

# **Chapter 1**

## **Introduction**

This chapter gives a brief introduction about unmanned aerial vehicles (UAVs). Then the objectives and motivation behind writing this thesis are discussed. Lastly, the structure of the thesis will be outlined.

### **1.1 Overview**

### **1.2 Motivation and Objective**

### **1.3 Thesis Outlines**

The thesis is organized into six chapters, each of which is briefly described below:

**Chapter 1** .....

**Chapter 2** .....

**Chapter 3** .....

**Chapter 4** .....

**Chapter 5** .....

**Chapter 6** .....

## Chapter 2

### Literature Review

#### 2.1 Analytical Techniques

The development of analytical techniques for evaluating aerodynamic derivatives has deep roots, tracing back to the pioneering work of researchers like Bryan [1]. However, the limitations in computational power and numerical approaches at the time meant that these early analytical methods were primarily applied to relatively simple configurations, often relying on various simplifying assumptions. One of the seminal contributions in this domain was Theodorsen's groundbreaking work [2] on the unsteady aerodynamics of the NACA 0012 airfoil undergoing harmonic oscillation. By leveraging potential flow theory, Theodorsen was able to calculate both the acceleration and rotary derivatives of the airfoil. Building upon this foundation, the mathematical approach for determining directional and sideslip derivatives in supersonic flow over thin airfoils was further refined and improved [3]. A particularly noteworthy contribution came from Etkin, who developed a comprehensive analytical framework [4] that provided a systematic and reliable means of deriving crucial parameters such as lift, drag, pitching moment, and control effectiveness coefficients. By exclusively relying on Etkin's well-established analytical techniques, researchers and designers can assess aircraft performance, stability, and control characteristics with a high degree of precision and reliability. The relevant formulas from Etkin's work are compiled in tables 2.1 and 2.2. While the underlying principles of these analytical methods are relatively straightforward, their application becomes exceedingly challenging when dealing with more complex scenarios. As a result, these early analytical techniques have largely been superseded by more sophisticated alternatives, as discussed in the subsequent sections of this thesis.

Neg. means usually negligible.

\* means contribution of the tail only, formula for wing-body not available.

$$\dagger C_{T_u} = \frac{(\partial T / \partial u)_0}{\frac{1}{2} \rho u_0 S} - 2C_{T_0}; C_{T_0} = C_{D_0} + C_{w_0} \sin \theta_0$$

\* Means contribution of the tail only, formula for wing-body not available;

$$V_F/V = 1.$$

Table (2.1) Represents the longitudinal derivatives based on the analytical methods derived by Etkins

	$C_x$	$C_z$	$C_m$
$\hat{u}^\dagger$	$M_0 \left( \frac{\partial C_T}{\partial M} - \frac{\partial C_D}{\partial M} \right) - \rho u_0^2 \frac{\partial C_D}{\partial p_d} + C_{T_u} \left( 1 - \frac{\partial C_D}{\partial C_T} \right)$	$-M_0 \frac{\partial C_L}{\partial M} - \rho u_0^2 \frac{\partial C_L}{\partial p_d} - C_{T_u} \frac{\partial C_L}{\partial C_T}$	$M_0 \frac{\partial C_m}{\partial M} + \rho u_0^2 \frac{\partial C_m}{\partial p_d} + C_{T_u} \frac{\partial C_m}{\partial C_T}$
$\alpha$	$C_{l_0} - C_{D_\alpha}$	$-(C_{L_\alpha} + C_{D_0})$	$-a(h_n - h)$
$\dot{\alpha}$	Neg.	$* - 2a_t V_H \frac{\partial \varepsilon}{\partial \alpha}$	$* - 2a_t V_H \frac{l_t}{\bar{c}} \frac{\partial \varepsilon}{\partial \alpha}$
$\hat{q}$	Neg.	$* - 2a_t V_H$	$* - 2a_t V_H \frac{l_t}{\bar{c}}$

Table (2.2) Represents the lateral derivatives based on the analytical methods derived by Etkins

	$C_y$	$C_l$	$C_n$
$\beta$	$* - a_F \frac{S_F}{S} \left( 1 - \frac{\partial \sigma}{\partial \beta} \right)$	N.A.	$* a_F V_v \left( 1 - \frac{\partial \sigma}{\partial \beta} \right)$
$\hat{p}$	$* - a_F \frac{S_F}{S} \left( 2 \frac{z_F}{b} - \frac{\partial \sigma}{\partial \hat{p}} \right)$	N.A.	$* a_F V_v \left( 2 \frac{z_F}{b} - \frac{\partial \sigma}{\partial \hat{p}} \right)$
$\hat{r}$	$* a_F \frac{S_F}{S} \left( 2 \frac{l_F}{b} + \frac{\partial \sigma}{\partial \hat{r}} \right)$	$* a_F \frac{S_F}{S} \frac{z_F}{b} \left( 2 \frac{l_F}{b} + \frac{\partial \sigma}{\partial \hat{r}} \right)$	$* - a_F V_v \left( 2 \frac{l_F}{b} + \frac{\partial \sigma}{\partial \hat{r}} \right)$

N.A. means no formula available

## 2.2 Empirical and Semi-empirical Methods

In the absence of analytical methods or when computational fluid dynamics (CFD) techniques have not yet been developed, various empirical and semi-empirical engineering approaches have been established. Empirical methods involve fitting different formulas or charts between the dynamic derivatives and the parameters, based on the dynamic derivative data of aircraft obtained from wind tunnel or flight tests. The DATCOM program is a prominent example of this strategy, incorporating a vast amount of aerodynamic data and serving as a helpful tool in the conceptual and preliminary stages of aircraft design [5]. While the DATCOM code can produce accurate results in typical setup scenarios, the relationships between dynamic derivatives and geometries become particularly complex for unconventional layouts or nonlinear flow fields, making it challenging to compute somewhat reliable findings [6] and [7]. To enhance the predictive capability of empirical methods, semi-empirical procedures have been developed. These semi-empirical approaches are based on a combination of assumptions and experimental evidence, providing basic mathematical models of a physical phenomenon. Two of the most commonly used semi-empirical methods for

calculating dynamic derivatives are the Newtonian impact theory and the piston theory-based approaches. These procedures can only be reliably applied within defined ranges.

### **2.2.1 Newtonian Impact Theory Based Method**

Newtonian impact theory, proposed as early as 1726, is an approximate approach for calculating the aerodynamic drag of moving objects based on the dynamics of individual particles [8]. This theory assumes that the gas is composed of multiple isolated particles, and the pressure on the body affects the momentum of the particles along the surface direction. For a plate moving uniformly in the air, the pressure coefficient  $C_p$  can be stated as shown in eqn. (2.1). While practical and theoretical studies have shown the Newtonian impact theory to have a rather substantial prediction error, it is still adequate for simulating hypersonic flows.

$$C_p = \frac{\rho V^2 S \sin^2 \alpha}{\frac{1}{2} \rho V^2 S} = 2 \sin^2 \alpha \quad (2.1)$$

Tobak was the first to present this theory, which allows for further integration of the unsteady aerodynamics from the pressure coefficient to determine the dynamic derivatives [9]. Comparing the dynamic derivatives derived from Newtonian impact theory with potential theory, he proved its practicability. To broaden its applicability, an embedded Newtonian flow theory was created in 1962, and its enhanced approach is utilized to compute the dynamic derivatives of hypersonic vehicles [10, 11]. This modification on Newtonian impact theory can swiftly calculate the dynamic derivatives by simplifying the flow in the shock layer, but it is limited to solving scenarios with relatively simple shock wave interactions.

### **2.2.2 Piston Theory Based Method**

Piston theory is another semi-empirical methodology for quickly calculating dynamic derivatives [12]. The fundamental assumption is a high Mach number  $Ma^2 \gg 1$  and a thin airfoil. According to the theory, the disturbance at one location has little effect on other points on the airfoil, and the pressure at this site is only connected to its downwash velocity. When the impulse theorem and isentropic principle are combined, the pressure  $p_A(x, y, t)$  at the position  $(x, y)$  of the airfoil can be expressed as shown in eq. (2.2).

$$p_A(x, y, t) = p_\infty \left( 1 + \frac{\gamma - 1}{2} \cdot \frac{V_n(x, y, t)}{a_\infty} \right)^{\frac{2\gamma}{\gamma - 1}} \quad (2.2)$$

The piston theory approach has been used to estimate the dynamic stability of several airfoils and the delta wing. In reality, the local speed at one point on the airfoil differs from that of the free stream; therefore, a modified local piston theory employing the local speed is developed to overcome the limitations on angle of attack and relative thickness [13, 14]. This method plays a significant role in the calculation of the dynamic derivatives of supersonic and hypersonic configurations.

## 2.3 Numerical Techniques

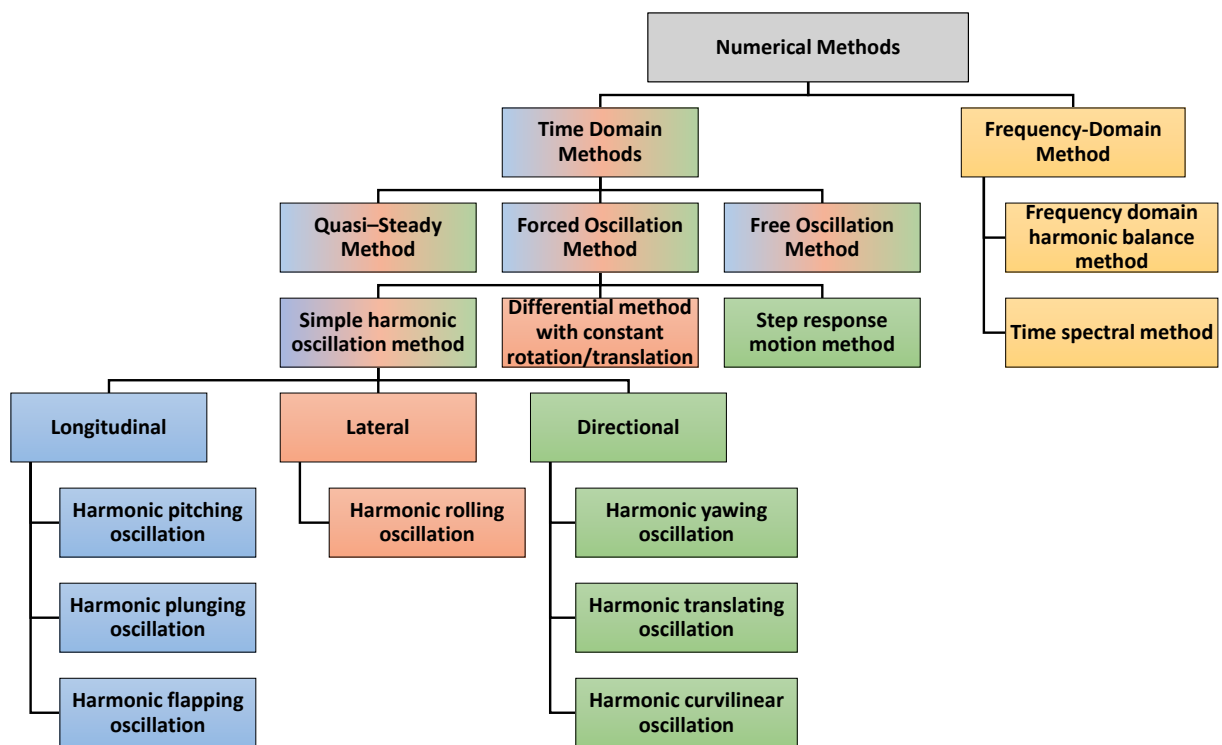


Fig. (2.1) Block chain for modern numerical approaches

Numerical methodologies have become essential in solving unsteady Euler or Navier-Stokes equations, which are crucial in computing unsteady aerodynamic forces and moments. These forces and moments, in turn, enable the determination of dynamic derivatives. Over the past decade, substantial advancements have been made in these techniques, significantly enhancing their efficiency and accuracy. In particular, the transition from time-domain to frequency-domain analyses has been a significant development in this field. Fig. (2.1) illustrates a flowchart depicting modern numerical methodologies primarily directed

towards solving unsteady Euler or Navier-Stokes equations.

### 2.3.1 Time Domain approaches

Temporal domain calculations involve determining dynamic derivatives of turbulent flow fields by examining their temporal characteristics. Certain steady and quasi-steady methods, such as quasi-steady analysis, forced oscillation analysis, and free oscillation analysis, are also classified as temporal domain techniques. These methods vary in cost and complexity.

#### 2.3.1.1 Quasi-Steady Method

The quasi-steady approach is a technique for deriving dynamic derivatives using computational fluid dynamics (CFD) simulations. This method involves solving steady governing equations in a non-inertial frame instead of an inertial frame. A common example of the quasi-steady approach is the computation of the rolling-damping derivative  $C_{l_p}$ , which represents the change in rolling moment per unit rolling rate. By applying a constant roll rate  $p$  to a steady body at zero angle of attack, a consistent rolling moment can be sustained.

$$C_l - C_{l_0} - C_{l_p} \frac{p c}{2V} = 0 \quad (2.3)$$

The quasi-steady approach involves transforming dynamic motion into a coordinate system where the body remains at rest, as shown in Fig. (2.2). Steady iterations are used to compute the aerodynamic forces and moments, and the rolling-damping derivative  $C_{l_p}$  is calculated using eq.(2.3) [15, 16]. This method can be applied to non-zero angles of attack, but the dynamic derivatives need to be transformed using eq.(2.4), as demonstrated in Fig. (2.3).

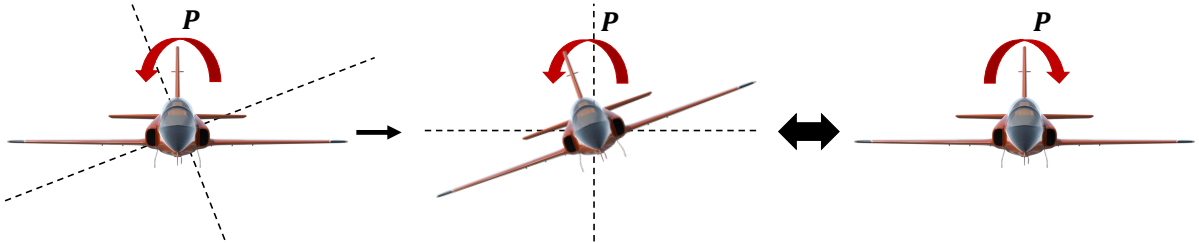


Fig. (2.2) Constant rolling at zero angle of attack

$$\begin{aligned} C_{l_p}^b &= C_{l_p}^w \cos^2 \epsilon - (C_{l_r}^w + C_{n_p}^w) \sin \epsilon \cos \epsilon + C_{n_r}^w \sin^2 \epsilon \\ C_{n_r}^b &= C_{n_r}^w \cos^2 \epsilon + (C_{l_r}^w + C_{n_p}^w) \sin \epsilon \cos \epsilon + C_{l_p}^w \sin^2 \epsilon \end{aligned} \quad (2.4)$$

In this context,  $\varepsilon$  indicates the angle between the body and wind axes. The quasi-steady approach can also be applied to compute the longitudinal-damping derivative  $C_{m_q}$ , as shown in Fig. (2.4). For instance, during a constant pull-up maneuver without elevator angle, the aircraft maintains a stable rotation in the vertical plane while the velocity and angle of attack remain constant. By applying a constant pitch rate to the frame rather than the aircraft, the flow field can be converted to a steady case, enabling the calculation of damping derivatives using the quasi-steady approach. Using the pitch rate  $q$  and radius  $R$  of the motion to maintain  $V = qR$  at the center of gravity of the aircraft, the constant pitching moments  $C_{m_q}$  can be easily determined. The basic quasi-steady approach can only determine the damping derivative of

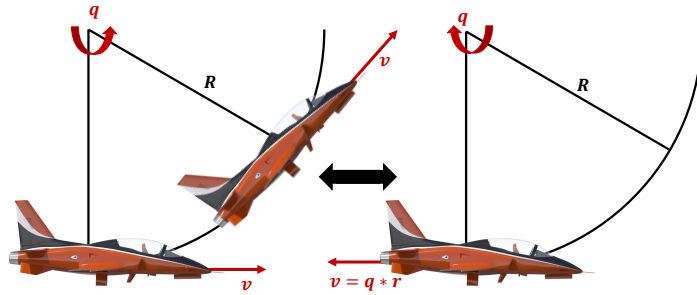


Fig. (2.3) Steady pull-up maneuver

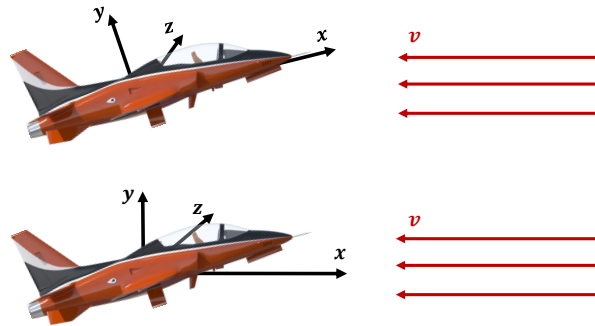


Fig. (2.4) Constant rolling at non-zero angle of attack

a symmetrical configuration. Park introduced a universal method for computing all dynamic derivatives through constant computation [17]. While the quasi-steady approach can serve as a simpler calculation methodology, it was initially limited to calculating the rotating derivatives of simple thin bodies. However, with the expansion of computational fluid dynamics (CFD)

codes in non-inertial reference frames, the approach can now compute all dynamic derivatives. Despite its increased applicability, this technique has inherent limitations and cannot accurately represent nonlinear unsteady aerodynamics. Moreover, the precision of dynamic derivative calculations using this method is inferior to that of unsteady methods. Nevertheless, it remains a practical approach for establishing initial design parameters.

### **2.3.1.2 Forced Oscillation Method**

The forced oscillation method has been widely used to compute dynamic derivatives [18, 19]. This technique involves extracting unstable aerodynamic data from various dynamic maneuvers, originating from dynamic wind tunnel tests. Known for its high precision and adaptability, the forced oscillation method yields favorable outcomes across subsonic, supersonic, and hypersonic regimes. It is considered the most comprehensive approach for simulating dynamic derivatives in the time domain and is reliable for generating inputs for flight quality assessments.

However, the conventional forced oscillation technique primarily calculates integrated dynamic derivatives, which may be insufficient for sophisticated aircraft requiring precise aerodynamic and control system development with comprehensive individual dynamic derivatives. Consequently, several innovative methods have been developed and verified. This study analyzes the advantages and limitations of various forced oscillation methods.

#### **2.3.1.2.1 Simple harmonic oscillation method**

The earliest form of dynamic derivatives encountered is the combined dynamic derivative, which is the primary focus of identification for most traditional approaches. This derivative is commonly estimated using a simple harmonic oscillation technique. Unsteady aerodynamics determined through computational fluid dynamics (CFD) tools can be employed to derive combined dynamic derivatives, achieved by inducing simple harmonic motion in the aircraft's oscillation around its center of gravity. For example, in longitudinally disturbed motion as depicted in Fig. (2.5), the aircraft undergoes oscillations about its center of gravity, resulting in an instantaneous change in angle of attack given by:

$$\Delta\alpha = \alpha_m \sin(\omega t) \quad (2.5)$$



Fig. (2.5) Longitudinal simple harmonic oscillation

The pitching moment coefficient can be expressed as a function of the angle of attack variation  $\Delta\alpha$  and the pitch rate  $q$ , that is,  $C_m = f(\Delta\alpha, q)$ .

$$C_m = C_{m_0} + C_{m_\alpha}\Delta\alpha + C_{m_{\dot{\alpha}}}\Delta\dot{\alpha} + C_{m_q}\Delta q + C_{m_{\dot{q}}}\Delta\dot{q} + \hat{\Delta}(\Delta\alpha, q) \quad (2.6)$$

When the free stream is steady, the pitching rate  $q$  becomes equivalent to  $\Delta\dot{\alpha}$ , the angular acceleration of the aircraft.

$$\Delta\dot{\alpha} = \omega\alpha_m \cos(\omega t) = q \quad (2.7)$$

$$\Delta\ddot{\alpha} = -\omega^2\alpha_m \sin(\omega t) = \dot{q}$$

The unsteady moment coefficient can be simplified as  $C_m = C_{m_0} + C_{m_\alpha}\Delta\alpha + (C_{m_{\dot{\alpha}}} + C_{m_q})\Delta\dot{\alpha}$  for small or medium angles of attack, neglecting higher-order components due to linear or weakly nonlinear aerodynamics.

$$C_m = C_{m_0} + C_{m_\alpha}\Delta\alpha + (C_{m_{\dot{\alpha}}} + C_{m_q})\Delta q \quad (2.8)$$

Various methods can be used to identify the combined dynamic derivative  $C_{m_{\dot{\alpha}}} + C_{m_q}$ , such as the integration method, the least squares method, and the single-point method. The integration method calculates the average result by considering the influence of time history through the area integral of the aerodynamic moment. The least squares method directly determines the coefficients by fitting the unsteady aerodynamic moment data. The single-point method computes the dynamic derivative using quasi-steady and sometimes unsteady aerodynamic moments, but it can yield significant inaccuracies in nonlinear situations.

Additionally, the simple harmonic oscillation method can be applied to determine lateral combined dynamic derivatives, associated with simple harmonic rolling and yawing

oscillations, and cross terms can be calculated using similar techniques. Enhancements to the basic harmonic plunge oscillation can provide more precise computations of dynamic derivatives. In this technique, the angle of attack is altered while the unsteady aerodynamic moment remains unaffected by pitch rate, allowing for the determination of one of the single dynamic derivatives,  $C_{m\dot{\alpha}}$ . Fig. (2.6) illustrates the basic harmonic plunge oscillation.

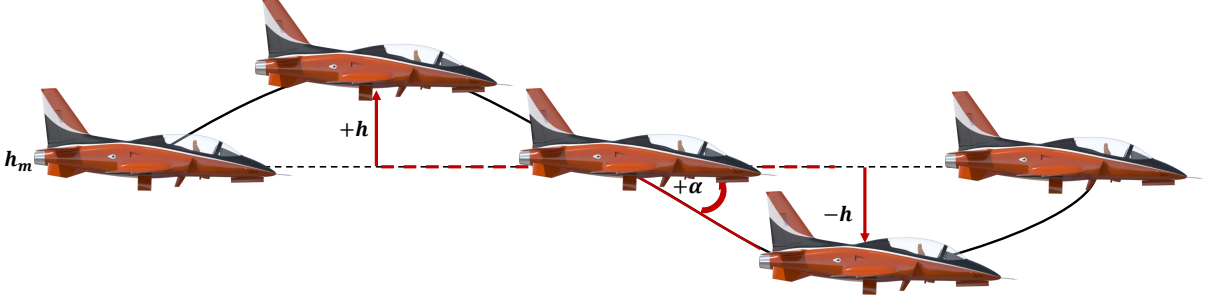


Fig. (2.6) Process of simple harmonic plunge oscillation

$$h(t) = h_m \sin(\omega t) \quad (2.9)$$

The aircraft's vertical motion during oscillation can be described by the above equation. As oscillation occurs, the angle of attack increases, which can be expressed as:

$$\Delta\alpha \approx \frac{\Delta V}{V} = \frac{\omega h_m \cos(\omega t)}{V} \quad (2.10)$$

$$\Delta\dot{\alpha} = \frac{-\omega^2 h_m \sin(\omega t)}{V} \quad (2.11)$$

The unsteady aerodynamic moment's Taylor expansion can be approximated by neglecting higher-order terms.

$$C_m = C_{m_0} + C_{m\alpha}\Delta\alpha + C_{m\dot{\alpha}}\Delta\dot{\alpha} \quad (2.12)$$

The pitching moment coefficient derivative with respect to angle of attack rate,  $C_{m\dot{\alpha}}$ , can be determined using the same methodology as  $C_{m\alpha} + C_{m_q}$ . The derivatives of directional acceleration,  $C_{n\dot{\beta}}$  and  $C_{l\dot{\beta}}$ , can be identified through translating oscillation.

Moreover, the simple harmonic oscillation technique offers an efficient approach for calculating the damping derivative  $C_{m_q}$ . As depicted in Fig. (2.7), the flapping motion combines pitching and plunging oscillations without canceling the effect of angle of attack

when determining  $C_{m_q}$ . This technique involves subtracting both the acceleration and combined derivatives while considering harmonic oscillation [20].

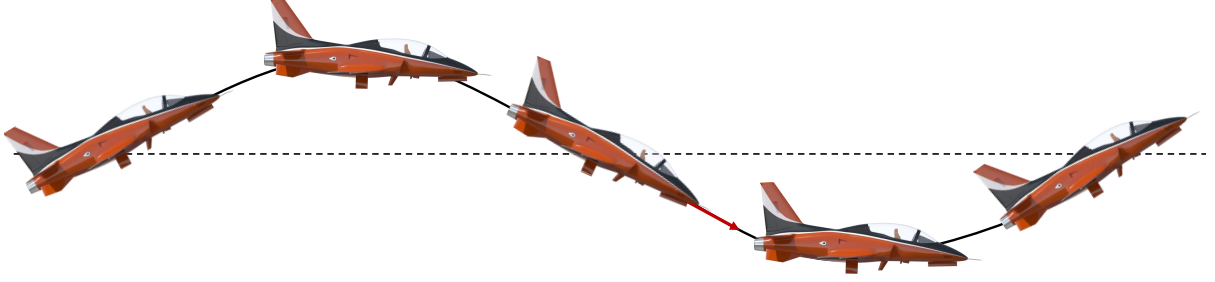


Fig. (2.7) Simple harmonic flapping oscillation

The additional angle of attack due to pitching oscillation is given by:

$$\Delta\alpha = \alpha_m \sin(\omega t) \quad (2.13)$$

To counteract the effect of  $\Delta\alpha$ , the additional velocity must provide a negative  $\Delta\alpha$  value:

$$\Delta V = -V\alpha_m \sin(\omega t) \quad (2.14)$$

The plunging oscillation is defined as:

$$h(t) = \frac{V\alpha_m}{\omega} \cos(\omega t) = h_m \cos(\omega t) \quad (2.15)$$

Similar to  $C_{m_q}$ , the directional-damping derivatives  $C_{n_r}, C_{l_r}$  are estimated using the coupled oscillations of translation and yawing.

*Hui et al.* [21] pioneered the application of resonance perturbation methodology to quantify dynamic derivatives, conceptualizing unsteady flow as a linear superposition of steady flow and minor perturbative flows induced by oscillations. These perturbations are approximated to Euler solutions, simplifying the computation process. Pitch damping derivatives are then derived through the evaluation of aerodynamic moments using transformation formulas across different axes. A universal Unmanned Combat Air Vehicle (UCAV), named SACCON, was developed by DLR and EADS-MAS to validate stability and control prediction algorithms [22, 23]. SACCON features a blended delta wing-body

configuration and both static and dynamic wind tunnel data were generated for the SACCON model using a low-speed wind tunnel by NASA Langley and the German-Dutch Wind Tunnel (DNW). The National Research Council of Canada (NRC) introduced a calibration model for dynamic rotational and oscillatory testing, alongside numerical validation [24, 25]. This model generates steady vortices from the strake wing to mitigate flow separation over the delta wing, demonstrating the efficacy of CFD algorithms in simulating dynamic derivatives at transonic speeds. The Basic Finner Missile (BFM) model is widely used as a dynamic derivative model due to its simplistic design and extensive availability of wind tunnel test data [26–29]. Recent systematic research conducted by the European project SimSAC has showcased significant advancements in the experimental and numerical determination of dynamic derivatives [30, 31]. The dynamic derivatives of the F/A-18 and F-16 fighters were also assessed, validating the practical efficacy of the simple harmonic oscillation method in simulating the aerodynamics of high-maneuverability aircraft. Fig. (2.8) details the methodology for computing both longitudinal and lateral single, as well as combined dynamic derivatives using the simple harmonic oscillation method, contributing significantly to the field of aerodynamic research.

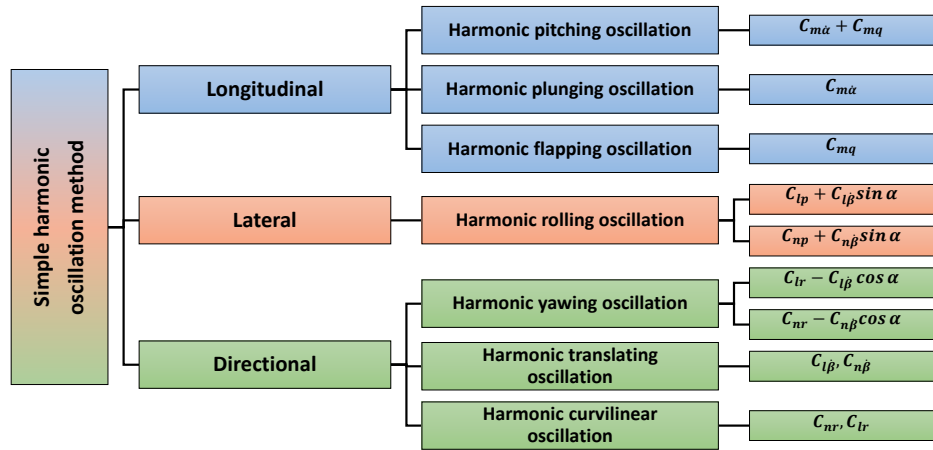


Fig. (2.8) Calculating dynamic derivatives with simple harmonic oscillation method

#### 2.3.1.2.2 Differential method with constant rotation/translation

The periodic motion of a flying vehicle in simple harmonic oscillation requires the computation of unsteady state, which is essentially a reduction from the steady state. To ensure periodic variation of aerodynamic forces and moments, simulating more than three harmonic

oscillations is necessary, although this can be time-consuming. To address this challenge, a differential approach has been proposed based on the difference in the vehicle's forces and moments, providing an efficient means to compute both single and combined dynamic derivatives [32, 33]. The differential method used for computing combined dynamic derivatives involves the inducement of constant pitching with two distinct pitch rates. By altering the aircraft's pitch by  $\Delta\alpha$  using pitch rates  $q_1$  and  $q_2$ , the relationship between the additional angle of attack  $\Delta\alpha$  and the pitch rates  $q$  is illustrated in Fig. (2.9) and given by:

$$\begin{aligned}\Delta\alpha &= q_1 t_1 \\ \Delta\alpha &= q_2 t_2\end{aligned}\tag{2.16}$$

$$\begin{aligned}C_{m_1} &= C_{m_0} + C_{m_\alpha}\Delta\alpha + (C_{m_\alpha} + C_{m_q}) q_1 \\ C_{m_2} &= C_{m_0} + C_{m_\alpha}\Delta\alpha + (C_{m_\alpha} + C_{m_q}) q_2\end{aligned}\tag{2.17}$$

The pitching moment coefficients due to angle of attack values  $\alpha_1$  and  $\alpha_2$  are  $C_{m_1}$  and  $C_{m_2}$ ,

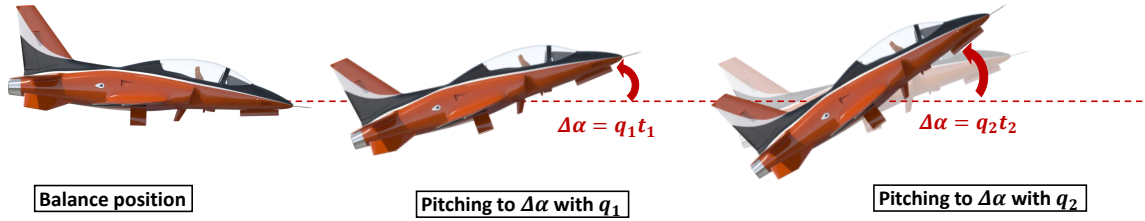


Fig. (2.9) Combined dynamic derivative calculation with differential method

respectively. The combined dynamic derivative can be computed by subtracting the two equations:

$$C_{m_\alpha} + C_{m_q} = \frac{C_{m_1} - C_{m_2}}{q_1 - q_2}\tag{2.18}$$

The differential method differs from the conventional simple harmonic oscillation method in that it does not involve periodic calculations, making it more efficient. However, it still assumes minor disturbances, with the additional angle of attack  $\Delta\alpha$  induced by the pitch rate being equivalent in magnitude to the amplitude of the harmonic oscillation. The differential method is used for deriving combined dynamic derivatives during continuous

rolling or yawing motion in lateral simulation. The acceleration derivative  $C_{m\ddot{\alpha}}$  is modeled based on the aerodynamic disparity resulting from constant plunging movements. By inducing the aircraft to translate to the same instantaneous additional angle of attack using two additional velocities derived from constant angle of attack rates  $\dot{\alpha}_1$  and  $\dot{\alpha}_2$ , the relationships between the incremental angle of attack and velocities are illustrated in Fig. (2.10) and given by:

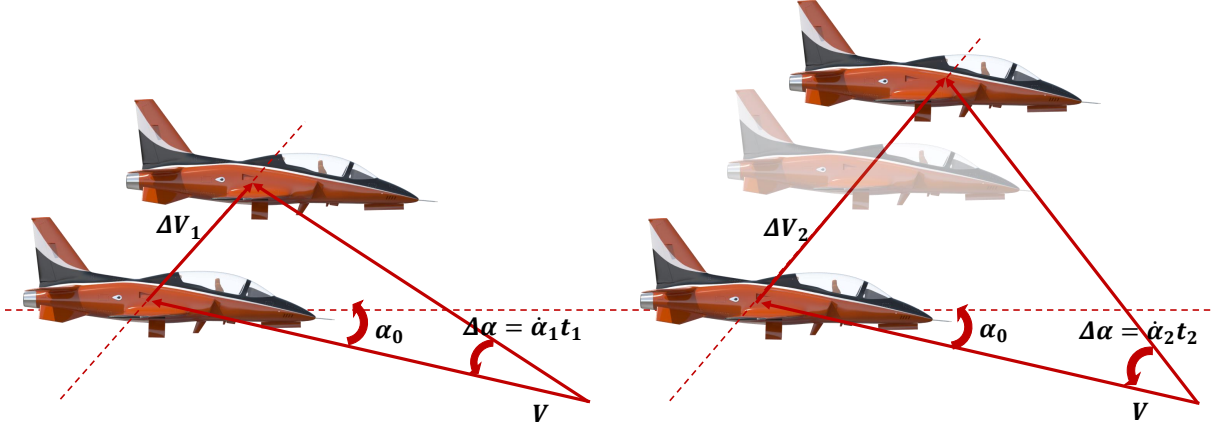


Fig. (2.10) Acceleration derivative identification with differential method

$$\Delta V_1 = V \tan(\dot{\alpha}_1 t_1) \approx V \dot{\alpha}_1 t_1 \quad (2.19)$$

$$\Delta V_2 = V \tan(\dot{\alpha}_2 t_2) \approx V \dot{\alpha}_2 t_2$$

The unsteady aerodynamic moments can be expressed using the principle of small disturbances as:

$$C_{m_1} \doteq C_{m_0} + C_{m_\alpha} \cdot \Delta\alpha + C_{m_{\alpha\dot{\alpha}_1}} \quad (2.20)$$

$$C_{m_2} \doteq C_{m_0} + C_{m_\alpha} \cdot \Delta\alpha + C_{m_{\alpha\dot{\alpha}_2}}$$

Since the additional angles of attack at the final times are equivalent, the rotational derivative  $C_{m\ddot{\alpha}}$  can be determined by subtracting the two corresponding equations:

$$C_{m\ddot{\alpha}} \doteq \frac{C_{m_1} - C_{m_2}}{\dot{\alpha}_1 - \dot{\alpha}_2} \quad (2.21)$$

The rotational derivative  $C_{m_q}$  and the single derivatives of  $C_{l_\beta}$  and  $C_{n_\beta}$  are also computed using lateral variations in aerodynamic moments resulting from constant translations in the spanwise direction. The differential approach is more efficient than the conventional

simple harmonic plunging oscillation method since acceleration derivatives are derived through simulations involving translations with two distinct angles of attack. However, an increase in computational time may lead to the emergence of additional angles of attack, potentially introducing numerical errors. Therefore, it is necessary to estimate a suitable angle and calculation time before applying this approach.

### 2.3.1.2.3 Step response motion method

The differential approach requires the execution of two constant movements to derive a single dynamic derivative. However, given its complexity, a more systematic approach is needed. A novel technique based on step response motion has been developed, capable of computing static and single dynamic derivatives in a step-wise manner [?, ?]. The relationship between the static derivative  $C_{m_\alpha}$ , the acceleration derivative  $C_{m_{\ddot{\alpha}}}$ , and the rotational derivative  $C_{m_q}$  with respect to the angle of attack, the rate of angle of attack, and pitch rate reaction movements is depicted in Fig. (2.11).

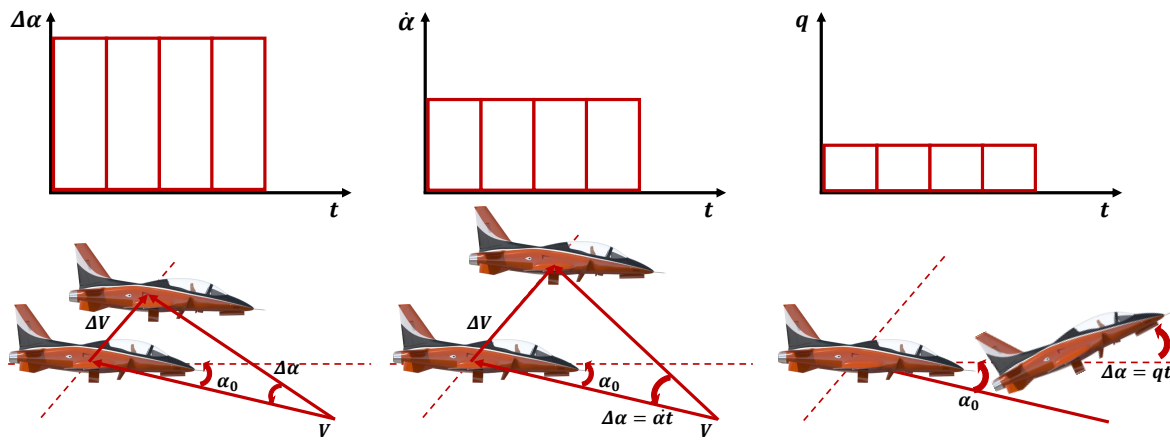


Fig. (2.11) Static and single dynamic derivatives calculation with step response method

The initial step in this method involves executing the angle of attack reaction motion, where the flight vehicle is forced to move with a constant additional angle of attack  $\Delta\alpha$  to compute  $C_{m_\alpha}$ . Since only  $\Delta\alpha$  influences the dynamic motion, the unsteady aerodynamic moment increases. This step is illustrated in Fig. (2.12).

$$C_{m_1} = C_{m_0} + C_{m_\alpha} \cdot \Delta\alpha \quad (2.22)$$

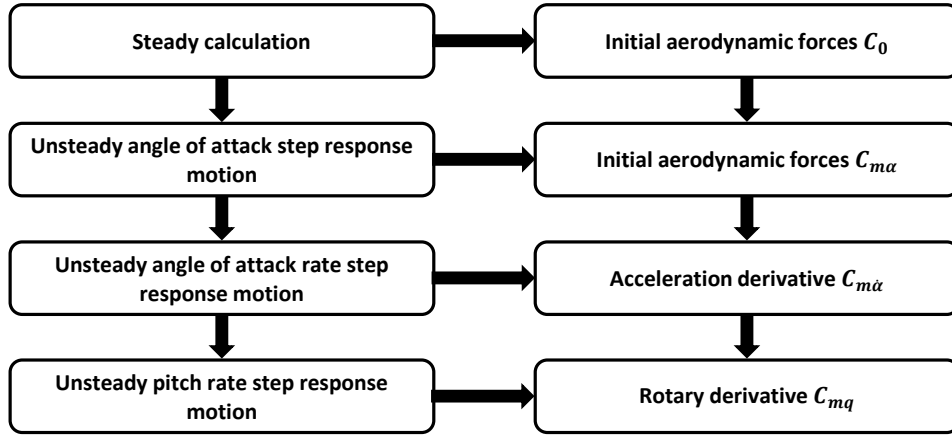


Fig. (2.12) Detail calculating process of step response method

The static derivative  $C_{m_\alpha}$  can be directly computed by integrating unsteady and initial-steady aerodynamic moments:

$$C_{m_\alpha} = \frac{C_{m_1} - C_{m_0}}{\Delta\alpha} \quad (2.23)$$

Subsequently, the aircraft responds to the rate of angle of attack motion with  $\dot{\alpha}$ , resulting in a constant additional angle of attack  $\Delta\alpha = \dot{\alpha}t$ . The aerodynamic characteristics depend solely on the variables  $\Delta\alpha$  and  $\dot{\alpha}$ :

$$C_{m_2} \approx C_{m_0} + C_{m_\alpha} \cdot \Delta\alpha + C_{m_{\dot{\alpha}}} \cdot \dot{\alpha} \quad (2.24)$$

The acceleration derivative is obtained by subtracting the final unsteady moments  $C_{m_2}$  and  $C_{m_1}$  at the same angle of attack  $\Delta\alpha$ :

$$C_{m_{\ddot{\alpha}}} = \frac{C_{m_2} - C_{m_1}}{\ddot{\alpha}} \quad (2.25)$$

The rotary derivative  $C_{m_q}$  can be determined by performing a consistent pitching motion with a constant additional angle of attack  $\Delta\alpha = qt$ , which integrates the effects of angle of attack and pitch rate into an unsteady aerodynamic moment.

$$C_{m_3} \approx C_{m_0} + C_{m_\alpha} \cdot \Delta\alpha + C_{m_{\dot{\alpha}}} \cdot \dot{\alpha} + C_{m_q} \cdot q \quad (2.26)$$

The following is a concise derivation of  $C_{m_q}$  using the rate of angle of attack response motion:

$$C_{m_q} = \frac{C_{m_3} - C_{m_2}}{\bar{q}} \quad (2.27)$$

The novel approach, characterized by simplified motion patterns, reduces computation times by more than 60 percent compared to traditional harmonic oscillation methods. However, its heightened sensitivity to the dynamic flow field can lead to oscillations in aerodynamic forces and moments due to minor nonlinearities, reducing identification accuracy.

Forced oscillation methods, including traditional harmonic oscillation techniques and extended motion methods, are governed by three primary parameters: frequency, motion rate, and amplitude. Among these, frequency plays a crucial role in governing unsteady motion.

When the reduced frequency is low, the accurate estimation of unsteady hysteresis becomes difficult, yielding poor dynamic derivative outcomes or even sign reversals. Some scholars attribute this to the aircraft transitioning from a dynamically stable state to an unstable state as the reduced frequency decreases. Others attribute it to numerical simulation inaccuracies in forced oscillation methods. Regardless of the perspective, careful analysis of the specific computational model and optimal frequency selection are necessary to improve numerical computation accuracy.

### **2.3.1.3 Free Oscillation Method**

The free oscillation method, obtained from wind tunnel experiments, computes dynamic derivatives by inducing oscillations about a fixed axis in a rigid aircraft subjected to an initial instantaneous disturbance [?]. This method more accurately reflects the essence of dynamic derivatives than harmonic oscillation techniques, as it showcases the aircraft's ability to recover to its initial state post-disturbance. Incorporating inertia and mass values derived from empirical data, and with frequency and modal characteristics closely resembling those of the actual model, the single degree-of-freedom oscillation method eliminates the need for reduced frequency selection inherent in harmonic oscillation methods, thereby enhancing the

fidelity of flight simulations. Oscillation with a single degree of freedom is typically employed to ascertain dynamic derivatives [?, ?], as depicted in Fig. (2.13). The free pitch maneuver involves granting lateral and directional freedoms, followed by applying angular pitch excitation to the aircraft, inducing longitudinal oscillation influenced by aerodynamics and inertias. The interaction between the aerodynamics and inertia of a flight vehicle during free pitch oscillation about a fixed axis is characterized by:

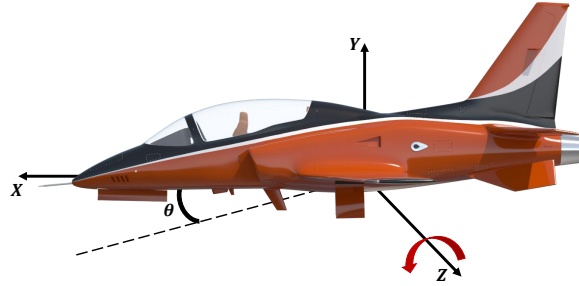


Fig. (2.13) Free pitch oscillation to calculate the longitudinal dynamic

$$I_z \ddot{\theta} - n_z \dot{\theta} - C_m = 0 \quad (2.28)$$

The moment of inertia to the z-axis, damping coefficient, and pitching moment coefficient are denoted by  $I_z$ ,  $n_z$  and  $C_m$ , respectively.

When the free stream is constant, the unsteady pitch moment is amplified by removing higher-order components, resulting in:

$$C_m = C_{m_\alpha} \theta + (C_{m_q} + C_{m_{\dot{\alpha}}}) \dot{\theta} \quad (2.29)$$

Substituting this expression into the free oscillation method equation yields:

$$I_z \ddot{\theta} - (n_z + (C_{m_q} + C_{m_{\dot{\alpha}}})) \dot{\theta} - C_{m_\alpha} \theta = 0 \quad (2.30)$$

The combined-dynamic derivatives,  $(C_{m_q} + C_{m_{\dot{\alpha}}})$ , determine the system's damping and oscillation mode. The pitch moment amplitude decreases, indicating dynamic stability when  $(C_{m_q} + C_{m_{\dot{\alpha}}}) < 0$ ; it increases, indicating dynamic instability when  $(C_{m_q} + C_{m_{\dot{\alpha}}}) > 0$ ; and it

remains constant, indicating neutral stability when  $(C_{m_q} + C_{m_{\dot{\alpha}}}) = 0$ .

The general solution to eq. (2.28) is given by  $\theta = Ae^{\lambda t} \cos(\omega t + \varphi)$ . By employing computational fluid dynamics (CFD) algorithms, the time-history of the pitch moment can be obtained, enabling the determination of combined dynamic derivatives. For small damping modes,  $(C_{m_q} + C_{m_{\dot{\alpha}}})$  can be approximated using instantaneous angles and times at the peak of oscillation. However, in cases of large damping or divergence, these values must be determined through the Moore–Penrose generalized inversion technique.

The Moore-Penrose Pseudoinverse is a linear algebra approach that facilitates the estimation of the inverse for matrices that are not directly invertible. This technique enables effective computation of inverse approximations for matrices of various rectangular dimensions, accommodating all conceivable matrix configurations.

Although the free oscillation method offers an accurate representation of dynamic derivatives and superior solution precision, practical implementation is challenging. The unconstrained calculation process, primarily dictated by model inertia, may render CFD simulations more time-consuming compared to the harmonic oscillation method, potentially resulting in significant errors in dynamic derivative identification. Furthermore, the restricted range of oscillation shapes limits the applicability of the free oscillation technique in calculating single and cross dynamic derivatives. These limitations have hindered the frequent utilization of the free oscillation approach in CFD simulations of dynamic derivatives.

### ***2.3.2 Frequency Domain approaches***

The traditional harmonic oscillation approach with dual-time step has a primary drawback: computationally intensive periodic unsteady aerodynamic calculations, making it impractical for complex configurations. To address this, frequency domain approaches have been developed, incorporating periodic aerodynamics of harmonic oscillation [?]. By leveraging multiple transient flow field solutions, it becomes feasible to reconstruct the entire unsteady flow field. Initially designed for turbine blades, these frequency domain techniques have demonstrated versatility in predicting flow characteristics around various aerodynamic structures, including helicopter rotor blades, circular cylinders, and aircraft flutter [?, ?, ?].

Frequency domain approaches can be categorized into linear and nonlinear types, with the latter being employed for dynamic derivative computations [?]. Within the nonlinear realm,

the harmonic balance method subdivides into direct, time-domain, frequency, and splitting field methods [?]. Among these, the frequency domain harmonic method and time spectral approach are prominent techniques for calculating dynamic derivatives within the time domain harmonic balance method.

### 2.3.2.1 *Frequency domain harmonic balance method*

The unsteady flow field can be expressed as:

$$\omega DQ + R = \hat{0} \quad (2.31)$$

where  $\omega$  is the angular frequency,  $R$  is the flux vector, and  $Q$  is the conservative variable.

The coefficient matrix  $D$  is defined as:

$$D_{i,j} = \frac{2}{N_T} \sum_{k=1}^{N_H} k \sin[2\pi k(j-i)/N_T] \quad (2.32)$$

The equation can be transformed into the frequency domain using Fourier transformation and introducing a pseudo-time parameter  $E$ . The time-domain solution  $Q$  for periodic unsteady flow can be reconstructed using frequency-domain data. The unsteady aerodynamic forces and moments for harmonic oscillation can be computed using the frequency domain harmonic balance method and data obtained at specified sample periods. Dynamic derivatives can be determined using various methodologies, and the frequency domain harmonic balance approach can simulate both single and combined dynamic derivatives.

$$\hat{Q} = EQ \quad (2.33)$$

$$Q(t) = \hat{Q}0 + \sum_{n=1}^{\infty} [\hat{Q}cn \cos(\omega nt) + \hat{Q}sn \sin(\omega nt)] \quad (2.34)$$

### 2.3.2.2 *Time spectral method*

The Frequency Domain Harmonic Balance Method transforms the control equations of an unsteady flow field into the frequency domain, and reconstructs periodic aerodynamic forces using multiple sampling instances. To handle the fluctuations in flow field variables, the

Time Spectral Approach was developed, which performs all computations in the time domain, eliminating the need for domain conversion and making it more practical for analyzing periodic unsteady flow fields.

The Time Spectral Method divides the time period  $T$  into  $N$  equal parts and uses the Discrete Fourier Transform (DFT) to calculate the flow field variable  $w^n$  at time  $n$ . The time derivative at the  $n^{th}$  time is given by eq. (2.37), which illustrates that the time derivative can be analytically expressed as a function of  $w^n$  at all sample times.

The Time Spectral Method enables the determination of both single and combined dynamic derivatives associated with harmonic oscillations. However, the Frequency Domain Approach may entail a decrease in the accuracy of unsteady flow field calculations compared to the dual-time step technique due to the loss of important signal energy content. The number of sample times dictates both the precision and efficiency of frequency domain techniques for calculating dynamic derivatives.

$$\hat{w}_k = \frac{1}{N} \sum_{n=0}^{N-1} w^n \exp\left(-ik \frac{2\pi}{T} n \Delta t\right) \quad (2.35)$$

The inverse transformation is

$$w^n = \sum_{k=-\frac{N}{2}}^{\frac{N}{2}-1} \hat{w}_k \exp\left(ik \frac{2\pi}{T} n \Delta t\right) \quad (2.36)$$

The time derivative at  $n$  time is given as

$$D_t w^n = \frac{2\pi}{T} \sum_{k=-\frac{N}{2}}^{\frac{N}{2}-1} ik \hat{w}_k \exp\left(ik \frac{2\pi}{T} n \Delta t\right) = \sum_{m=-\frac{N}{2}}^{\frac{N}{2}-1} d_m w^{n+m} \quad (2.37)$$

$$\text{where } d_m = \begin{cases} \frac{2\pi}{T} \cdot \frac{1}{2} (-1)^{m+1} \cot\left(\frac{m\pi}{N}\right), & m \neq 0 \\ 0, & m = 0 \end{cases} \quad (2.38)$$

$$V \frac{\partial w^n}{\partial \tau} + V D_t w^n + R(w^n) = 0 \quad (2.39)$$

## 2.4 Experimental Techniques

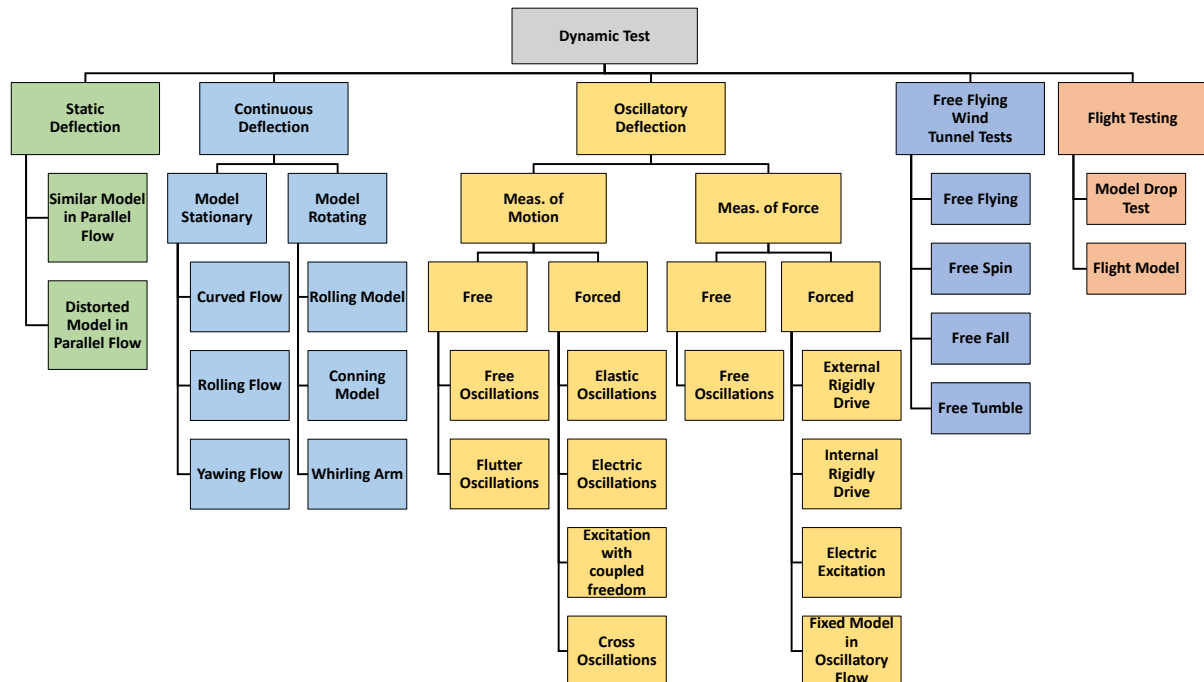


Fig. (2.14) Experimental Techniques Flowchart for measuring dynamic derivatives

one undeniable truth prevails: Experimental Techniques stand as the epitome of reliability in data acquisition, notwithstanding their inherent challenges and substantial costs. In light of this, Fig. (2.14) serves as a comprehensive compendium, delineating the diverse spectrum of experimental methodologies employed for assessing aerodynamic derivatives. Through this elucidation, researchers gain invaluable insights into the myriad approaches available, guiding their endeavors towards a deeper understanding of aerodynamic phenomena.

### 2.4.1 Static Deflection

In the domain of experimental aerodynamics, the investigation of static deflection emerges as a cornerstone for understanding the aerodynamic forces and moments acting on models subjected to uniform airflow within a wind tunnel's test section. This meticulous examination is pivotal for the derivation of aerodynamic derivatives, which are indispensable for evaluating the stability, control, and maneuverability of aerospace vehicles. The process involves the strategic positioning of the model, either in its geometrically analogous form or in a deliberately distorted configuration, to measure the forces and moments along the three-coordinate axes under varying attack and sideslip angles.

### 2.4.1.1 Similar geometrical models in straight parallel flow

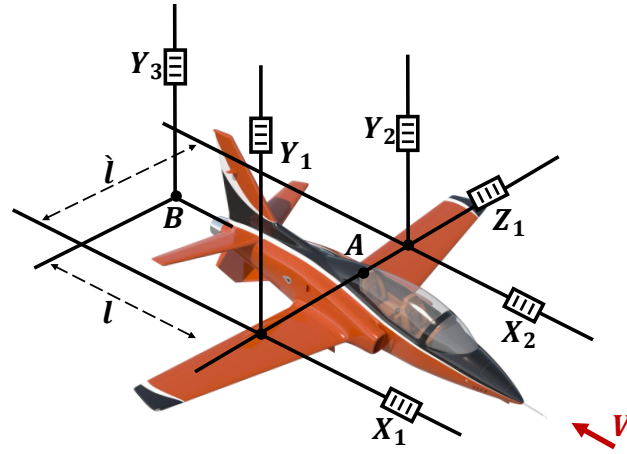


Fig. (2.15) Model Suspension for Static Deflection Test

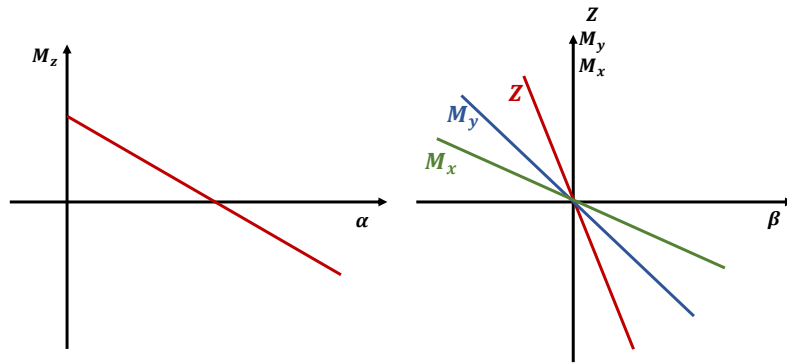


Fig. (2.16) Results of static deflection test

The initial phase of static deflection analysis focuses on geometrically analogous models exposed to straight parallel flow. Here, the model is securely anchored within the test section, as depicted in Fig. (2.15), to ensure precise measurement of aerodynamic loading. The forces and moments generated are meticulously recorded, taking into account the influence of wind tunnel boundary conditions. The results are subsequently articulated as functions of attack and sideslip angles, showcased in Fig. (2.16). The aerodynamic derivatives are calculated based on the slopes of these relationships at the original position angles prior to any disturbance. This method, while straightforward, is primarily confined to the extraction of static derivatives.

### 2.4.1.2 Distorted geometric models in straight parallel flow

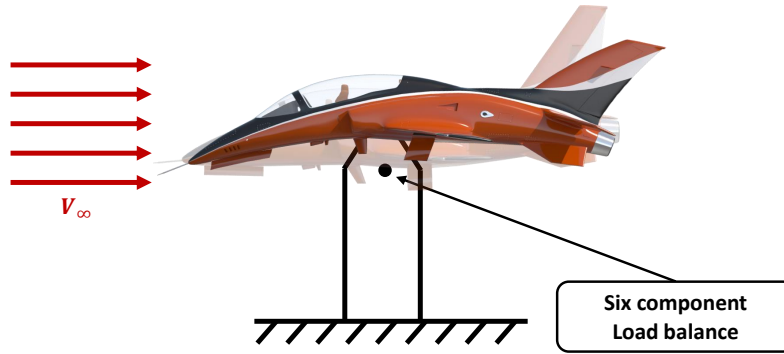


Fig. (2.17) Distorted Model in Parallel Flow

Advancing the study, the analysis extends to distorted geometric models subjected to straight parallel flow, as illustrated in Fig.(2.17). This innovative approach entails the intentional deformation of the model to emulate the pressure distributions observed in a non-distorted model undergoing motions such as rolling, pitching, or yawing in a parallel flow. Standard six-component measurements are conducted, mirroring the procedure outlined for geometrically analogous models. The essence of this method lies in its ability to measure dynamic derivatives on stationary models using static balances. However, it necessitates the fabrication of multiple complex and costly models to achieve the desired outcomes.

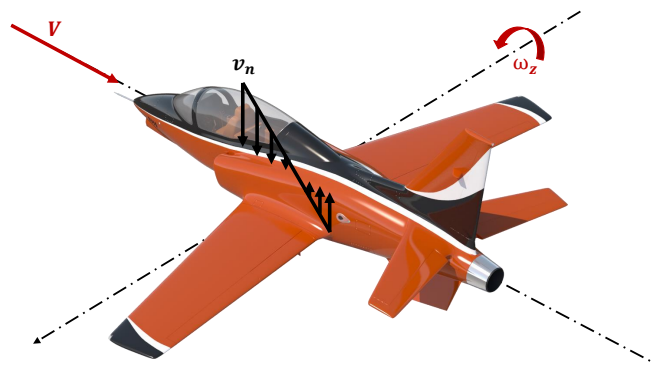


Fig. (2.18) Normal velocity distribution on wing in pitching motion

The mathematical underpinning of this analysis involves the integration of velocity distribution equations to model the distorted geometric configurations accurately. For instance,

considering a plane with a lifting surface at zero angle of attack, rotating with angular velocity  $q$ , and a wind speed of  $V$ , the wind velocity distribution normal to the wing depicted in Fig.(2.18) is given by:

$$V \frac{\partial y}{\partial x} = -xq$$

Upon integration with respect to  $x$ , the equation yields:

$$y = -\frac{1}{2} \frac{q}{V} x^2$$

This equation facilitates the modeling of a cambered wing that mimics the same velocity distribution when at rest and flying in straight parallel flow  $V$ , thereby enabling the measurement of dynamic derivatives on stationary models using static balances.

## 2.4.2 Continous Deflection

In this set of data, a relative continuous angular deviation is produced between the model and the airflow. It is achieved either by moving the model in a straight parallel flow or by flowing the stationary model in a curving or rolling flow.

### 2.4.2.1 Mode Stationary (Curved Flow)

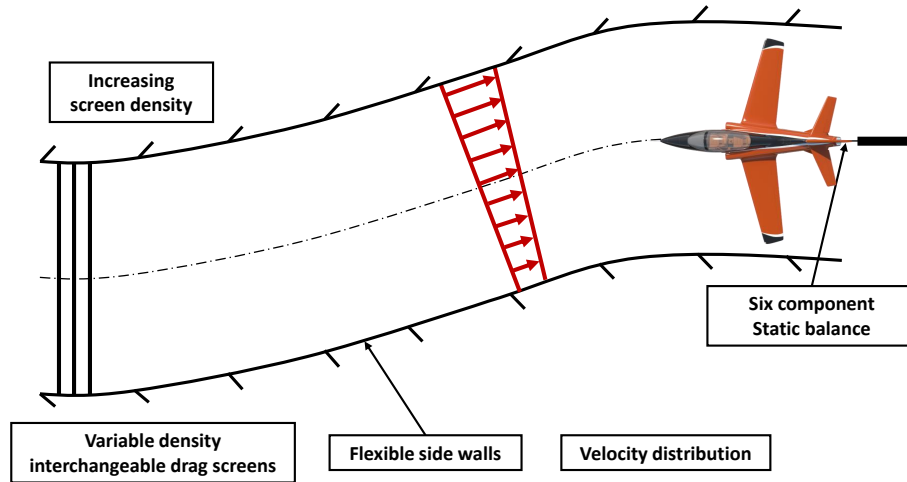


Fig. (2.19) Testing in curved flow

Aerodynamic coefficients relevant to pure yawing ( $C_{l_r}, C_{n_r}, C_{Y_r}$ ) and pure pitching ( $C_{m_q}, C_{L_q}$ ) can be explored using flexible boundaries to manipulate airflow patterns in Fig. (2.19). This method involves gradually reducing the density of upstream drag screens, inducing a velocity variation that matches the curvature radius of the local stream. This

approach is primarily useful in low-speed aerodynamic tests. For example, the NASA Langley 6 ft  $\times$  6 ft curved-flow test section at Virginia Polytechnic Institute, originally from the Langley stability tunnel, emulates a continuous curved-flight condition [34]. The wind tunnel flow is manipulated to curve around a static model, aligning the flow curvature with the model's curvature to create a perpendicular velocity variation relative to the streamlines Fig. (2.19). Flexible side walls and vertical-wire drag screens upstream of the test section are strategically placed to vary in mesh size, optimizing the simulation of pure yawing and pitching movements on a static balance. Simulating steady curved flight has challenges, such as compensating for buoyancy effects caused by static-pressure gradients and the model's boundary layer migration towards the center of curvature. However, these phenomena typically have a minimal influence on accurately measuring purely rotary derivatives in most applications. The curved flow test section, with straight walls, measures 6 feet (1.83 m) by 6 feet (1.83 m) and extends to 22 feet (6.7 m) in length. The vertical walls, made of 0.125-inch-thick (0.31-centimeter-thick) steel and segmented into three parts, allow for fine-tuning of the wall's curvature using jack-screws placed at regular intervals along the test section [35]. To accurately replicate the aerodynamics of a vehicle navigating a curved trajectory, two critical conditions must be satisfied: the airflow surrounding the model must follow a circular path, and the velocity variation along this path should correspond with the local flow curvature radius. This precision is achieved using specifically designed wire screens in the flow upstream of the test section, with variation in wire diameter and spacing across the screen ensuring an accurate velocity gradient.

#### 2.4.2.2 *Model Stationary (Rolling Flow)*

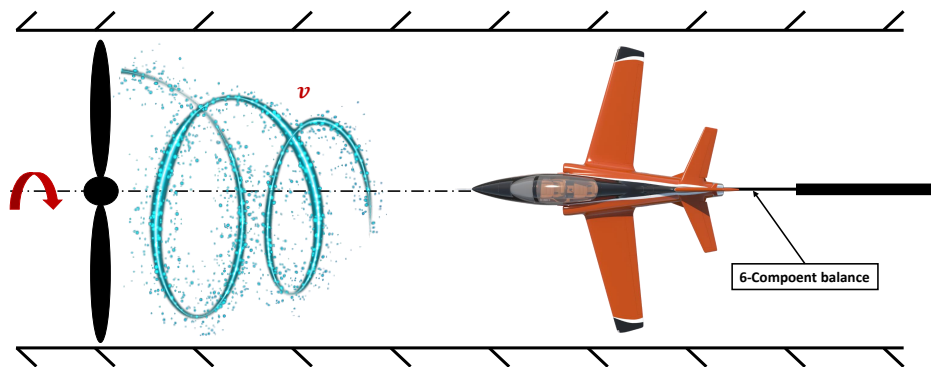


Fig. (2.20) Test section with rotary flow

Innovative approaches to examining continuous rolling derivatives ( $C_{l_p}$ ,  $C_{n_p}$ , and  $C_{Y_p}$ )

involve using a variable-speed rotor with radially extended blade chords to reshape the airflow Fig. (2.20). Contrary to physically rolling the model, this setup creates an aerodynamically distinct condition. The interaction between the induced centrifugal force and the resultant radial pressure differential influences the behavior of the boundary layer on the model. Analyzing responses to rolling maneuvers in a controlled environment requires a fixed model in a rotational stream. Such facilities are available at Virginia Polytechnic Institute and State University, using a 6-foot diameter rolling-flow test section from the NASA-Langley stability tunnel [35]. This test configuration meticulously simulates "pure" roll movements, requiring a rotor setup preceding the testing chamber with nine specially crafted vanes. This arrangement ensures that the peripheral velocity component relative to the tunnel's axis escalates linearly with the radial distance, facilitating a solid core swirling motion within the flow despite in Fig. (2.20). While this model of simulating pure roll maneuvers showcases high fidelity, precision depends on the symmetry of the model and its mount. In asymmetrical scenarios, corrections may be necessary to align with expected aerodynamic behavior. The "rolling flow" or circular test section protocol involves:

- Airflow must encompass the model in a rotational pattern.
- The velocity component orthogonal to the tunnel's axis should proportionally intensify with the radial distance from the central axis.

This specialized setup enhances the understanding of aerodynamic dynamics during roll and supports advancements in aeronautical design and testing methodologies.

#### **2.4.2.3 Model Rotating (Rolling model with parallel straight flow)**

The novel method presented in this study aims to calculate the damping in the roll derivative  $C_{l_p}$ , with the model's rotation being either unrestricted or rigidly constrained. When using deflection through ailerons or fins, this approach measures the resulting rolling velocity, creating a non-coercive yet technically challenging setup. The underlying theory's complexity reflects these practical challenges. In the context of the rigidly forced rotation method, presented in Fig. (2.21), the model is continuously rolled while the reactive aerodynamic moment is precisely recorded using a customized balance. The roll derivative is then directly computed by combining the measured reactive moment with the imposed roll angular velocity. The cross derivative  $C_{n_p}$  can also be determined by positioning a yawing moment balance at the coordinate system's origin, labeled as A. These methods are similar in concept to

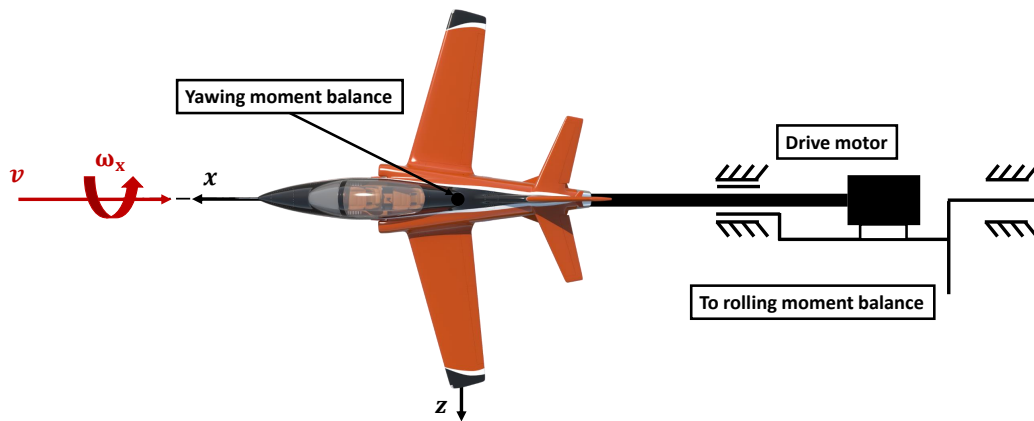


Fig. (2.21) Method of rigidly forced rotation

oscillatory methods, with sub-categories such as constant roll (akin to forced oscillation) and free decay strategies (similar to free oscillation). Fig. (2.22) depicts a steady-state forced-roll

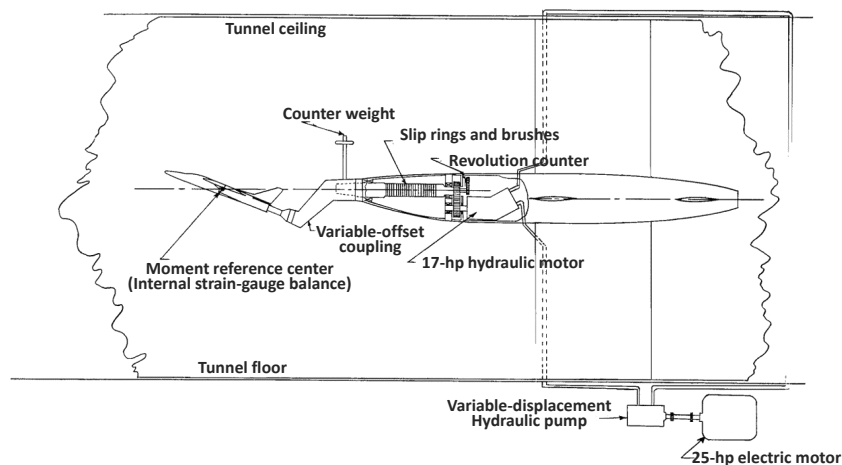


Fig. (2.22) General arrangement of forced-roll apparatus [36]

apparatus designed for use within the NASA-Langley 7 x 10 Foot High-Speed Wind Tunnel. This apparatus is mounted on a six-component strain gauge balance, which is commonly employed in the static assessment of strut-supported models. The design allows for adjustable angles of attack through interchangeable connections between the balance and the rotating sting support. An internal hydraulic motor, characterized by constant displacement and reversible operation, propels the model. Necessary data adjustments are made to compensate for the influence of balance and support deflection under load, centrifugal force effects, and any initial misalignments in the model's center of gravity (CG) relative to the roll axis [36]. In the context of missile and bomb model testing within the 4-Foot-Transonic-Wind Tunnel, a

free-decay roll apparatus has been developed. This system comprises a sleeve driven by a hydraulic motor and positioned on ball bearings atop a six-component balance. Models mounted on this sleeve can accelerate to designated spin rates, after which a pneumatically-operated clutch disengages the drive, allowing free-spinning on the bearings. This phase involves the collection of both spin rate and balance data, with the drive system ensuring a torque delivery of up to 138 lb.in at roll speeds of approximately 5000 rpm [37]. The Department of Aerospace Engineering at the Middle East Technical University has conducted thorough studies on the dynamic stability derivatives of a basic combat aircraft model. Utilizing oscillatory motion in roll within the 8' x 10' low-speed, closed-circuit Ankara Wind Tunnel (AWT), the experiments analyze aerodynamic loads using a five-component internal strain gauge balance. The direct small-amplitude forced oscillation method verifies the balance's signal output, providing a reliable approach for computing fundamental dynamic stability derivatives without the direct solving of motion equations. This system in AWT, initially devised for pitch plane motions, was later adapted for roll plane analyses [38,39].

#### ***2.4.2.4 Model Rotating (Coning)***

The rotational behavior of aircraft has gained significant attention in recent aerodynamics studies, as it requires a thorough representation of motion equations that consider the nonlinear interplay between pitch, yaw, and roll. Rotary or coning motion significantly affects the overall aerodynamic moment, making it a critical element in the equation framework [40]. Experimentally replicating these dynamics involves mounting the model in a wind tunnel on a rotary balance, aligning its axis with the wind tunnel's centerline, and fixing it at specified incidence and sideslip angles. This setup allows for precise control over the model orientation and the introduction of rotational effects. However, the precision and adequacy of overlaying oscillatory pitch or yaw motions on the principal rotational action remain open research questions. Rotary balance experiments contribute to advancements in forced oscillation techniques within the rotary balancing schema. These enhancements target subsonic rate damping characteristics, spin behavior forecasts, and the incorporation of spin dynamics into 6-DOF simulation frameworks. Such integrations enable detailed investigations of "combined motion" or "oscillatory coning," enriching our understanding of aircraft dynamics under complex maneuvering scenarios [41].

NASA-Langley's Full-Scale Tunnel features a state-of-the-art rotational balance

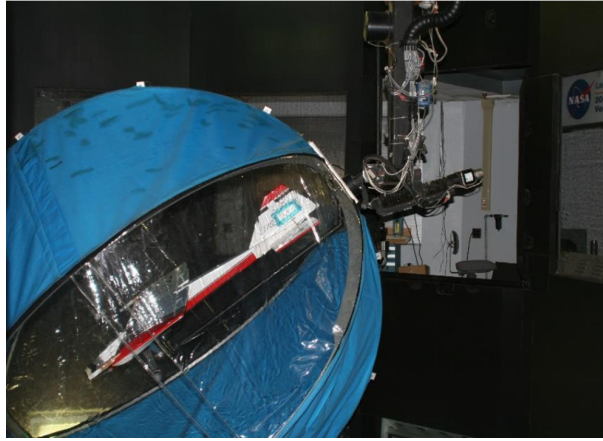


Fig. (2.23) FASER inside the rotary tare bag

apparatus Fig. (2.23) for six-component measurement over an expanded array of attack angles ( $45^\circ$  to  $90^\circ$ ). This device supports experimentation at Reynolds numbers up to  $3 \times 10^6$ , allowing low-speed trials that emulate real-world aerodynamic conditions. The Spin Tunnel at NASA Langley houses a specialized rotary balance for 1:5 scale models, achieving rotational speeds of up to 90 rpm in either direction. The NASA-Ames facility boasts a unique rotary balance for both the 12-foot pressure and 11-foot transonic tunnels, allowing remote adjustments of attack and sideslip angles and facilitating a maximum rotational speed of 400 rpm [42, 43]. In NASA Langley's 20-foot Vertical Spin Tunnel (VST), rotary balance testing involves spinning aircraft models under varied conditions, incorporating different angular velocities, attack angles, and sideslip angles. An internally mounted six-component strain gauge balance accurately measures the resultant forces and moments, while tare measurements within a tare bag control experimental conditions [44]. The rotary testing process is characterized by precise manipulation of the aircraft model, involving both rotation and radial translation within the wind tunnel, while maintaining a constant spin axis relative to the model's center of gravity. This comprehensive test includes sideslip angles ranging from  $-5$  to  $+10$  degrees and attack angles from  $0$  to  $50$  degrees, contributing significantly to the refinement of predictive models and the safe execution of aerial maneuvers.

### **2.4.3 Oscillatory Deflection**

In a comprehensive study, a geometrically similar model is subjected to oscillations in a parallel flow to analyze motion patterns, which help measure stiffening and damping characteristics during oscillatory movements. This method is crucial for understanding damping related to pitch and yaw dynamics, which become more complex with a changing angle of attack

over time  $\frac{d\alpha}{dt} \neq 0$ . The relationship  $C_{m_{\dot{\theta}}} \neq C_{m_q}$  requires reevaluation of traditional methods to accurately isolate  $C_{m_q}$ , particularly under non-stationary conditions. Traditional methods often fail to account for the contributions of the wing and fuselage, affecting the measurement of  $C_{m_{\dot{\theta}}}$ . A refined analysis reveals that

$$C_{m_{\dot{\theta}}} = C_{m_{\dot{\theta}_{wb}}} - C_{m_{\dot{\theta}_{tail}}} \doteq C_{m_{\dot{\theta}_{tail}}}$$

, indicating that the influence of tail on downwash lag is primarily negated after factoring out its unstable lift properties. The equation

$$C_{m_q} = \frac{C_{m_{\dot{\theta}}}}{\left(1 + \frac{d\mathcal{C}}{d\alpha}\right)}$$

offers a method to compute  $C_{m_q}$  by considering the rate of change in the downwash angle at the tail as the aircraft's angle of attack varies. The assumption of minimal wing-body interaction generally applies to configurations with short fuselages and straight wings. However, this assumption may not hold accurately for aircraft with significantly swept or delta wings and long fuselages, particularly in low-speed conditions. The derived pure derivatives are valid only for specific configurations and speed ranges.

### 2.4.3.1 *Measurement of Motion*

Stiffness and damping derivatives are determined by analyzing motion records on a temporal scale, allowing for precise measurement of dynamic properties.

#### 2.4.3.1.1 *Free oscillation*

An initial perturbation is introduced to an elastically constrained model as depicted in Fig. (2.24). Subsequent decaying oscillations are analyzed, with the solution to this scenario expressed as eq. (2.40).

$$I_{zz}\ddot{\theta} + k_{\theta}\dot{\theta} + \sigma_{\theta}\theta = C_{m_{\dot{\theta}}}\dot{\theta} + C_{m_{\theta}}\theta \quad (2.40)$$

Assuming minimal deflections and negligible higher-order derivatives of aerodynamic moments, the solution is eq. (2.40).

$$\theta = \bar{\theta}e^{\lambda t} \quad (2.41)$$

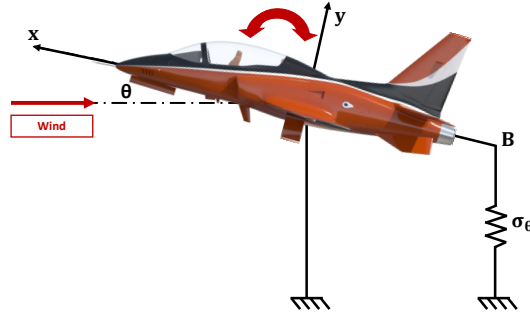


Fig. (2.24) Free oscillation method

Where,

$$\lambda = \mu + jp \quad (2.42)$$

By substituting eq. (2.41) and eq. (2.42) into eq. (2.40) and separating into real and imaginary components, the following expressions are derived:

$$C_{m\theta} = \sigma_{\theta} (p^2 + \mu^2) I_{zz} \quad (2.43)$$

In studies of oscillatory motion, the parameters of frequency, given by  $f = \frac{p}{2\pi}$ , and logarithmic decrement, denoted as  $\delta = -\mu/2f$ , are extracted from recorded motion values  $p$  and  $\mu$ . These parameters provide comprehensive insights into the total moment of inertia  $I_{zz}$ , damping coefficient  $k_{\theta}$ , and the elasticity of angular displacement around the axis,  $\sigma_{\theta}$ . Three distinct methods are employed to modulate the amplitude of the initial impulse in oscillatory motion studies:

1. Mechanically.
2. Release from a displaced position.
3. Electrical stimulation at phase resonance with abrupt circuit break.

Method 3, which involves electrical stimulation at phase resonance followed by an abrupt circuit interruption, is particularly effective for high-frequency testing in systems with highly elastic springs. The simplicity of this method, along with its historical precedence, makes it foundational for analyzing oscillatory derivatives. The decaying oscillations technique does not yield a fixed amplitude; instead, it provides an amplitude range. Modern instruments can narrow this range considerably, facilitating detailed amplitude-dependent studies. This capability is

crucial when examining scenarios that feature slight nonlinear behaviors.

**Single degree of freedom** The University of Bristol developed an innovative single-degree-of-freedom pitch-axis dynamic wind tunnel system, modeled on a 1/16<sup>th</sup> scale of a BAe Hawk aircraft, primarily constructed from fiberglass-coated wood. This state-of-the-art system features specific dimensions and is equipped with aluminum gimbals that enable oscillation across five degrees of freedom, incorporating sophisticated feedback mechanisms to monitor angular position and velocity accurately. The focus of the research was analyzing inverted pitch motion with a defined moment of inertia at  $0.0343\text{kg.m}^2$ . The setup incorporated a DSPACE DS1103 system for data acquisition, alongside MATLAB/Simulink and Real-Time software, functioning at a sampling rate of  $100\text{Hz}$ . The wind tunnel, with a diameter of  $1.1\text{m}$  and capable of achieving velocities up to  $40\text{m/s}$ , was optimized to minimize turbulence to  $1.5\%$  at operational speeds of  $20\text{m/s}$ . This testing condition corresponds to a Reynolds number of  $Re = 0.2 \times 10^6$ , calculated based on the wing chord of the scale model. At the NASA Langley Research Center, a comprehensive evaluation was conducted using the

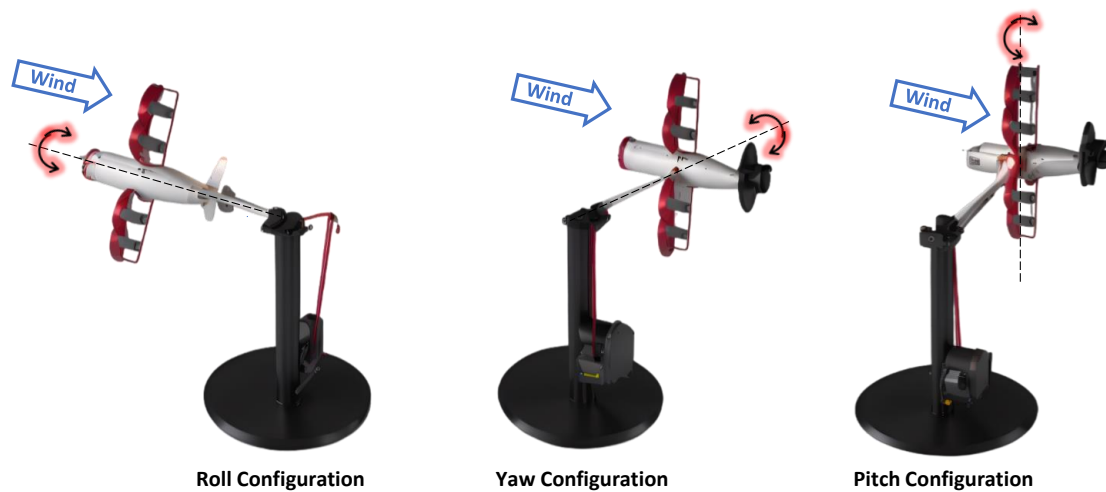


Fig. (2.25) NASA Langley Research Center 14-by-22-Foot Subsonic Wind Tunnel forced oscillation capability

14-by-22-Foot Subsonic Tunnel equipped with a forced oscillation rig in Fig.(2.25) [45]. The experimental setup facilitated complex angular oscillations, allowing the model to exhibit roll, yaw, and pitch movements. The setup consists of a motor and gearbox that drives a flywheel, which in turn manipulates movement through a vertical push rod connected to a crank and

subsequently attached to a sting. The sting is fixed to the aerodynamic model via an internally mounted 6-component strain gauge balance, enabling precise measurement and control over the forces exerted during the tests. The motor's RPM is a critical control variable, adjustable to modify the frequency of oscillation, ranging from 0.1 to 1.0Hz. Additionally, adjustments to the radial location of the pushrod on the flywheel allow for setting the amplitude of oscillation up to 30degrees. The configuration for yaw oscillation mirrors that of the roll; however, the differentiation lies in the attachment point of the sting to either the upper or lower portion of the model, depending on the specific test requirement. For pitch oscillations, the arrangement involves the flywheel being linked to another oscillatory mechanism by employing a yoke structure, facilitating the mounting of the balance, and the pushrod activates rotation of the balance and model about the pivot positioned on the yoke.

**4 degree of freedom** The Department of Aerospace Sciences at Cranfield University has developed a 4-DOF (degrees of freedom) test rig, as documented in [46,47]. The rig consists of a vertically aligned rod supported by bearings, enabling it to rotate around its vertical axis. The rod is secured within a mobile Dexion framework and can be detached from the wind tunnel as a cohesive unit, as depicted in Fig.(2.26). The model is suspended via a gimbal and sleeve,

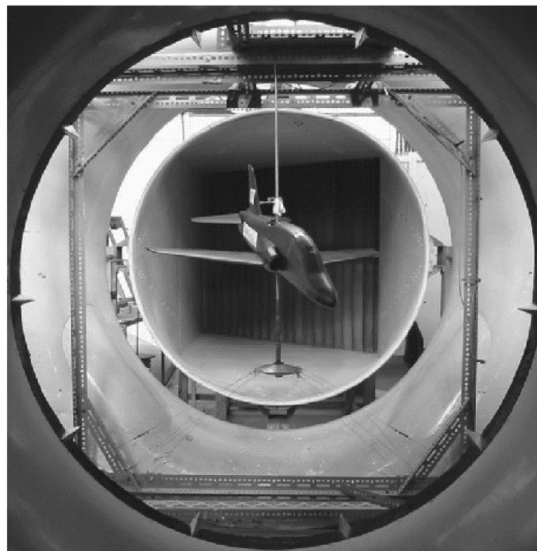


Fig. (2.26) 4-DOF Dynamic wind-tunnel rig with a one-twelfth scale BAe Hawk

which allows for rotation in pitch and roll about the sleeve. The sleeve is keyed to the vertical rod and allows for vertical movement while mandating concurrent rotation. Yaw rotation occurs around the vertical axis, and vertical motion is achieved by the sliding movement of the sleeve along the rod. The angles of motion for each axis are measured using potentiometers, with

movement limits set at 30 degrees. The gimbal-and-rod assembly was innovatively designed to be as compact and lightweight as possible to minimize the model's dependence on the suspension system. To enhance the system's efficiency, all rotational bearings are equipped with small precision ball races, and the sleeve employs precision linear ball bearings. Coil springs at both the upper and lower ends of the vertical rod mitigate impact damage when the model reaches the endpoint stops.

**5 degree of freedom** The University of Bristol has created an advanced 5-DOF (degrees of freedom) test rig, as described in several studies [48–53]. The rig includes a flight vehicle model connected to an arm via a dual-degree-of-freedom gimbal, allowing two types of movement, and a supporting framework connected through a triple-degree-of-freedom gimbal, increasing the model's maneuverability (see Fig. 2.27). An aerodynamic compensation device is placed at the downstream end of the arm to facilitate heave and sway motions of the aircraft model while compensating for the mass, inertia, and aerodynamic disturbances introduced by the supporting arm (see Fig. 2.28). The compensator ensures that

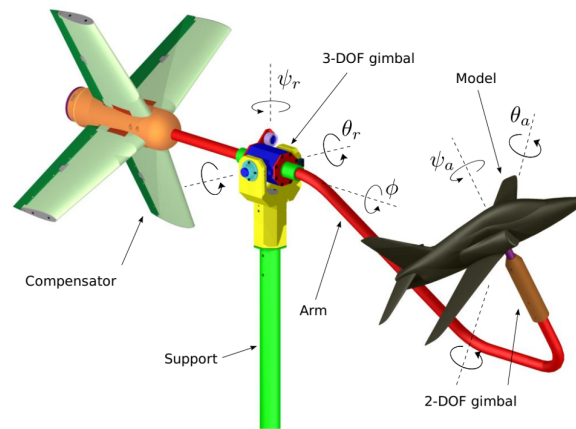


Fig. (2.27) The 5-DOF manoeuvre rig

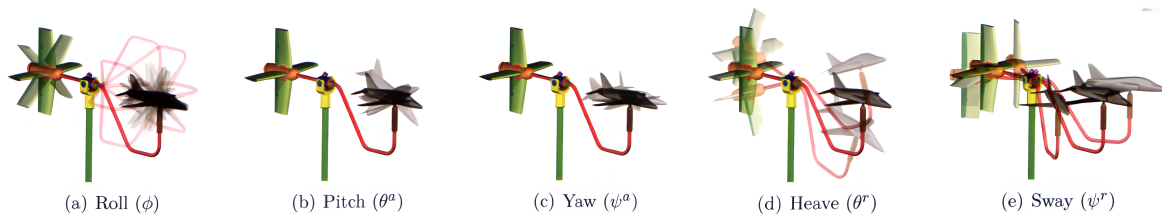


Fig. (2.28) Illustration of the 5-DOF

the pendulum maintains a static balance in the horizontal orientation. All axes of motion on this rig can be locked, offering flexibility in experimental setups. The aircraft model integrated

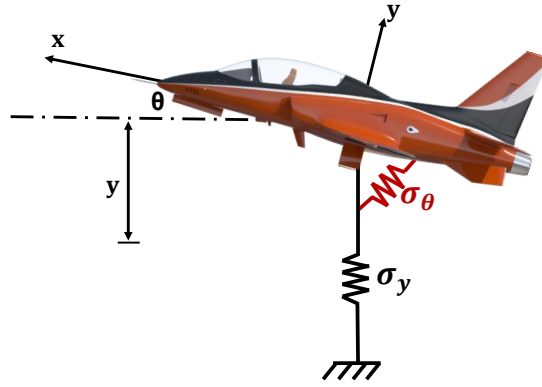


Fig. (2.29) Flutter oscillation method

with this rig must have independently actuating control surfaces and be dynamically scaled to behave like the full-scale aircraft when 'flown' on the arm. Due to the complexity of movements afforded by the rig, describing its behavior involves nonlinear dynamics, necessitating sophisticated mathematical models. A mathematical framework based on the Lagrangian mechanics with constraints has been employed, resulting in a model formulated as a system of differential-algebraic equations. This model incorporates terms to account for friction losses within the gimbals, significantly refining its accuracy. Modifications have been made to adjust for instances when the center of gravity of the flight vehicle model does not align perfectly with the pivot point, further increasing the rig's applicability to a variety of experimental scenarios.

#### 2.4.3.1.2 Flutter oscillation

In flutter dynamics studies, solving flutter equations enables the computation of derivatives, as shown in Fig.(2.29). The experimental setup involves suspending an aerodynamic model to undergo flutter oscillations, allowing for the empirical measurement of flutter characteristics, such as critical wind speed and oscillation frequency at which fully developed flutter occurs. The two-degree-of-freedom experimental apparatus aligns with methodologies described in previous research [54]. During stable flutter, the system's behavior can be mathematically represented, elucidating the dynamic interactions within the system under specific aerodynamic conditions.

$$I_{zz}\ddot{\theta} + k_{\theta}\ddot{\theta} + \sigma_{\theta}\theta + I_{yz}\ddot{y} = C_{m_{\dot{\theta}}}\dot{\theta} + C_{m_{\theta}}\theta + C_{m_{\dot{y}}}\dot{y} + C_{m_y}y \quad (2.44)$$

$$C_m\ddot{y} + k_y\dot{y} + \sigma_y y + I_{yz}\ddot{\theta} = C_{L\dot{\theta}}\dot{\theta} + C_{L\theta}\theta + C_{L\dot{y}}\dot{y} + C_{Ly}y \quad (2.45)$$

The motion can be presented as:

$$\theta = \bar{\theta}e^{jpt} \quad y = \bar{y}e^{j(pt+\varepsilon)} \quad (2.46)$$

In the analysis of flutter dynamics, variables  $\bar{\theta}, \bar{y}$  represent amplitudes and phase shifts, respectively. By integrating equations from eq. (2.46) into eq. (2.44), the process involves segregating the components into real and imaginary subsets, constructing four fundamental equations that encapsulate the eight required derivatives. From the collective set of eight equations, the necessary derivatives for analyzing flutter dynamics are derived, specifically gauged at points of stable amplitude oscillation. However, achieving steady limit cycle oscillations is challenging, and the reliability of results may be compromised in scenarios where aerodynamic derivatives are significantly influenced by wind speed, particularly within the transonic range.

#### 2.4.3.1.3 Elastic Oscillations

In the dynamics analysis framework depicted in Fig. (2.49), a linear spring mechanism is employed to impart harmonic motion to the model under study. The computation of derivatives in this setup hinges on the evaluation of amplitude ratios, specifically between the applied force and the corresponding resonance frequencies. Additionally, this analysis takes into consideration the phase shifts occurring between various movements, allowing for a more nuanced understanding of the system's dynamic response under harmonic excitation. This methodological approach facilitates a detailed exploration of the oscillatory characteristics intrinsic to the model, providing crucial insights into its behavior under specific forced conditions. The mathematical foundation governing the dynamics of the system are encapsulated in the following equation presented herein:

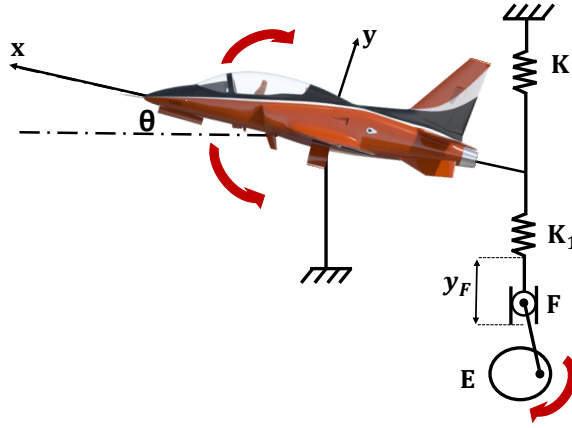


Fig. (2.30) Elastically forced oscillation

$$I_{zz}\ddot{\theta} + k_{\theta}\dot{\theta} + \sigma_{\theta}\theta = C_{m_{\dot{\theta}}}\dot{\theta} + C_{m_{\theta}}\theta + C_{m_F} \quad (2.47)$$

In the governing dynamics of the system, the parameter  $C_{m_F}$  represents the excitation moment coefficient, crucial for understanding the response of the system under external stimuli. Additionally, the coefficients  $C_{m_{\theta}}$  and  $C_{m_{\dot{\theta}}}$  are defined as the stiffness and damping derivatives, respectively. These derivatives play pivotal roles in characterizing the mechanical behavior of the system, as elucidated in the subsequent expressions:

$$C_{m_{\theta}} = \sigma_{\theta} - p^2 I_{zz} - \frac{\overline{C_{m_F}}}{\bar{\theta}} \cos \varepsilon \quad (2.48)$$

$$C_{m_{\dot{\theta}}} = k_{\sigma} - \frac{\overline{C_{m_F}}}{p\bar{\theta}} \sin \varepsilon \quad (2.49)$$

Where

$$\overline{C_{m_F}} = \text{Const } \bar{y}_F$$

In the described dynamic system, the variable  $y_F$  denotes the downward displacement at the juncture where spring  $k_1$  is connected to the exciter, representing the forcing amplitude. Additionally, if the structural coefficients of the system, namely  $(\sigma_{\theta}, k_{\theta}$  and  $I_{zz})$ , are established, it becomes feasible to compute the derivatives as a function of the angular frequency  $p$ , the amplitude ratio, and the phase angle  $\varepsilon$ . To determine these structural coefficients, a series of tests are performed in still air conditions. Initially, the model is attached to capture the model's inertial properties. Subsequent testing without the model

attached serves to ascertain the value of  $k_\sigma$ , assuming  $C_{m_\theta} = 0$ . It is crucial that these tests maintain a consistent amplitude of oscillation  $\bar{\theta}$ , identical to that used during the wind-on tests, to ensure the validity of comparative analyses. Achieving such consistency in amplitude during different test conditions necessitates a specific type of mechanical exciter capable of continual adjustment of amplitude throughout the oscillation process. This precise control facilitates a thorough investigation of the dynamic responses under various simulations and conditions. Consequently, the principal response equations for the spring-tuned system are structured as follows:

$$\left(\frac{\bar{\theta}}{\bar{\theta}_a}\right)^2 = \frac{1 + 4Q^2}{1 + 4Q^2 + 4(1 - \gamma^2)^2 Q^2} \quad (2.50)$$

$$\tan \varepsilon = \frac{2\gamma Q}{1 + 2(1 - \gamma^2) Q^2} \quad (2.51)$$

Where

$$\gamma = \frac{p}{p_a} \quad (2.52)$$

$$Q = \frac{P_a I_{zz}}{k_\theta - C_{m_\theta}} \quad (2.53)$$

The notation 'a' in suffix identifies values specific to amplitude resonance within the discussed dynamic system. The symbols  $p$ ,  $p_a$  denote the angular frequency and the amplitude-resonance frequency respectively. One of the critical parameters in assessing the tuning quality of the system is the Q factor, which quantifies the sharpness of the resonance peak. The response behavior of these frequencies under different Q values can be analyzed through the equations provided in (2.50) and (2.51). At lower operational speeds, the Q factor may register a value around 2.5, whereas at higher speeds, it has the potential to escalate up to 2000. Such data imply that when a system is excited near its resonance frequency, particularly in a finely tuned system, the mechanical oscillator needs to exhibit exceptional stability. Minor deviations in frequency at this finely-tuned state can cause significant fluctuations in both amplitude and phase. These fluctuations tend to make the derivative calculations inaccurate and unreliable. When the system is driven at its amplitude-resonance frequency  $p_a$ , the damping characteristics are framed in the following manner:

$$C_{m_\theta} = k_\theta - \frac{\overline{C_{m_F}}}{p_a \bar{\theta}_a} \frac{1}{\left(1 + \frac{1}{4Q^2}\right)^{1/2}} \quad (2.54)$$

For realistic values of  $Q \geq 2.5$ , it is possible to write

$$C_{m_{\dot{\theta}}} = k_{\theta} - \frac{\overline{C_{m_F}}}{p_a \bar{\theta}_a} \quad (2.55)$$

The phase angle  $\varepsilon$  is not present, obviating the need for its empirical measurement. However, the derivation concerning the stiffness parameter remains pertinent and is articulated as follows:

$$C_{m_{\theta}} = \sigma_{\theta} - p_a^2 I_{zz} \left( 1 + \frac{1}{2Q^2} \right) \quad (2.56)$$

$$C_{m_{\theta}} \simeq \sigma_{\theta} - p_a^2 I_{zz} \quad (2.57)$$

The equation on the right-hand side correlates proportionally with the probability changes in the resonance frequency stemming from aerodynamic loading ( implicitly because  $\sigma_{\theta} \sim p_0^2 I_{zz}$  ), where the suffix "0" denotes conditions observed in still air environments. Testing at low speeds presents notable challenges attributed to the inherent flatness in the tuning response of devices specifically engineered for these measurement tasks. As an alternative approach, stimulation at the resonance frequency can be employed. This method yields the derivatives with a high degree of precision, outlined as follows:

$$C_{m_{\theta}} = \sigma_{\theta} - p_p^2 I_{zz} \quad (2.58)$$

$$C_{m_{\dot{\theta}}} = k_{\theta} - \frac{\overline{C_{m_F}}}{p_p \bar{\theta}_p} \quad (2.59)$$

$p$  signifies a phase resonance condition. To accurately monitor this condition, a device is necessary to indicate when the phase angle  $\varepsilon = 90^\circ$ . Given that the phase angle exhibits rapid changes in response to frequency variations, the resonance frequency can be determined with a high degree of precision.

At NASA's Langley Research Center, an experimental session was conducted within the 12-Foot Low-Speed Tunnel utilizing a dynamic pitch rig, documented in Fig. (2.31). This rig, sophisticatedly controlled via computer and powered by a hydraulic system, is mounted on a C-strut support structure. Within the setup, an internally mounted balance is integrated into the model, facilitating the oscillation of the model around the moment reference center of the balance. This configuration allows the model's angle of attack to reach up to  $85^\circ$ . The dynamic



Fig. (2.31) Dynamic Pitch Motion Test Rig

capabilities of the rig include a maximum pitch rate of  $260 \text{ deg/sec}$  and an acceleration rate of  $2290 \text{ deg/sec}^2$ , enabling it to assess extensive ranges of pitching motions. The rig is designed to handle a variety of maneuvers, including sinusoidal oscillations with different amplitudes and frequencies, constant pitch rate ramp motions, and complex modes consisting of the sum of sinusoidal movements at varying frequencies and amplitudes. For a more detailed description of the dynamic pitch rig's capabilities, refer to the works of Kim and Patrick [55], [56]. During the testing phase, essential data were gathered including pitch angle measurements via an LVDT, six-component force and moment data through a strain gauge balance, and dynamic freestream pressure from a wall-mounted pitot-static probe. Data acquisition was performed at 100 Hz, employing an in-line low-pass anti-aliasing filter. Subsequently, to enhance data accuracy and reduce variability, all recorded data channels underwent digital filtering and multiple test cycles were ensemble averaged.

#### 2.4.3.1.4 Electric Excitation

In the modified setup, an electric vibrator replaces the mechanical exciter and spring  $K_1$ , with a power amplifier providing the necessary energy (See Fig. 2.32). The system features a valve oscillator for output regulation, allowing for continuous amplitude adjustment in response to electrical inputs. This adjustment enhances the precision of determining structural coefficients during static air excitation experiments, particularly in high  $Q$  value environments common in high-speed conditions.

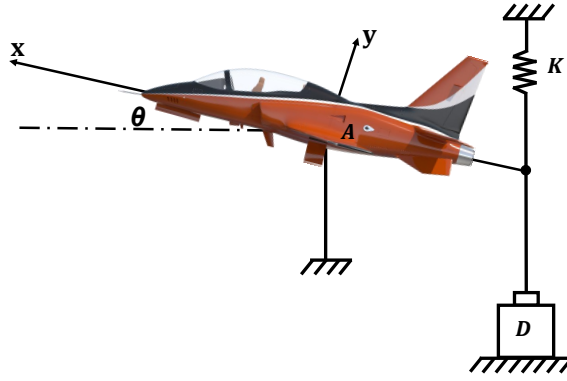


Fig. (2.32) Electric forced excitation test rig

The self-excitation method also captures the input signal for the amplifier directly from a displacement pickup attached to the oscillating system. Moreover, an integrated phase shifter and amplitude stabilizer in the excitation system regulate the excitation current and maintain consistent oscillation amplitude, respectively, unaffected by wind speed fluctuations. This system is particularly effective for finely-tuned systems operating at high speeds and frequencies, as it synchronizes with the system's phase response. When encountering negative aerodynamic damping, inverting the vibrator connection is necessary, which reverses the excitation sign, enabling the driving amplifier to act as a damper, a functionality unattainable through other strategies.

#### 2.4.3.1.5 Excitation with coupled freedom

The system described has two degrees of freedom, with one used to excite the system and observe the response at each resonance frequency. This method assumes that derivative values remain constant concerning the frequency parameter, despite fluctuations in flow and velocity. In practice, models are oscillated on a flexible sting, introducing an additional degree of freedom that cannot be eliminated. The system includes both pitching and diving motions, but when excitations occur in the pitch, eq.(2.44) and eq.(2.45) apply, with the addition of  $C_{m_F}$  to the right-hand side of eq.(2.44)

$$\begin{aligned}
 C_{m_F} &= \overline{C_{m_F}} e^{jpt} \\
 \theta &= \bar{\theta} e^{j(pt - \epsilon_\theta)} \\
 y &= \bar{y} e^{j(pt - \epsilon_y)}
 \end{aligned}
 \tag{2.60}$$

Applying eq.(2.60) into eqs.(2.44) and (2.45) yields a set of four equations, encompassing eight derivatives that can be determined by analyzing these equations at two distinct resonance frequencies. The type of excitation can be either mechanical or electrical, but the motion must remain free from flutter when not externally stimulated.

#### 2.4.3.1.6 Cross oscillations

The linked freedom excitation method is applied to calculate the damping cross derivatives  $C_{l_r}$  and  $C_{n_p}$ , as depicted in Fig. (2.33). This technique involves initiating oscillations at resonance around one axis and analyzing the motion dynamics on both the excited axis and the orthogonal axis. For instance, rolling oscillations are induced to determine  $C_{n_p}$ .

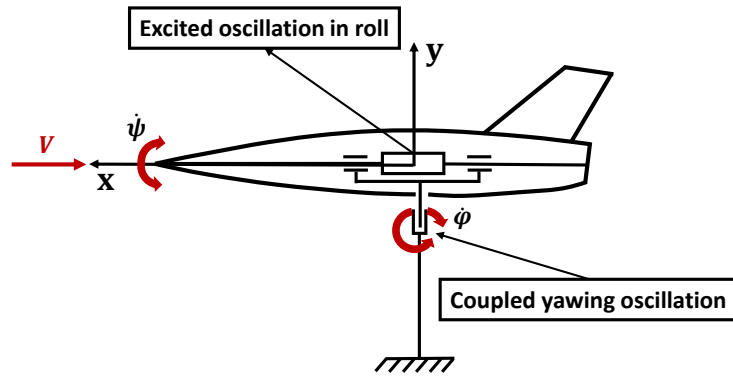


Fig. (2.33) Cross oscillation excitation test rig

During the analysis, the excitation frequencies and coupling motions are synchronized, with their phase differences eliminated. At this stage, the opposing forces of aerodynamic and mechanical damping from yaw counteract the aerodynamic yaw moments generated by roll. This equilibrium is achieved by equalizing the left and right quadrature components, as shown in eqs.(2.61) and (2.62).

$$I_{yy}\ddot{\psi} + k_{\psi}\dot{\psi} + \sigma_{\psi}\psi - I_{xy}\ddot{\phi} = C_{n_{\psi}}\dot{\psi} + C_{n_{\phi}}\dot{\phi} + C_{n_{\psi}}\psi + C_{n_{\phi}}\phi \quad (2.61)$$

$$I_{yy}\ddot{\phi} + (k_{\psi} - C_{n_{\psi}})\dot{\psi} + (\sigma_{\psi} - C_{n_{\psi}})\psi - I_{xy}\ddot{\phi} = C_{n_{\psi}}\dot{\phi} + C_{n_{\phi}}\phi \quad (2.62)$$

$$(k_{\psi} - C_{n_{\psi}})\dot{\psi} = C_{n_{\phi}}\bar{\phi} \quad (2.63)$$

The amplitudes  $\bar{\psi}$  and  $\bar{\phi}$  are extracted from motion data, and the direct derivative  $C_{n_{\psi}}$  is calculated using established procedures. This directly leads to determining  $C_{n_{\phi}}$ , which is then equated to  $C_{n_p}$ .

### 2.4.3.2 *Measurement of Forces*

When examining oscillatory behavior, derivatives are calculated based on the forces applied to the model, employing force pickups integrated within the drive linkage. Further techniques focus on identifying optimal rigs for estimating these derivatives accurately. This process is crucial for understanding and predicting the dynamic behavior of the system under investigation.

#### 2.4.3.2.1 *Free oscillation*

When assessing lift, a force pickup is strategically positioned at the oscillation axis, as depicted in Fig (2.34). This setup facilitates the measurement by tapping directly into the motion's pivot point. As

$$\theta = \bar{\theta} e^{\mu t} \sin pt$$

As  $p$  is the angular frequency. The lift force may be written as:

$$C_L = \bar{C}_L e^{\mu t} \sin(pt + \varepsilon) = C_{L_{\theta}} \theta + C_{L_{\dot{\theta}}} \dot{\theta}$$

The derivatives are then given by:

$$\begin{aligned} \bar{C}_L \cos \varepsilon &= \bar{\theta} (C_{L_{\theta}} + \mu C_{L_{\dot{\theta}}}) \\ \bar{C}_L \sin \varepsilon &= \bar{\theta} p C_{L_{\theta}} \end{aligned} \tag{2.64}$$

The value

$$\frac{\bar{C}_L}{\bar{\theta}} = \frac{C_{L_1}}{\theta_1} e^{\mu \varepsilon / p}$$

Using a torsion spring  $K$ , elastic forces in reactions can be eliminated to precisely capture peak values  $C_{L_1}$  and  $\theta_1$ , differentiated by phase angle  $\varepsilon$ . As shown in Fig.(2.36), the BAe Hawk model is mounted on a 1- and 2-degree-of-freedom (DOF) rig, allowing for pitch and swing movements via its pendulum strut placement and a bearing at the strut's top. The configuration, complemented by actuated stabilators, facilitates flight simulations within a 3'6" diameter open-jet wind tunnel, achieving a pitch range up to 40 degrees. Additionally, the

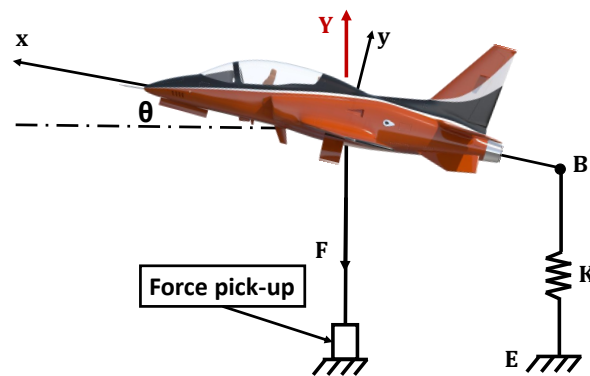


Fig. (2.34) Free oscillation method with force measuring test rig

support structure ensures reduced stress, lowering sting interference and enhancing test accuracy. The model can also be tested under different conditions using the department's 7 ft. by 5 ft. closed-section tunnel which can be adapted with the necessary equipment for expanded testing capabilities. To enhance unsteady aerodynamics research, it's beneficial to assess the aerodynamic reaction to discern the time lag in load-response scenarios. The implementation of two advanced flexures, specifically the 'binocular' configuration strain gauge balance installed at the strut's midpoint and the 'ring' balance—seamlessly incorporated with the model's gimbal inside the fuselage—facilitates this process. These components were designed considering the challenges posed by the strut's bending loads and are crucial for the integrity of flexure design. Utilizing finite element analysis in the design phase and strain data from the strut's apex, a rigorous calibration is achieved. A 1/16th-scale BAe Hawk, with a 600 mm wingspan and 1.2 kg weight, is the initial aircraft model developed to operate on this 2-DOF system. Bristol developed an efficient three-degree-of-freedom rig in Fig.(2.37) to evaluate aircraft stability derivatives, employing a gimballed mechanism and piezoelectric balance for force and moment capture. Minor modifications enabled comprehensive static and dynamic derivative collection. In static tests, a DC motor and leadscrew adjusted the model's pitch, constrained by a pitch arm and stoppers, achieving a 15 to 25-degree range, ensuring roll and yaw stasis. A digital inclinometer, cross-checked via dSpace, calibrated pitch within a one-degree margin. For dynamic tests, these constraints were removed, allowing free movement along all axes, with forces measured using a Kistler balance during motion [58]. Fig.(2.38) illustrates the complex structure of the 3-DOF gimbal consisting of dual nested

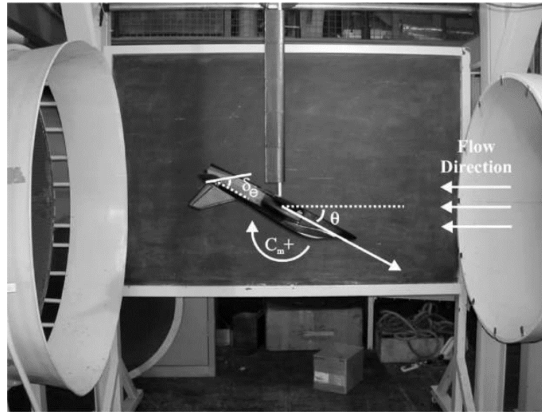


Fig. (2.35) Hawk model mounted inverted to 1-DOF rig



Fig. (2.36) 1-16th-scale Hawk Model on 2-DOF test rig [57]

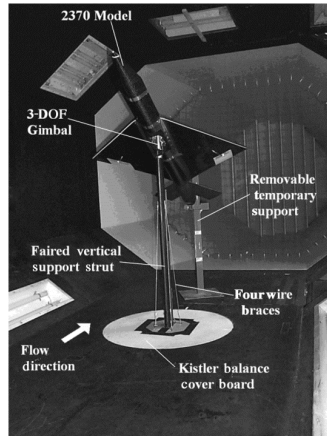


Fig. (2.37) The Bristol 3-DOF dynamic test rig

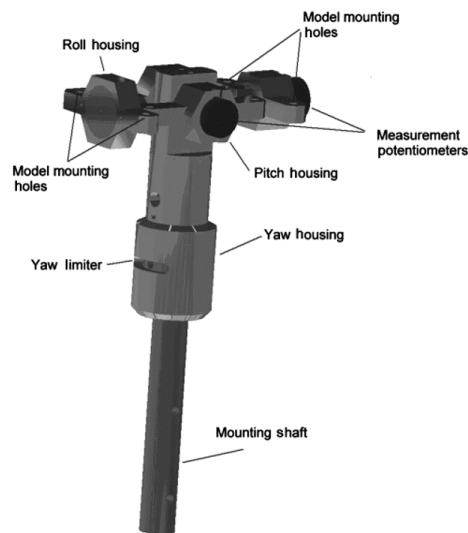


Fig. (2.38) 3-DOF gimbal

main frames and precise ball bearings facilitating pitch and roll movements. A separate yaw housing with thrust bearings permits unrestricted yaw while enduring aerodynamic forces. Accurate Penny and Giles potentiometers recorded angular movements along all three axes. Positioned inside the yaw housing, the yaw potentiometer connected directly to the mounting axis. The gimbal's rotational limits were set to 45 degrees for both pitch and roll, and 35 degrees for yaw. To protect the gimbal bearings, semirigid padding buffered the fuselage slot. Due to the large cutout needed for gimbal movement, potential cavity impacts on results were noted, though not explored. Stability derivatives were calculated by numerically differentiating angular positions to derive rates and accelerations necessary for motion equations [?].

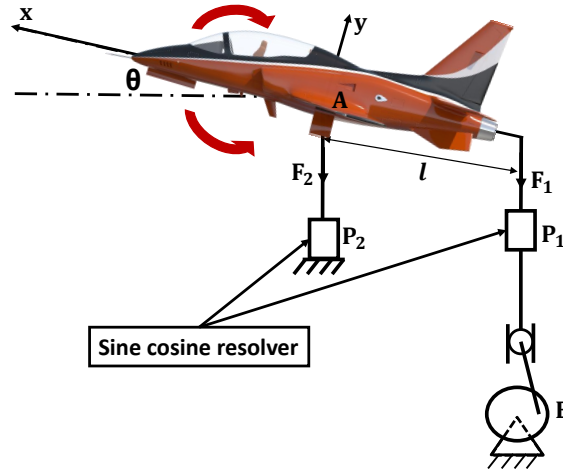


Fig. (2.39) External rigid drive

#### 2.4.3.2.2 External rigid drive

In the depicted configuration, as illustrated in Fig (2.39), the model experiences rotation around a fixed axis at point A and is energized at point B through a solid linkage to an excitation system at point E. Measurements of the vertical force reaction  $F_2$  at A are taken by detector  $P_2$ , while the excitation force  $F_1$  is recorded by sensor  $P_1$  situated in the activating link. This arrangement allows for the determination of the movement equation relative to axis A.

$$I_{zz}\ddot{\theta} + k_{\theta}\dot{\theta} = lF_1 + C_{m_{\dot{\theta}}}\dot{\theta} + C_{m_{\theta}}\theta \quad (2.65)$$

For analytical accuracy in aerodynamics, these equations incorporate structural terms, such as inertial responses, established under controlled conditions without wind. Since inertial effects become pronounced in high-speed, high-frequency tests—often overshadowing precise force measurements—it's critical to balance out these inertial forces despite the experimental difficulties posed. By selecting forced movements that blend rotational and translational actions while maintaining a constant alignment against the airflow, we're able to isolate derivatives like the pure pitch  $C_{m_q}$  and pure yaw  $C_{n_r}$  from the characterized "snaking motion" of the model under test conditions.

#### 2.4.3.2.3 Internal rigid drive

The experimental setup ensures exclusive detection of aerodynamic loads through strategically positioned force pickups. Integrated onto a durable floating frame, the

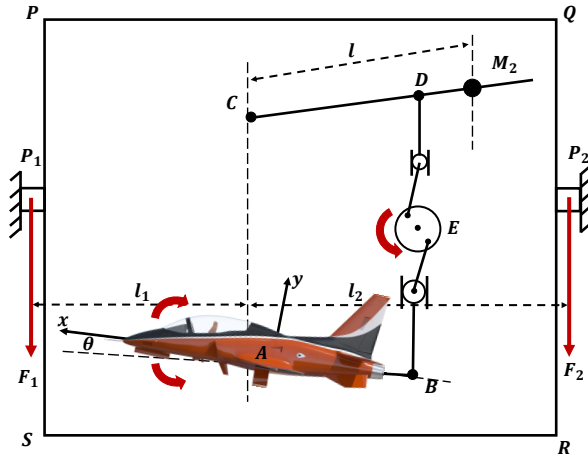


Fig. (2.40) Internal rigid drive

arrangement incorporates the model, an oscillation mechanism, and the drive motor, as shown in Fig. (2.40). This frame is meticulously designed to prevent any out-of-plane movement. Force pickups, labeled  $P_1$  and  $P_2$ , robustly anchor the frame to the ground, effectively resisting any planar motion while accurately recording forces  $F_1$  and  $F_2$  within the plane and orthogonal to the airflow. Additionally, a mass designated  $M_1$  has been employed to equilibrate inertial forces, with all frictional forces effectively confined within the setup. In a condition of equilibrium

$$\begin{aligned} C_{L_\theta} \dot{\theta} + C_{L_\theta} \theta &= F_1 + F_2 \\ C_{m_\theta} \dot{\theta} + C_{m_\theta} \theta &= F_1 l_1 - F_2 l_2 \end{aligned} \quad (2.66)$$

The derivatives are given directly by

$$\begin{aligned} C_{L_\theta} \bar{\theta} &= \bar{F}_1 \cos \epsilon_1 + \bar{F}_2 \cos \epsilon_2 \\ C_{L_\theta} p \bar{\theta} &= \bar{F}_1 \sin \epsilon_1 + \bar{F}_2 \sin \epsilon_2 \\ C_{m_\theta} \bar{\theta} &= \bar{F}_1 l_1 \cos \epsilon_1 - \bar{F}_2 l_2 \cos \epsilon_2 \\ C_{m_\theta} p \bar{\theta} &= \bar{F}_1 l_1 \sin \epsilon_1 - \bar{F}_2 l_2 \sin \epsilon_2 \end{aligned} \quad (2.67)$$

The substantial dimensions of the frame require the use of force pickups characterized by high stiffness and consequently low sensitivity. This configuration is particularly apt for recording large forces at low frequencies, typical of scenarios involving high subsonic velocities with a low-frequency parameter. The mechanical layout of the system is specifically tailored for half-model testing, where the frame is positioned near and parallel to the test section wall,



Fig. (2.41) Parts of the AWT Test Rig

arranging the components on one side while the model extends into the wind stream on the other.

In the Ankara Wind Tunnel, dynamic stability derivatives are ascertained for a generic combat aircraft model undergoing oscillations, employing a direct forced oscillation method cited in relevant literature. Dubbed the AGARD Standard Dynamic Model, this prototype serves as a benchmark for calibrating different measurement techniques across NATO's wind tunnels. Aerodynamic forces and moments are meticulously gauged using an internal strain gauge balance embedded in the model. The design and assembly of the testing apparatus are illustrated in Fig. (2.41). The model's harmonic motion in the pitch plane is engendered by a drive mechanism situated beneath the wind tunnel's test section flooring. This drive is operated by a DC-servo motor, instigating a crank-rod system that interlinks with a fluctuating vertical rod supporting the model. Model oscillation amplitude is modulated via an adjustable flywheel eccentricity radius, permitting variations up to 50 mm, equating to a mid-range oscillation pitch angle of  $5^\circ$ .

#### 2.4.3.2.4 Electric Excitation

Fig. (2.42) illustrates the substitution of the mechanical exciter  $E$  (as shown in Fig. (2.39)) with an electric vibrator  $D$ . This vibrator is powered by a valve oscillator and a power amplifier, with a spring  $K$  added to balance inertial responses. This modification allows for improved control over the oscillation's frequency and amplitude, which is advantageous for

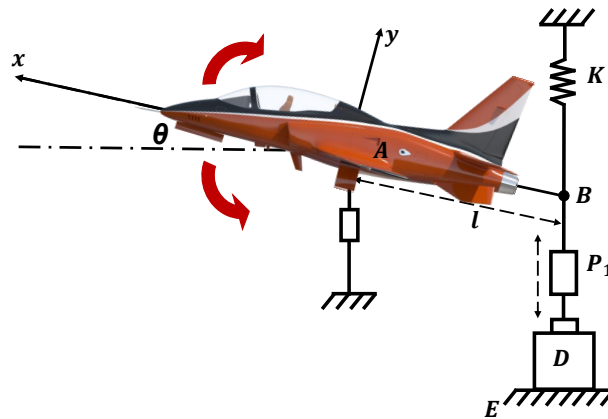


Fig. (2.42) Electrically excited oscillation for system with force pick-ups

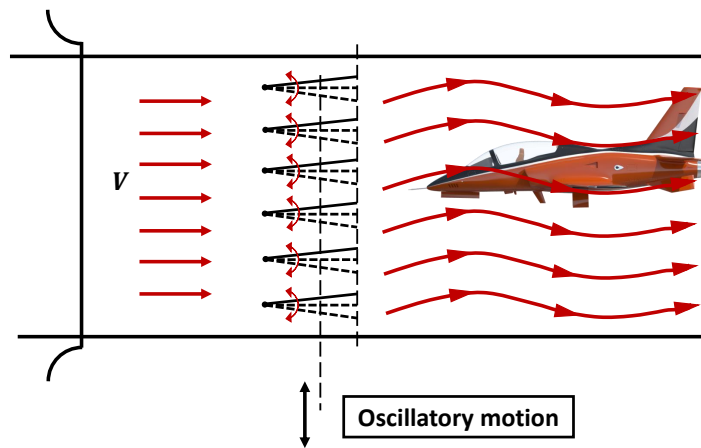


Fig. (2.43) Test section with oscillatory flow

tailored processes in high-speed testing environments [54].

#### 2.4.3.2.5 Fixed Model in Oscillatory Flow

An oscillatory flow within the test section is generated through methods such as a longitudinally vibrating bump on the tunnel wall or a collection of oscillating vanes placed before the model shown in Fig. (2.43). These techniques are essential for the measurement of oscillatory derivatives on static models within the test section. Ascertain the optimal configuration of the oscillating flow presents a significant challenge.

#### 2.4.4 Free Flying Wind Tunnel Tests

The evaluation of aerodynamic derivatives is performed in free flight wind tunnels, eliminating the need for balances. The procedure involves a model controlled by two or three

operators who adjust variables such as wind speed, tunnel inclination, engine thrust, and model control settings. Initially, settings are optimized to achieve equilibrium; subsequently, controls are manipulated remotely to provoke the model's response, which is recorded by three film cameras positioned in three orthogonal planes. Derivatives are derived from the model's transient response to these adjustments. Assessment is typically categorized into longitudinal and lateral derivatives. The successful execution of the test demands that the model be both dimensionally and dynamically representative, presenting substantial challenges in its design and construction.

#### **2.4.4.1 *Free Flying***

The conduct of captive-model dynamic-stability tests in wind tunnels faces significant hurdles primarily due to:

- Interference and vibrations from mechanical model supports.
- The limitation of mechanical supports in replicating free model motions.

To mitigate these issues, innovations in wind-tunnel testing methodologies have emerged, involving:

- Initiating tests via launching models into wind-tunnel flows for free flight within the test section.
- Utilizing remotely controlled models connected by a flexible control-and-safety cable.
- Employing cable-suspension to allow models the freedom of motion across five degrees of freedom, excluding longitudinal translation.
- Implementing magnetic suspension and actuation for model stabilization and control.

The modification of the NAE helium-hypersonic-wind-tunnel to incorporate the free-flight method represents a significant advancement in testing technologies. This approach utilizes a pneumatic launcher to project injection-molded polystyrene models into the tunnel. Data capture during these tests is facilitated by high-speed film technology, recording at an impressive rate of 3000 to 4000 frames per second. This optical setup enables simultaneous observation of the model in two perpendicular planes within a single frame [59], enhancing the comprehensiveness and accuracy of the data collected. The pitch-jet launch system enables the model's initial launch at a minimal angle from the launch gun axis, rapidly achieving high

angular velocity post-release; thus, reaching optimal attack angles near the observation zone without trajectory compromise. Prior to launch, the model may be spun on a spindle, with air jets on the launch head imparting necessary angular velocities. Alternatively, the shot-put launch employs a rail system allowing fin-guided adjustments from 0 to 90 degrees, replacing the spindle. Detailed methodologies for these free flight strategies in wind tunnels are discussed in the referenced literature [59–62]. The NASA-Langley-Full-Scale-Wind-Tunnel, featuring a 30 ft x 60 ft open test section, is optimally designed for the flight testing of large powered models, typically around 4 ft in span [63]. The facility equips three operators to manage electric and pneumatic power alongside command signal transmission to the models via a flexible cable. Included with this cable is a small steel safety line which, running through a pulley system, allows for model retrieval during instances of uncontrollable motion or mechanical failure. Throughout the tests, this cable remains slack and is supervised by a dedicated safety cable operator. Test outcomes predominantly include stable high-angle-of-attack flights, tests on pilot control methods under similar conditions, and artificial rate dampening studies, primarily assessed qualitatively through pilot experiences and film documentation.

#### **2.4.4.2 Free Spin**

Dynamically scaled models in the Vertical Spin Tunnel (VST) primarily serve to investigate aircraft spin behaviors and characteristics essential for designing emergency recovery systems, as depicted in Fig. (2.44). These models are introduced into the tunnel with an initial rotation and launched at high angles of attack into an upward airflow. The VST operator then adjusts airflow speed to align with the model's rate of descent. Throughout these tests, the aircraft may exhibit various spin modes where its orientation and rotational speed either stabilize or fluctuate around average values, depending on the existing aerodynamic conditions.

#### **2.4.4.3 Free Tumble**

Tumble testing, akin to free-spin testing, is applied to flying-wing and other unconventional aircraft designs, as highlighted by Fremaux [64]. Unlike spinning models that move vertically, tumbling models exhibit net lift, precluding a vertical trajectory and thus limiting the duration of their traversal through the test zone. To extend test durations, a "free-to-pitch" rig is employed, which restricts the model's movement to rotation around the pitch axis (1-DOF), allowing for the performance of tests of varying lengths.



Fig. (2.44) Free-spin test of dynamically-scaled fighter model

## **Chapter 3**

### **Development the AeroMech tool for rapid estimation of airplane aerodynamic characteristics during early design stages**

#### **3.1 Background and Overview of the AeroMech Tool**

This section introduces the AeroMech tool, a MATLAB-based software designed to quickly estimate the aerodynamic characteristics of subsonic fixed wing airplanes and their components during the initial stages of design. AeroMech has undergone three years of development and over a year of testing and validation. The tool utilizes empirical and semi-empirical methods, along with simplified engineering methods, which are computationally efficient and rapid. Despite their simplicity, these methods have been shown to provide sufficient accuracy for use during the early design stages, as compared to traditional computational fluid dynamics and experimental testing. Numerous test cases have demonstrated the effectiveness of AeroMech in estimating aerodynamics under different conditions. AeroMech is capable of accurately estimating various aerodynamic characteristics for aircraft and their components, These estimations have been validated against experimental data, numerical, semi-empirical and other reliable prediction methods. The validation study has confirmed that AeroMech can be employed as a standalone tool or in conjunction with other advanced methods for the design optimization of aircraft during the early stages of development. The tool offers the capability to rapidly estimate various aerodynamic aspects of subsonic airplanes and their parts, including lift, pitching moment, pressure distributions, drag polars at off-design conditions, and the effects of control surfaces, such as deflection angle, hinge moment, and control effectiveness. In the early stages of aircraft design, it is crucial to have quick and efficient methods for estimating aerodynamic characteristics. AeroMech, a new tool introduced in this study, incorporates various empirical and semi-empirical methods, as well as engineering techniques, which are computationally cost-effective, rapid, and generally offer adequate accuracy for use in the initial design stages. The software is designed to be user-friendly, with detailed instructions and guidelines provided for its use and further development.

## **3.2 Critical Role of Early Design Stage Analysis**

In the design process, the use of efficient methods that match the accuracy of high-fidelity techniques is more likely to be adopted. Bridging the gap between rapid methods and high-fidelity methods. AeroMech, an open-source toolbox, exemplifies this approach by combining potential flow solvers and high-fidelity solvers (commonly semi-empirical technique) to estimate aerodynamic characteristics swiftly and accurately. The potential flow models swiftly predict aerodynamic loads.

The early stages of aircraft design necessitate the ability to evaluate aerodynamic characteristics swiftly and precisely, as these results significantly contribute to the overall aircraft design. Over the years, fast methods such as semi-empirical, empirical have been employed to evaluate the aerodynamic characteristics of aircraft. Although these methods are rapid, they may not offer the necessary accuracy. Conversely, high-fidelity methods like computational fluid dynamics with grid-based or grid-free methods provide precise outcomes at the cost of substantial computational effort. Recently, this tool reducing computational cost and allowing for the rapid analysis of not only aerodynamic forces but also flow physics. This facilitates the design and exploration of the design space.

The objective of this section is to outline a procedure for developing a tool that enables designers to gain a comprehensive understanding of an airplane's aerodynamic characteristics using the limited data typically available during the early stages of design. The targeted aerodynamic characteristics include the lift, drag, and pitching moment coefficients, as well as the following derivatives: speed, angle of attack, angle of sideslip, rate of angle of attack, rate of angle of sideslip, roll rate, pitch rate, and yaw rate. To achieve this, all necessary analytical-empirical equations are implemented into a Matlab code. Additionally, a large number of empirical charts are digitized and incorporated into this code to streamline the calculation process, making it more efficient and user-friendly. Figure 3.1 presents a flowchart that describes the main steps for predicting the airplane's aerodynamic characteristics. The subsequent subsections explain these main steps in detail.

## **3.3 Drag Coefficient Prediction**

### ***3.3.1 Wing Drag Coefficient Prediction***

The wing drag coefficient is a fundamental parameter in evaluating the overall drag force acting on an aircraft. This section presents a methodology for predicting the wing drag

coefficient during the preliminary design phase, with a particular focus on airplanes that feature essentially straight, tapered wings. The total wing drag coefficient, denoted as  $(C_{D_{wing}})$ , is derived from two primary components: the wing zero-lift drag coefficient  $(C_{D_{0w}})$  and the wing drag coefficient attributable to lift  $(C_{D_{Lw}})$ . The wing zero-lift drag coefficient is affected by several factors, including the interference between the wing and fuselage, the correction factor for lifting surfaces, as well as the turbulent flat plate friction coefficient of the wing. These parameters can be quantified using empirical data and established correlations. On the other hand, the wing drag coefficient due to lift is influenced by the wing lift coefficient, the aspect ratio of the wing, the span efficiency factor, and the induced and zero-lift drag factors associated with linear twist. These elements are combined to determine the overall contribution of lift-induced drag to the total wing drag coefficient.

$$C_{D_{wing}} = C_{D_{0w}} + C_{D_{Lw}} \quad (3.1)$$

$$C_{D_{0w}} = (R_{wf}) (R_{LS}) (C_{fw}) \{1 + L'(t/c) + 100(t/c)^4\} S_{wetw}/S \quad (3.2)$$

$$C_{D_{Lw}} = (C_{Lw})^2 / \pi A e + 2\pi C_{Lw} e_t v + 4\pi^2 (\epsilon_t)^2 w \quad (3.3)$$

### 3.3.2 *Prediction of Fuselage Drag Coefficient*

The fuselage of an aircraft plays a pivotal role in contributing to the overall drag the aircraft experiences. We will detail a methodology for predicting the fuselage drag coefficient during the preliminary design phase. The total fuselage drag coefficient, denoted as  $(C_{D,fus})$ , is comprised of two main components: the fuselage zero-lift drag coefficient  $(C_{D,o,fus})$  and the fuselage drag coefficient due to lift  $(C_{D,L,fus})$ . The fuselage zero-lift drag coefficient is influenced by several factors, including the interference between the wing and fuselage, the turbulent flat plate skin-friction coefficient of the fuselage, and the base drag coefficient of the fuselage. These parameters can be quantified using empirical data and established correlations. In contrast, the fuselage drag coefficient due to lift is determined by the fuselage angle of attack, the planform area of the fuselage, and the ratio of the drag of a finite cylinder to the drag of an infinite cylinder. These factors are integrated to calculate the overall contribution of lift-induced drag to the total fuselage drag coefficient.

$$C_{D_{fus}} = C_{D_{o_{fus}}} + C_{D_{L_{fus}}} \quad (3.4)$$

$$C_{D_{o_{fus}}} = R_{wf} C_{f_{fus}} \left( 1 + 60 / (1_f / d_f)^3 + 0.0025 (1_f / d_f) \right) s_{wet_{fus}} / s + C_{D_{b_{fus}}} \quad (3.5)$$

$$C_{D_{L_{fus}}} = 2a^2 s_{b_{fus}} / s + \eta c_{dc} a^3 s_{plf_{fus}} / s \quad (3.6)$$

### 3.3.3 Empennage Drag Coefficient Prediction

In the context of subsonic flight, the drag coefficient of the empennage can be determined by examining the individual contributions of each empennage component. These components typically encompass the horizontal stabilizers, canard surfaces, and vertical stabilizers, with their specific configurations varying considerably based on the aircraft design. To calculate the zero-lift drag coefficient for each empennage component, a methodology analogous to that used for the wing is employed, but with the relevant empennage parameters substituted. This approach ensures that the distinctive attributes of empennage surfaces, such as sweep angles, aspect ratios, and thickness ratios, are accurately accounted for in the drag estimation process. Furthermore, the drag coefficient associated with the lift generated by the empennage surfaces is also taken into consideration. For horizontal stabilizers and canards, the induced drag due to the lift they produce is calculated based on their respective lift coefficients and aspect ratios. In contrast, for vertical stabilizers, their contribution to induced drag is typically minimal unless the aircraft is experiencing significant sideslip conditions. By systematically evaluating the distinct drag components of each empennage surface, a thorough understanding of the overall subsonic empennage drag coefficient is achieved. This methodical approach facilitates accurate predictions of the aircraft's performance and stability characteristics, which are essential in the design and optimization process.

$$C_{D_{emp}} = \text{SUM}_i \left\{ (C_{D_0})_i + (C_{D_{L_{emp}}})_i \right\} \quad (3.7)$$

### 3.3.4 Nacelle/Pylon Drag Coefficient Prediction

In the subsonic speed regime, accurately predicting the drag coefficient for nacelle and pylon configurations involves a comprehensive multi-step process. This approach is designed to thoroughly account for the interference effects between the nacelle, pylon, and other aircraft components, thereby yielding a more precise estimation of the overall drag. The initial step

involves determining the subsonic installed drag increment attributed to the nacelle or the combined nacelle and pylon assembly. This drag increment captures the interference effect arising from the installation, which can significantly influence the aircraft's performance metrics. Additionally, this methodology accounts for the impact of engine or propeller stoppage, which can introduce supplementary drag due to windmilling or propeller drag. These effects are analyzed separately and incorporated into the overall nacelle/pylon drag coefficient.

$$C_{D_{np}} = C_{D_n} + C_{D_p} \quad (3.8)$$

### ***3.3.5 Flap Drag Coefficient Prediction***

In the subsonic speed regime, accurately predicting the drag coefficient associated with the deployment of flaps on an aircraft is of paramount importance. This task necessitates a thorough evaluation of the various components contributing to the overall flap drag, thereby offering a comprehensive understanding of the aircraft's performance characteristics. The total flap drag coefficient is composed of three primary elements: the flap profile drag increment, the induced drag increment due to the flap, and the interference drag increment due to the flap. By meticulously examining each of these components, researchers and designers can precisely estimate the impact of flap deployment on the aircraft's overall drag. The flap profile drag increment is determined based on the specific type of flap employed, such as plain flaps, single-slotted flaps, or double-slotted flaps. Each flap configuration possesses its own unique drag characteristics, which are accounted for through the application of empirical data and correlation methods. The induced drag increment resulting from flap deployment is calculated based on the additional lift generated by the flaps. This additional lift alters the overall lift distribution on the wing, subsequently affecting the induced drag. Lastly, the interference drag increment due to the flap is evaluated. The presence of the flap can modify the flow patterns around the wing and adjacent aircraft components, thereby introducing additional drag. By systematically considering these three distinct drag components, researchers and designers can develop a comprehensive understanding of the flap drag coefficient in the subsonic speed regime. This knowledge is crucial for optimizing the aircraft's performance, ensuring efficient operation, and enhancing the overall design.

$$C_{D_{\text{flap}}} = \Delta C_{D_{\text{prof}}} + \Delta C_{D_i} + \Delta C_{D_{\text{int}}} \quad (3.9)$$

### 3.3.6 Landing Gear Drag Coefficient Prediction

Predicting the drag coefficient associated with an aircraft's landing gear is a critical element in the overall drag analysis, particularly within the subsonic speed regime. The total landing gear drag coefficient is calculated by first determining the individual drag coefficients of each landing gear component, such as the main gear and nose gear. These individual drag coefficients are then aggregated, taking into consideration the relative sizes and reference areas of the respective components. The drag coefficient of each landing gear component is significantly influenced by its geometric characteristics, such as tire width, tire diameter, and the presence of fairings or aerodynamic streamlining. Empirical data and correlation methods are utilized to estimate the drag coefficient of these individual components, ensuring a precise representation of their contributions to the overall landing gear drag. Furthermore, the method addresses the impact of gear retraction and extension,. These factors are meticulously considered to provide a comprehensive understanding of the landing gear's influence on the aircraft's performance.

$$C_{D_{\text{gear}}} = \text{SUM}_i \left[ \left\{ (C_{D_{\text{gear } C_L=0}})_i + p_i C_L \right\} (S_{\text{gear}})_i / S \right] \quad (3.10)$$

### 3.3.7 Canopy/Windshield Drag Coefficient Prediction

The drag coefficient attributable to the canopy is determined by considering its incremental drag coefficient and its maximum frontal area. The incremental drag coefficient of the canopy can vary based on several factors, including the canopy's shape and the aircraft's angle of attack. In a similar manner, the drag coefficient associated with the windshield is calculated by taking into account the windshield's incremental drag coefficient and its frontal area. The incremental drag coefficient of the windshield is influenced by its specific design characteristics, such as shape and curvature. By meticulously accounting for the individual drag contributions of the canopy and windshield, we can achieve a comprehensive understanding of the overall drag coefficient associated with these crucial aircraft components.

$$C_{D_{cw}} = C_{D_{can}} + C_{D_{ws}} \quad (3.11)$$

### **3.3.8 Store Drag Coefficient Prediction**

This process entails a multi-step approach to accurately estimate the contribution of these external elements to the aircraft's drag. The initial step involves determining the isolated drag coefficient of each individual store, treating it as an independent fuselage-like component. This isolated drag coefficient serves as the baseline for further calculations. Subsequently, the interference factor between the store and the aircraft must be considered. This factor accounts for the complex aerodynamic interactions between the store and the adjacent aircraft components, which can significantly influence the overall drag. By integrating the isolated store drag coefficient with the corresponding interference factor, the total store drag coefficient can be accurately determined. This comprehensive approach ensures that the intricate aerodynamic interactions between the aircraft and the external stores are thoroughly captured, resulting in a more precise representation of the overall drag characteristics. This systematic methodology enables us to accurately predict the drag contributions of various external store configurations.

## **3.4 Prediction of Lift Coefficient versus Angle of Attack**

In this comprehensive section, we explore the methods for predicting the lift coefficient as a function of the angle of attack for various aircraft components, including airfoils, wings, and the entire airplane. This understanding is essential for the design and optimization of aircraft performance. We begin by examining the lift and maximum lift characteristics of an airfoil with the flaps retracted. Key parameters necessary to construct the airfoil's lift coefficient versus angle of attack curve include the zero-lift angle of attack, the lift curve slope, the linear range of the angle of attack, and the angle of attack for maximum lift. These parameters can be estimated using either empirical data or analytical methods, contingent on the availability of specific airfoil information. Next, we shift our focus to the airfoil's lift and maximum lift characteristics with the flaps deployed. The lift coefficient increment due to the deployment of various flap types, such as plain flaps, single-slotted flaps, Fowler flaps, and double-slotted flaps, is calculated and incorporated into the analysis. We then explore the wing's lift and maximum lift characteristics with the flaps retracted. The wing's lift curve slope and maximum lift coefficient are determined based on the airfoil data and the wing's geometric properties, such as aspect ratio and sweep angle. Continuing our examination, we investigate the wing's lift and maximum lift characteristics with the flaps deployed. The wing's lift increment due to the deployment of flaps is calculated, and the resulting flaps-down lift curve

slope and maximum lift coefficient are determined. Lastly, we consider the overall airplane's lift and maximum lift characteristics with the flaps retracted. The airplane's zero-lift angle of attack, lift curve slope, and maximum lift coefficient are calculated using a combination of the wing-fuselage data and the effects of other lifting surfaces, such as the horizontal tail and canard (if present). Finally, we explore the airplane's lift and maximum lift characteristics with the flaps deployed. The airplane's lift increment due to the deployment of flaps is calculated, considering the contributions from the wing, horizontal tail, and canard (if present). The resulting flaps-down lift curve slope and maximum lift coefficient are then determined. By thoroughly examining these methods, we equip ourselves with the necessary tools to accurately predict the lift characteristics of an aircraft. This enables us to optimize the design and ensure the desired performance is achieved.

### **3.5 Prediction of pitching moment Coefficient versus lift Coefficient**

The section outlines a comprehensive approach to understand and estimate the relationship between the pitching moment coefficient and lift coefficient for various aircraft components, including airfoils, wings, and the entire airplane. This is a crucial analysis for ensuring the stability and control of an aircraft. This subsection discusses the methods to determine the variation of the airfoil pitching moment coefficient with its lift coefficient when the flaps are in the retracted position. Key parameters such as the airfoil's zero-lift pitching moment coefficient, aerodynamic center, and center of pressure are identified, and their estimation techniques are provided. Similarly, this subsection outlines the approach to predict the airfoil pitching moment characteristics when the flaps are deployed. The methods account for the incremental changes in pitching moment due to the presence of trailing edge and leading edge flaps. The focus of this subsection is on estimating the wing pitching moment coefficient as a function of its lift coefficient when the flaps are retracted. The analysis considers the wing geometry, including aspect ratio, sweep angle, and taper ratio, as well as the location of the wing's aerodynamic center. Then, we extend the analysis to the scenario where the wing's flaps are deployed. The incremental changes in the wing's pitching moment due to the flaps are quantified using the wing's lift coefficient and geometric parameters. The discussion then shifts to the overall airplane pitching moment characteristics with the flaps retracted. The methodology incorporates the contributions from the wing-fuselage combination, the horizontal tail, and the canard, if present, to determine the airplane's pitching

moment coefficient as a function of its lift coefficient. Finally, the last subsection addresses the case where the airplane's flaps are deployed. The incremental changes in the airplane's pitching moment due to the flaps are calculated, considering the contributions from the wing, canard, and horizontal tail.

## 3.6 Stability Derivatives

### 3.6.1 Speed Derivatives

The speed derivatives in aerodynamic and thrust forces and moments are essential for understanding an aircraft's behavior. These derivatives describe the impact of changes in the aircraft's speed on the various forces and moments acting upon it. The aerodynamic speed derivatives include the drag-due-to-speed derivative  $C_{D_u}$ , the lift-due-to-speed derivative  $C_{L_u}$ , and the pitching-moment-due-to-speed derivative  $C_{m_u}$ , as shown in Equations (3.12), (3.13), and (3.14). These derivatives quantify how the drag, lift, and pitching moment of the aircraft vary with changes in speed, respectively. Collectively, these speed derivatives offer a comprehensive understanding of how the aircraft's aerodynamic and propulsive characteristics respond to changes in flight speed. This knowledge is crucial for designing and analyzing the aircraft's stability and control properties.

$$C_{D_u} = M_1 (\partial C_D / \partial M) \quad (3.12)$$

$$C_{L_u} = \left( M_1^2 (\cos \Lambda_{c/4})^2 C_{L_1} \right) / \left( 1 - M_1^2 (\cos \Lambda_{c/4})^2 \right) \quad (3.13)$$

$$C_{m_u} = -C_{L_1} (\partial \bar{x}_{acA} / \partial M) \quad (3.14)$$

### 3.6.2 Angle of Attack Derivatives

The angle of attack derivatives describe how the aerodynamic and thrust forces and moments vary with changes in the aircraft's angle of attack. These derivatives are essential for understanding the aircraft's stability and control characteristics. The aerodynamic angle of attack derivatives include the drag-due-to-angle-of-attack derivative  $C_{D_\alpha}$ , the lift-due-to-angle-of-attack derivative  $C_{L_\alpha}$ , and the pitching-moment-due-to-angle-of-attack derivative  $C_{m_\alpha}$ . These derivatives capture the sensitivity of drag, lift, and pitching moment to changes in the aircraft's angle of attack. Additionally, the thrust-versus-angle-of-attack derivative  $C_{m_{\alpha_T}}$  describes how the pitching moment due to thrust varies with the angle of

attack. This derivative is crucial for understanding the interplay between the aircraft's aerodynamic characteristics and its propulsion system. Collectively, these angle of attack derivatives provide a comprehensive understanding of how the aircraft's forces and moments respond to changes in the angle of attack. This knowledge is vital for designing and analyzing the aircraft's stability, control, and handling qualities.

$$C_{D\alpha} = (\partial C_D / \partial C_L) C_{L\alpha} \quad (3.15)$$

$$C_{L\alpha} = (dC_m / dC_{L\alpha}) \quad (3.16)$$

$$C_{m\alpha} = (dC_m / dC_L) C_{L\alpha} \quad (3.17)$$

### 3.6.3 Rate of Angle of Attack Derivatives

The rate of angle of attack derivatives describe how the aircraft's aerodynamic forces and moments change with the rate of change in the angle of attack. These derivatives provide insights into the aircraft's dynamic behavior and are crucial for analyzing its stability and control characteristics. The key rate of angle of attack derivatives include the drag-due-to-rate-of-angle-of-attack derivative  $C_{D\dot{\alpha}}$ , the lift-due-to-rate-of-angle-of-attack derivative  $C_{L\dot{\alpha}}$ , and the pitching-moment-due-to-rate-of-angle-of-attack derivative  $C_{m\dot{\alpha}}$ . The drag-due-to-rate-of-angle-of-attack derivative  $C_{D\dot{\alpha}}$  is typically considered negligible and often disregarded in the analysis. On the other hand, the lift-due-to-rate-of-angle-of-attack derivative  $C_{L\dot{\alpha}}$  and the pitching-moment-due-to-rate-of-angle-of-attack derivative  $C_{m\dot{\alpha}}$  can have significant impacts on the aircraft's dynamic behavior, particularly in the longitudinal stability and control. These rate of angle of attack derivatives provide a deeper understanding of how the aircraft's aerodynamic characteristics respond to changes in the rate of the angle of attack. This knowledge is essential for designing and analyzing the aircraft's handling qualities and overall dynamic stability.

$$C_{D\dot{\alpha}} = 0 \quad (3.18)$$

$$C_{L\dot{\alpha}} = 2C_{L\alpha_h} \eta_h \bar{v}_h (d\delta / d\alpha) \quad (3.19)$$

$$C_{m\dot{\alpha}} = -2C_{L\alpha_h} \eta_h \bar{v}_h (\bar{x}_{ac_h} - \bar{x}_{cg}) (d\delta / d\alpha) \quad (3.20)$$

### 3.6.4 Angle of Sideslip Derivatives

The angle of sideslip derivatives describe how an aircraft's aerodynamic forces and moments react to changes in its sideslip angle. These derivatives are essential for understanding an aircraft's lateral-directional stability and control characteristics. The primary angle of sideslip derivatives include the sideforce-due-to-sideslip derivative  $C_{Y_\beta}$ , the rolling-moment-due-to-sideslip derivative  $C_{l_\beta}$ , and the yawing-moment-due-to-sideslip derivative  $C_{n_\beta}$ . These derivatives quantify the sensitivity of the sideforce, rolling moment, and yawing moment to variations in the sideslip angle, respectively. The sideforce-due-to-sideslip derivative  $C_{Y_\beta}$  is influenced by contributions from the wing, fuselage, and vertical tail(s). The rolling-moment-due-to-sideslip derivative  $C_{l_\beta}$ , commonly referred to as the dihedral effect, is affected by the characteristics of the wing-fuselage combination, horizontal tail, and vertical tail. The yawing-moment-due-to-sideslip derivative  $C_{n_\beta}$ , which represents static directional stability, is predominantly influenced by the fuselage and vertical tail(s). Additionally, the thrust-versus-sideslip derivative  $C_{n_{\beta_T}}$  describes the effect of thrust on the yawing moment due to sideslip. This derivative is crucial for understanding the propulsive contributions to the aircraft's lateral-directional stability. These angle of sideslip derivatives offer a comprehensive understanding of how an aircraft's lateral-directional characteristics respond to changes in the sideslip angle.

$$C_{y_\beta} = C_{y_{\beta_w}} + C_{y_{\beta_f}} + C_{y_{\beta_v}} \quad (3.21)$$

$$C_{l_\beta} = C_{l_{\beta_{wf}}} + C_{l_{\beta_h}} + C_{l_{\beta_v}} \quad (3.22)$$

$$C_{n_\beta} = C_{n_{\beta_w}} + C_{n_{\beta_f}} + C_{n_{\beta_v}} \quad (3.23)$$

### 3.6.5 Rate of Angle of Sideslip Derivatives

The rate of angle of sideslip derivatives provide crucial insights into the aircraft's dynamic behavior and are essential for analyzing its lateral-directional stability and control characteristics. The primary rate of angle of sideslip derivatives include the sideforce-due-to-rate-of-sideslip derivative  $C_{Y_{\dot{\beta}}}$ , the rolling-moment-due-to-rate-of-sideslip derivative  $C_{l_{\dot{\beta}}}$ , and the yawing-moment-due-to-rate-of-sideslip derivative  $C_{n_{\dot{\beta}}}$ . The sideforce-due-to-rate-of-sideslip derivative  $C_{Y_{\dot{\beta}}}$  captures the sensitivity of the sideforce to changes in the rate of sideslip. The rolling-moment-due-to-rate-of-sideslip derivative  $C_{l_{\dot{\beta}}}$  describes how the rolling moment varies with the rate of change in sideslip. The

yawing-moment-due-to-rate-of-sideslip derivative  $C_{n_{\dot{\beta}}}$  represents the aircraft's responsiveness in yaw to changes in the rate of sideslip. These rate of angle of sideslip derivatives provide a deeper understanding of how an aircraft's lateral-directional characteristics respond to dynamic changes in the sideslip angle.

$$C_{Y_{\dot{\beta}}} = 2(C_{L_{a_v}})(d\sigma/d\beta)(S_v/S)(1_p \cos a_f + z_p \sin a_f)/b \quad (3.24)$$

$$C_{l_{\dot{\beta}}} = C_{Y_{\dot{\beta}}}(z_p \cos \alpha_f - 1_p \sin \alpha_f)/b \quad (3.25)$$

$$C_{n_{\dot{\beta}}} = C_{Y_{\dot{\beta}}}(1_p \cos a_f + z_p \sin a_f)/b \quad (3.26)$$

### 3.6.6 Roll Rate Derivatives

The roll rate derivatives are crucial for understanding the aircraft's lateral-directional dynamic stability and control characteristics. The primary roll rate derivative of interest is the rolling-moment-due-to-roll-rate derivative  $C_{l_p}$ . This derivative measures the sensitivity of the rolling moment to changes in the aircraft's roll rate. The rolling-moment-due-to-roll-rate derivative  $C_{l_p}$  is influenced by contributions from the wing, fuselage, and horizontal tail. The wing's contribution is primarily dependent on its geometric dihedral and aspect ratio, while the fuselage and horizontal tail also have significant effects. This roll rate derivative provides insights into the aircraft's roll damping, which is a crucial factor in determining lateral-directional stability and the pilot's ability to control the roll motion. A higher positive value of  $C_{l_p}$  indicates stronger roll damping, which is generally desirable for stability and control. By understanding the roll rate derivative, aircraft designers and analysts can evaluate the aircraft's roll characteristics and make informed decisions to ensure the desired handling qualities and dynamic behavior.

$$C_{Y_p} = 2(C_{Y_{\beta_v}})(z_v \cos \alpha - 1_v \sin \alpha)/b \quad (3.27)$$

$$C_{l_p} = C_{l_{p_w}} + C_{l_{p_h}} + C_{l_{p_v}} \quad (3.28)$$

$$C_{n_p} = C_{n_{p_w}} + C_{n_{p_v}} \quad (3.29)$$

### 3.6.7 Pitch Rate Derivatives

The pitch rate derivatives describe how the aircraft's aerodynamic forces and moments vary with changes in the aircraft's pitch rate. These derivatives play a crucial role in understanding the aircraft's longitudinal dynamic stability and control characteristics. The key pitch rate derivative is the pitching-moment-due-to-pitch-rate derivative  $C_{m_q}$ . This derivative captures the sensitivity of the pitching moment to changes in the aircraft's pitch rate. The pitching-moment-due-to-pitch-rate derivative  $C_{m_q}$  is primarily influenced by the contributions from the horizontal tail. The horizontal tail's effectiveness in generating a stabilizing pitching moment in response to pitch rate changes is a crucial factor in this derivative. This pitch rate derivative provides insights into the aircraft's pitch damping, which is an important factor in determining the aircraft's longitudinal stability and the pilot's ability to control the aircraft's pitch motion. A higher negative value of  $C_{m_q}$  indicates stronger pitch damping, which is generally desirable for aircraft stability and control. By understanding the pitch rate derivative, aircraft designers and analysts can evaluate the aircraft's pitch characteristics and make informed decisions to ensure the desired handling qualities and dynamic behavior.

$$C_{D_q} = 0 \quad (3.30)$$

$$C_{L_q} = C_{L_{q_w}} + C_{L_{q_h}} + C_{L_{q_c}} \quad (3.31)$$

$$C_{m_q} = C_{m_{q_w}} + C_{m_{q_h}} + C_{m_{q_c}} \quad (3.32)$$

### 3.6.8 Yaw Rate Derivatives

The yaw rate derivatives describe how the aircraft's aerodynamic forces and moments respond to changes in the aircraft's yaw rate. These derivatives are crucial in understanding the aircraft's lateral-directional dynamic stability and control characteristics. The primary yaw rate derivative of interest is the yawing-moment-due-to-yaw-rate derivative  $C_{n_r}$ . This derivative captures the sensitivity of the yawing moment to changes in the aircraft's yaw rate. The yawing-moment-due-to-yaw-rate derivative  $C_{n_r}$  is influenced by the contributions from the vertical tail(s), wing, and fuselage. The vertical tail's effectiveness in generating a stabilizing yawing moment in response to yaw rate changes is a key factor in this derivative. This yaw rate derivative provides insights into the aircraft's yaw damping, which is an important factor in determining the aircraft's lateral-directional stability and the pilot's ability to control the

aircraft's yaw motion. A higher negative value of  $C_{n_r}$  indicates stronger yaw damping, which is generally desirable for aircraft stability and control.

$$C_{Y_r} = -2(C_{Y_{\beta_v}})(1_v \cos \alpha + z_v \sin \alpha)/b \quad (3.33)$$

$$C_{l_r} = C_{l_{r_w}} + C_{l_{r_v}} \quad (3.34)$$

$$C_{n_r} = C_{n_{r_w}} + C_{n_{r_v}} \quad (3.35)$$

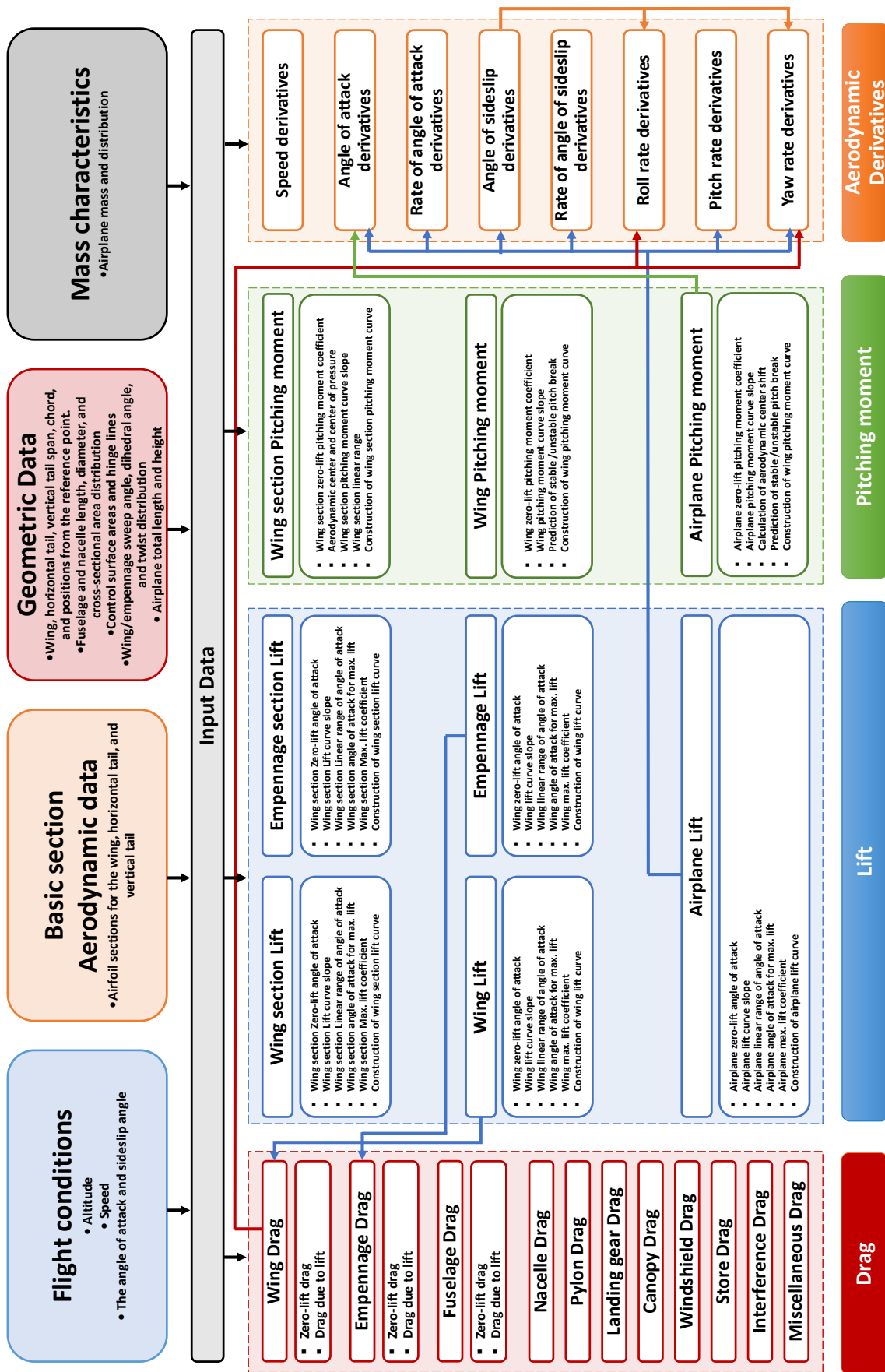


Fig. (3.1) Evaluating aeromechanical characteristics Flowchart

## **Chapter 4**

### **Verification and Validation of the AeroMech tool**

#### **4.1 Comparison of Aerodynamic Characteristics of Cessna-182 and Cessna-310**

This study is dedicated to a comparative analysis of the aerodynamic properties of two aircraft models: the Cessna-182 and the Cessna-310. The aerodynamic data of these aircraft are calculated using the AeroMech tool and are subsequently compared with published data as well as results from two popular aerodynamic analysis software programs: Digital DATCOM and XFLR5. The choice of these specific aircraft models is based on several criteria that ensure the relevance and clarity of the comparison for both the academic community and the broader field of aeronautics.

##### **4.1.1 Selection Criteria**

The selection of the Cessna-182 and the Cessna-310 for this comparative study was guided by the following considerations:

- **Familiarity and Popularity:** The Cessna-182 and Cessna-310 are well-known and widely utilized aircraft models. This familiarity aids in grounding our study within a context that is easily relatable and comprehensible to many readers, facilitating a more straightforward comparison with existing research findings.
- **Design and Performance Variations:** These aircraft exemplify distinct design philosophies and performance characteristics. The Cessna-182 is a single-engine aircraft with a high-wing configuration, primarily serving general aviation purposes. In contrast, the Cessna-310 is a twin-engine aircraft featuring a low-wing design, commonly used for light business and commercial aviation. By juxtaposing these two diverse aircraft types, the study aims to offer a comprehensive understanding of the factors influencing aircraft performance and to verify the accuracy of the AeroMech tool. Additionally, this comparison seeks to identify any discrepancies in performance outcomes when juxtaposed with prior research.

### 4.1.2 Aircraft Overview

The Cessna-182, depicted in Figure 4.1, is a high-wing, single-engine light aircraft designed with general aviation in mind. Its design and operational characteristics make it an ideal candidate for personal use and pilot training.

Conversely, the Cessna-310, shown in Figure 4.2, is a low-wing, twin-engine light aircraft. It is engineered for both general aviation and business travel, offering enhanced performance and reliability for commercial applications.

Table 4.1 summarizes the key specifications of these two aircraft models, providing a reference point for the detailed aerodynamic analyses that follow.



Fig. (4.1) Cessna-182 airplane.



Fig. (4.2) Cessna-310 airplane.

Table (4.1) Specifications of the two case-study airplanes

Parameter	Value		Unit
	Cessna-182	Cessna-310	
Maximum takeoff weight	1406	2087	kg
Empty weight	894	1523	kg
Wingspan	10.97	11.25	m
Total length	8.84	9.74	m
Height	2.84	3.25	m
Wing area	16.2	16.6	m <sup>2</sup>
Cruise speed	269	330	km/h
Max power	230	285	hp
No. of engines	1	2	-
Powerplant	Lycoming IO-540-AB1A5	Continental IO-520-MB	-

This comparison provides a valuable opportunity to explore the factors that influence airplane performance and gain a deeper understanding of the subject matter.

## **4.2 Verification and Validation of AeroMech Tool**

In order to ascertain the accuracy of the aerodynamic characteristics predicted by the AeroMech tool, it is essential to perform a comparative analysis with the results derived from two well-regarded aerodynamic analysis software programs: Digital DATCOM and XFLR5. This comparison is carried out for two distinct case studies, thereby providing a robust assessment of the AeroMech tool's predictive capabilities.

The primary objective of this comparison is to establish the reliability of the AeroMech tool in accurately predicting the aerodynamic properties of aircraft. By juxtaposing the results obtained from the AeroMech tool with those from Digital DATCOM and XFLR5, we can identify any potential discrepancies and evaluate the consistency of the AeroMech tool's outputs.

Subsequent to this comparative analysis, the results produced by the AeroMech tool are further validated against published data. This additional validation step is crucial as it enhances the level of confidence in the precision and reliability of the AeroMech tool. By aligning the AeroMech tool's predictions with established published data, we can substantiate its accuracy and robustness in aerodynamic analysis.

This rigorous verification process is instrumental in confirming the AeroMech tool's efficacy and ensuring its suitability for comprehensive aerodynamic evaluations. It not only reinforces the credibility of the AeroMech tool but also underscores its potential as a reliable instrument for future aerodynamic studies.

### ***4.2.1 Digital DATCOM: A Computer Program for Aerodynamic Estimation***

Digital DATCOM is a sophisticated computer program designed to estimate the aerodynamic, stability, and control characteristics of an aircraft in a systematic manner. This tool is pivotal during the preliminary design phase, where designers necessitate rapid and cost-effective estimations of these characteristics. The preliminary design phase demands swift estimates, and while intricate automated procedures can be highly accurate, they are often time-consuming and computationally expensive. Conversely, manual calculation methods, although sometimes necessary, are inefficient due to the substantial man-hours required,

particularly when conducting configuration trade studies or evaluating a range of flight conditions.

The foundation of the Digital DATCOM program lies in the philosophy of the USAF Stability and Control Datcom. This philosophy emphasizes providing a structured summary of methods for estimating stability and control characteristics, tailored specifically for preliminary design applications. The program employs a modular approach, with each module specializing in the estimation of different aerodynamic characteristics. These modules encompass lift, drag, pitching moment, rolling moment, yawing moment, and control derivatives. Additionally, the program includes modules to estimate static stability derivatives, which are crucial for describing the aircraft's tendency to return to its trimmed condition following a disturbance.

To utilize Digital DATCOM, designers input detailed aircraft geometry, which includes parameters such as wing planform, fuselage geometry, and control surface deflections. The program then processes this input to calculate the corresponding aerodynamic derivatives. These derivatives are essential inputs for the stability and control analysis of the aircraft. It is important to note that the accuracy of the Digital DATCOM program is contingent upon the precision of the input geometry and the inherent limitations of the program itself.

Figures 4.3 and 4.4 provide visual representations of the Cessna-182 and Cessna-310 case studies utilized in this research, respectively. These illustrations underscore the practical application of Digital DATCOM in estimating the aerodynamic characteristics of these aircraft models.

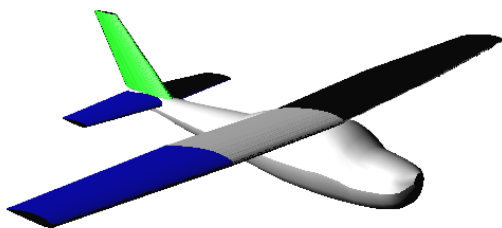


Fig. (4.3) Cessna-182 3D-model in Digital DATCOM.

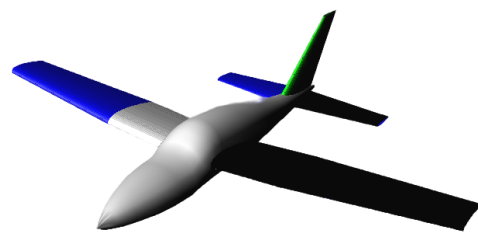


Fig. (4.4) Cessna-310 3D-model in Digital DATCOM.

#### ***4.2.2 XFLR5: A Computer Program for Aerodynamic Analysis***

XFLR5 is a prominent computational tool extensively utilized for analyzing and determining the aerodynamic characteristics of aircraft. This program is grounded in potential

flow theory, which assumes that the airflow around an aircraft is predictable, irrotational, inviscid, and incompressible. By employing numerical methods to solve the equations governing airflow around an aircraft, XFLR5 can generate comprehensive data on various performance metrics such as lift and drag coefficients, pitching moments, and pressure distributions.

The reliability of XFLR5 has been established through rigorous validation against experimental data and comparison with other numerical methods. It has gained widespread acceptance in the field of aircraft design and analysis, and its efficacy is reflected in numerous research studies and scientific publications. To utilize XFLR5 for calculating the aerodynamic characteristics of an aircraft, the user begins by creating a detailed 3D model of the aircraft, incorporating physical attributes such as wingspan, wing area, and airfoil sections. XFLR5 includes an extensive built-in airfoil database and allows for the importation of custom airfoil data. Following the setup of the aircraft model, the user can simulate various flight conditions, including different angles of attack, velocities, and altitudes.

The core computational mechanism of XFLR5 involves solving potential flow equations using a panel method. This technique entails dividing the aircraft's surface into numerous small flat panels and calculating the velocity and pressure at each panel. These computed values are then used to determine the lift, drag, and pitching moment coefficients of the aircraft. Additionally, XFLR5 offers graphical outputs such as pressure distributions over the aircraft surface and airflow streamlines, providing visual insights into the aerodynamic behavior.

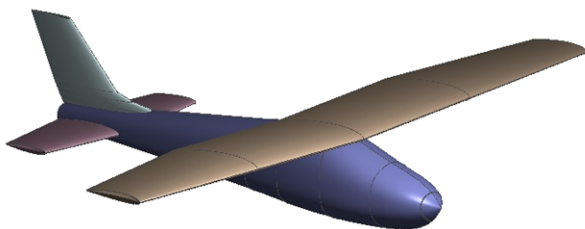


Fig. (4.5) Cessna-182 3D-model  
in XFLR5.

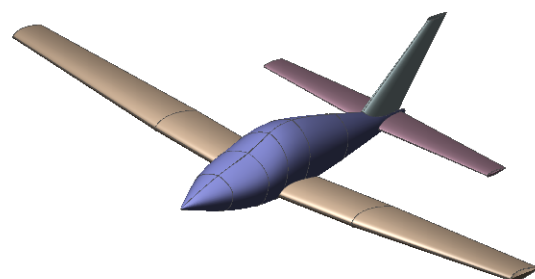


Fig. (4.6) Cessna-310 3D-model  
in XFLR5.

The initial step in employing XFLR5 for aerodynamic analysis of a case-study aircraft

involves the creation of a three-dimensional digital model of the aircraft's geometry. This is typically accomplished using computer-aided design (CAD) software to construct a solid model of the aircraft's components, including the fuselage, wings, tail, and other relevant parts. The digital model is subsequently imported into XFLR5 for analysis. The next phase involves discretizing the aircraft's geometry into small computational sections, or "panels," which accurately represent the aircraft's surface. The number and size of these panels can be adjusted to achieve a balance between computational accuracy and efficiency.

Once the panels are defined, XFLR5 calculates the aerodynamic forces acting on the aircraft, encompassing lift, drag, and moment, which are critical for assessing the aircraft's performance. The simulation results are then analyzed to derive key aerodynamic characteristics such as the maximum lift coefficient, stall speed, drag polar, and stability derivatives. The drag polar, which plots the drag coefficient as a function of the lift coefficient, is crucial for evaluating the aircraft's performance in terms of range, endurance, and fuel efficiency. Stability derivatives provide insights into the aircraft's longitudinal, lateral, and directional stability, essential for predicting its handling qualities.

Figures 4.5 and 4.6 illustrate the CAD outputs for the Cessna-182 and Cessna-310 case studies, respectively, showcasing the practical application of XFLR5 in aerodynamic analysis.

#### ***4.2.3 Discussion of Results: Comparison with Reference Software and Published Data***

The aerodynamic characteristics of the selected aircraft models were meticulously analyzed using our AeroMech tool, which leverages an analytical-empirical method. To validate the accuracy of our tool, the results were compared with those obtained from two established aerodynamic analysis software programs, Digital DATCOM and XFLR5. The overall comparison revealed a commendable agreement between the AeroMech tool and the reference software, albeit with some logical discrepancies.

These discrepancies can be attributed to multiple factors. Primarily, the analytical-empirical method employed by the AeroMech tool is based on simplified models of aerodynamic phenomena, which may not fully encapsulate the complexities of real-world conditions. In contrast, the reference software uses more sophisticated numerical methods that can better account for the intricate details of the flow field. Additionally, variations in the

underlying assumptions and computational methodologies across the different software tools can lead to differences in the predicted aerodynamic characteristics.

Comparisons with published data also showed generally good agreement, although some differences were noted. These variations can be traced back to differences in computational methodologies, variations in experimental data used for comparison, and inherent limitations in the modeling assumptions of the analytical-empirical approach.

The lift curves for the Cessna-182 and Cessna-310 aircraft, depicted in Figures 4.7 and 4.8, indicate that the lift coefficient values derived from XFLR5 and the AeroMech tool exhibit high similarity. The Digital DATCOM method, while close, shows slight deviations in the slope of the curve. Similarly, the pitching moment curves for both aircraft, shown in Figures 4.9 and 4.10, reveal that the values obtained from the AeroMech tool, Digital DATCOM, and XFLR5 are comparable. The drag curves, illustrated in Figures 4.11 and 4.12, also demonstrate a high degree of similarity among the three approaches, with minimal differences observed.

The analysis of the  $C_{Lq}$  derivatives for both case studies indicates that the AeroMech tool produces values moderately close to the published data. The observed discrepancies can be attributed to variations in flight conditions, geometric data of the aircraft components, propulsion data, and the lift and pitching moment characteristics of the aircraft. Similarly, the  $C_{n\beta}$  derivatives analysis shows that the AeroMech tool's values are reasonably close to the published data. Furthermore, the analysis of the  $C_{yp}$ ,  $C_{np}$ , and  $C_{yr}$  derivatives for both the Cessna-182 and Cessna-310 indicates that the values generated by the AeroMech tool are in moderate agreement with the published data.

In summary, the AeroMech tool has demonstrated its efficacy in assessing the aerodynamic characteristics of aircraft, proving to be a promising approach for predicting these characteristics. Despite some observed differences, the tool offers a rapid and efficient means of generating predictions, making it particularly suitable for early-stage design analysis. Future studies are recommended to further refine the precision of the AeroMech tool, enhancing its reliability and accuracy in predicting aircraft performance.

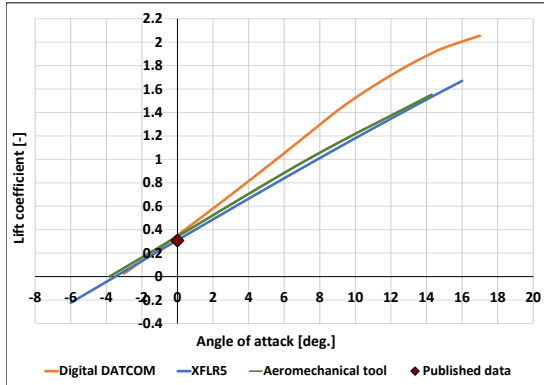


Fig. (4.7) Lift curve for Cessna-182.

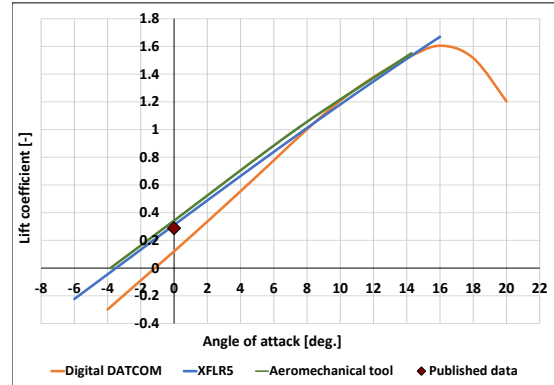


Fig. (4.8) Lift curve for Cessna-310.

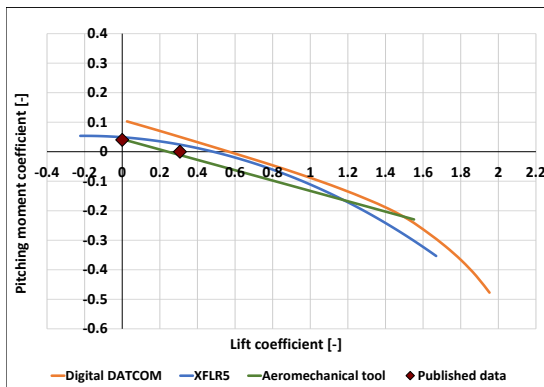


Fig. (4.9) Pitching moment curve for Cessna-182.

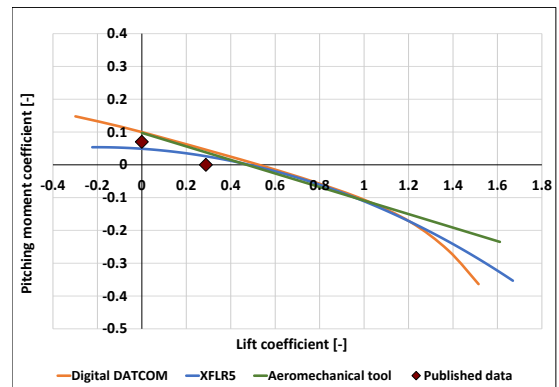


Fig. (4.10) Pitching moment curve for Cessna-310.

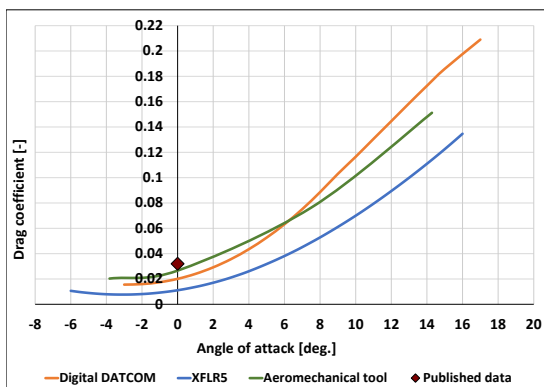


Fig. (4.11) Drag curve for Cessna-182.

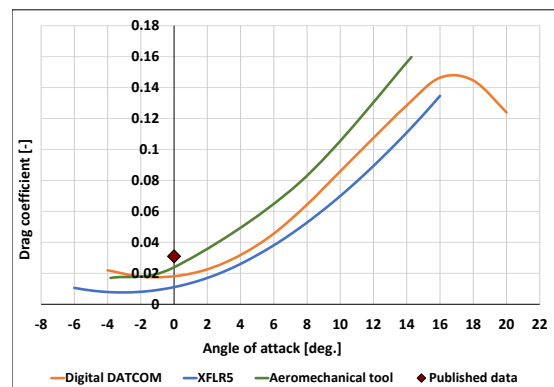


Fig. (4.12) Drag curve for Cessna-310.

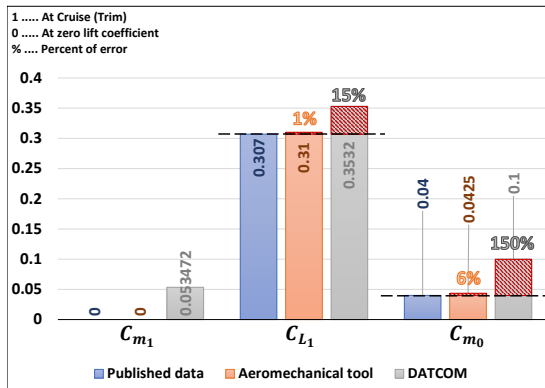


Fig. (4.13) Aerodynamic coefficients for Cessna-182

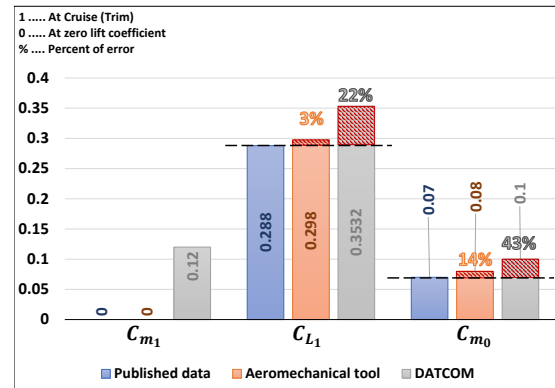


Fig. (4.14) Aerodynamic coefficients for Cessna-310.

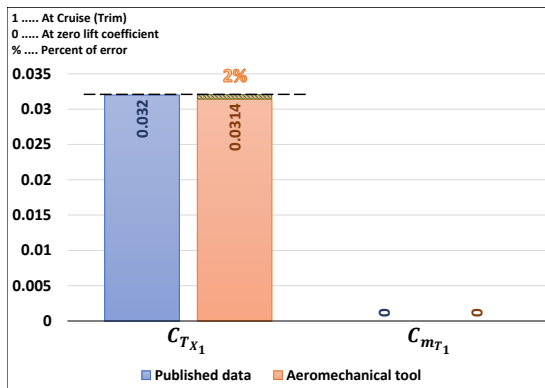


Fig. (4.15) Steady-state derivatives for Cessna-182.

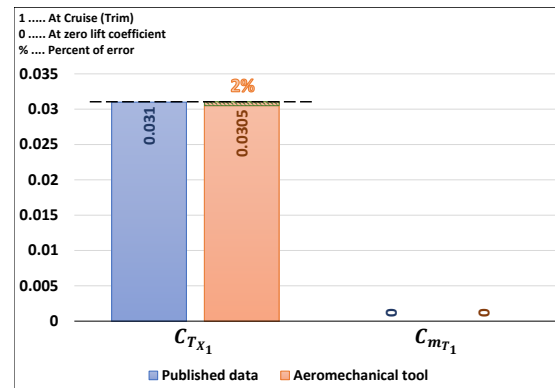


Fig. (4.16) Steady-state derivatives for Cessna-310.

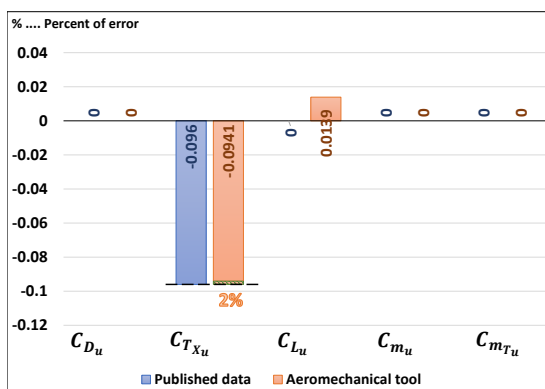


Fig. (4.17) Speed derivatives for Cessna-182.

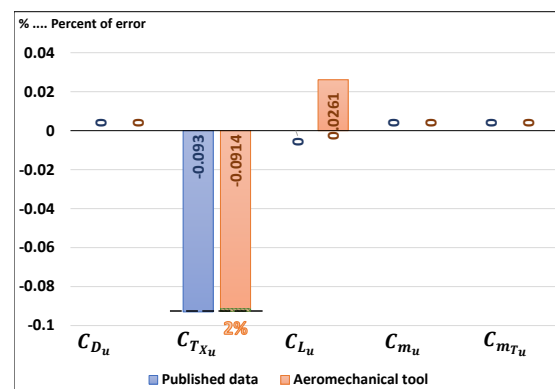


Fig. (4.18) Speed derivatives for Cessna-310.

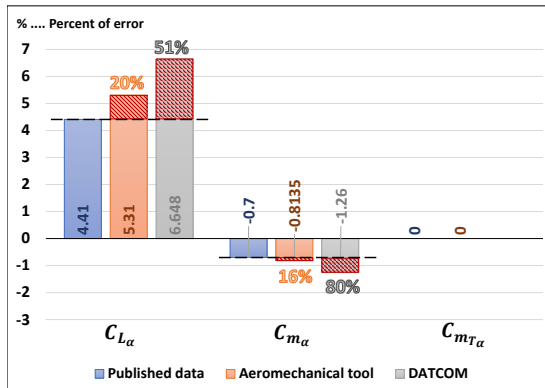


Fig. (4.19) Angle of attack derivatives for Cessna-182.

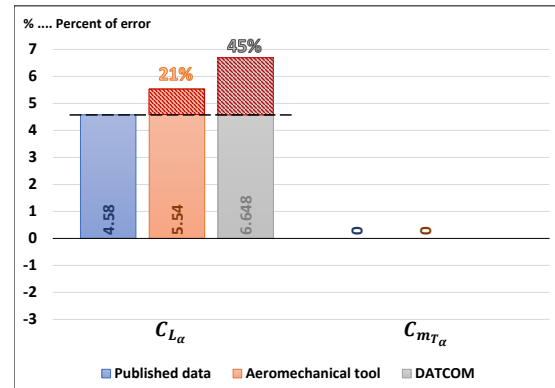


Fig. (4.20) Angle of attack derivatives for Cessna-310.

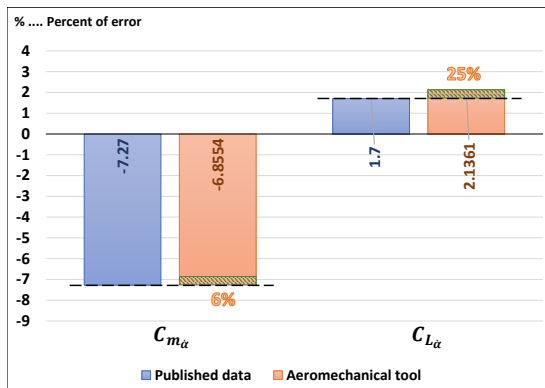


Fig. (4.21) Rate of angle of attack derivatives for Cessna-182.

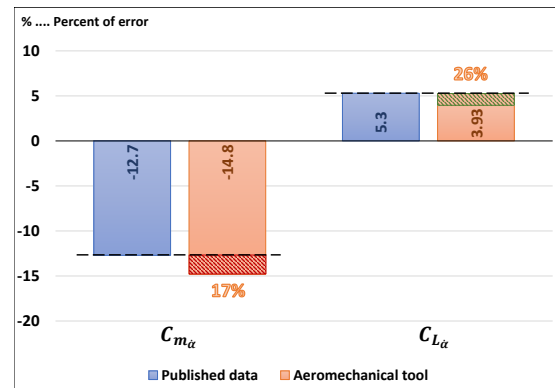


Fig. (4.22) Rate of angle of attack derivatives for Cessna-310.

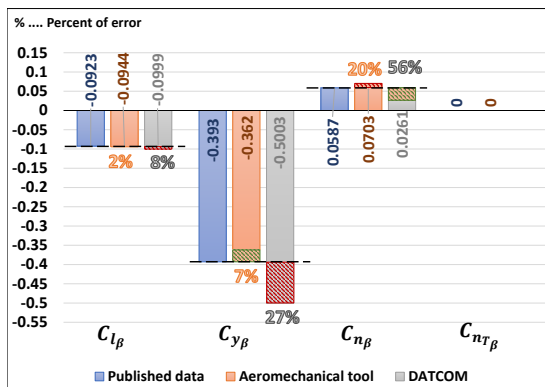


Fig. (4.23) Sideslip angle derivatives for Cessna-182.

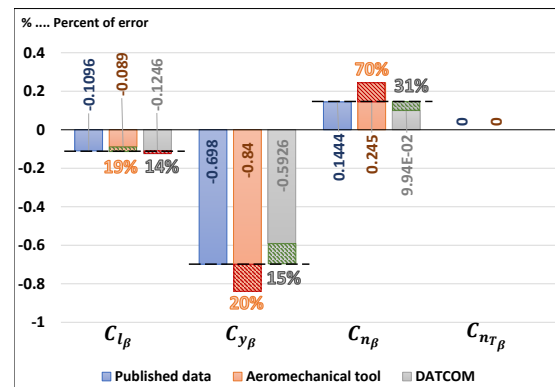


Fig. (4.24) Sideslip angle derivatives for Cessna-310.

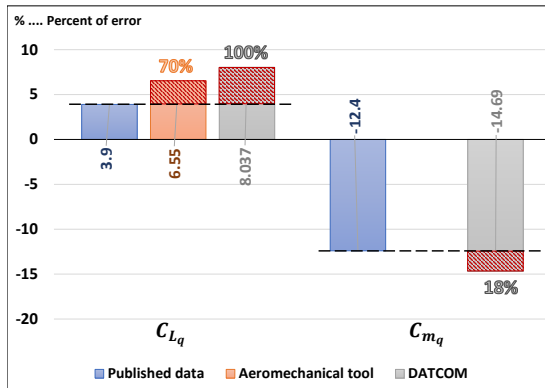


Fig. (4.25) Pitch rate derivatives for Cessna-182.

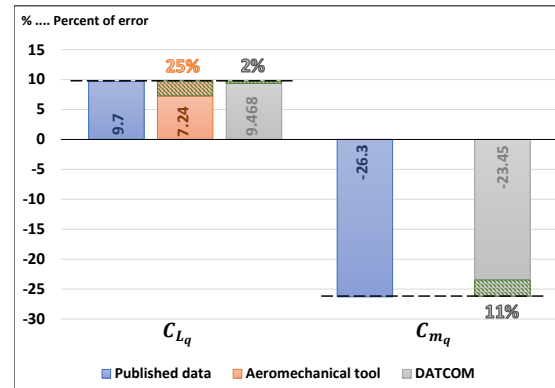


Fig. (4.26) Pitch rate derivatives for Cessna-310.

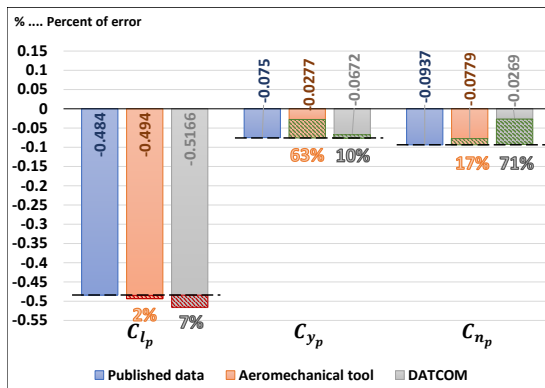


Fig. (4.27) Roll rate derivatives for Cessna-182.

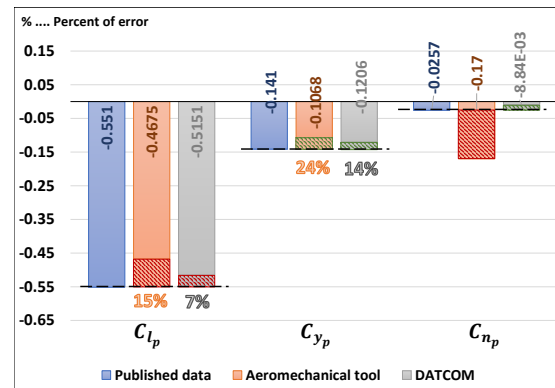


Fig. (4.28) Roll rate derivatives for Cessna-310.

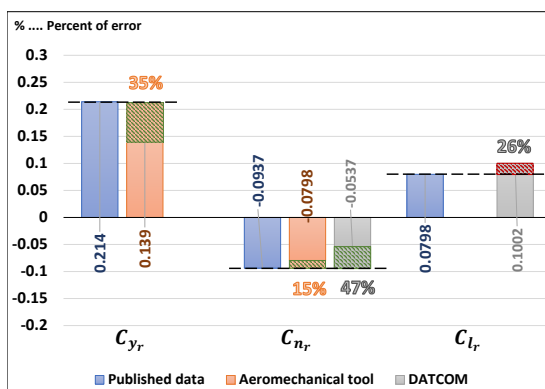


Fig. (4.29) Yaw rate derivatives for Cessna-182.

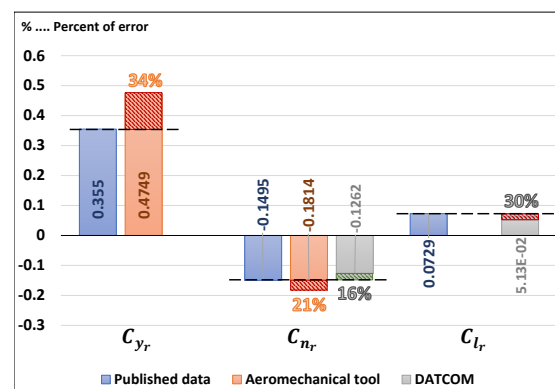


Fig. (4.30) Yaw rate derivatives for Cessna-310.

## **Chapter 5**

### **Computational and Experimental Techniques to Evaluate the Aerodynamic Derivatives of the Wing Loong I UAV**

#### **5.1 Application of AeroMech Tool for Wing Loong I**

The efficacy of the AeroMech tool in predicting aircraft aerodynamics has already been validated and verified through comprehensive case studies [?]. Building upon this solid foundation, our current focus shifts to calculating the aerodynamic derivatives for the Unmanned Aerial Vehicle (UAV) known as Wing Loong I. To ensure the precision and reliability of AeroMech's outputs, we have compared these results with those generated by the Digital DATCOM and XFLR5 programs.

Digital DATCOM is renowned for its efficiency in preliminary aerodynamic design, offering a rapid and cost-effective method for estimating the aerodynamic characteristics, stability, and control of aircraft. It is grounded in the principles of the USAF Stability and Control Datcom [?, 5] and employs a modular approach to systematically calculate various aerodynamic properties and static stability derivatives [?, ?].

Contrarily, XFLR5 is celebrated for its robust capabilities in aerodynamic analysis, relying on potential flow theory to compute essential aerodynamic coefficients such as lift and drag [?, ?]. The program allows users to create detailed 3D models, simulate diverse flight conditions, and analyze aerodynamic forces, thereby providing a comprehensive understanding of critical aircraft characteristics, including lift, drag, and pitching moment curves.

The results demonstrated in Lift Curve, pitching moment curve, Drag Curve, Polar Curve, Angle of Attack Derivatives, SideSlip Angle Derivatives, Roll Derivatives, Yaw Derivatives showcase a comparison between the outputs of the AeroMech tool, Digital DATCOM, and XFLR5. These results exhibit a notable convergence, underscoring the reliability and accuracy of the AeroMech tool in predicting the aerodynamic performance of the Wing Loong I UAV.

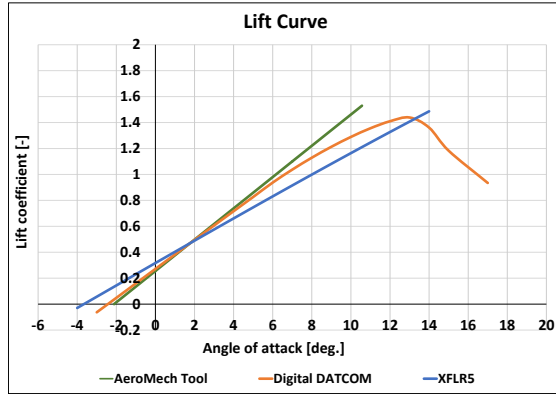


Fig. (5.1) Lift Curve

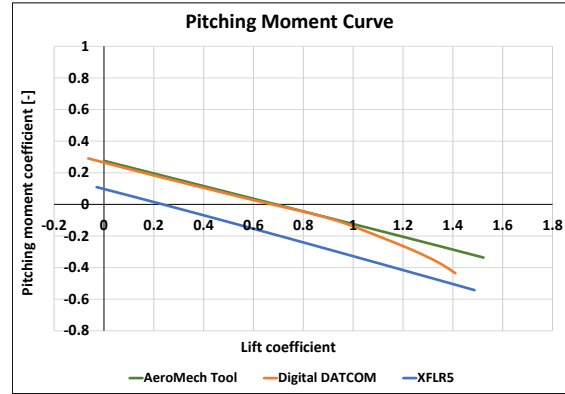


Fig. (5.2) pitching moment curve

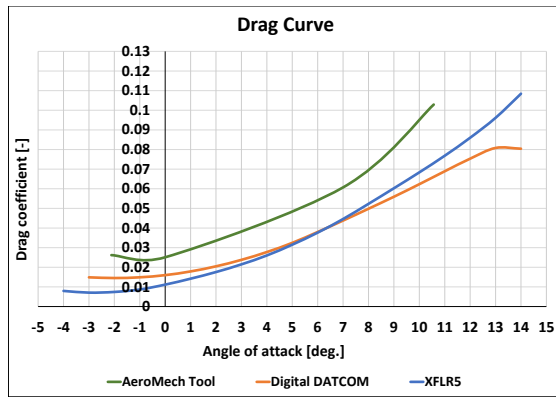


Fig. (5.3) Drag Curve

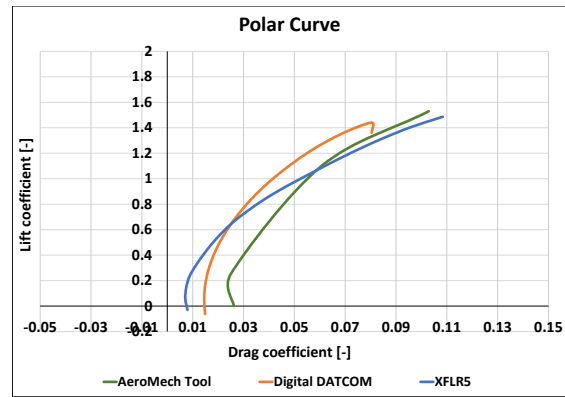


Fig. (5.4) Polar Curve

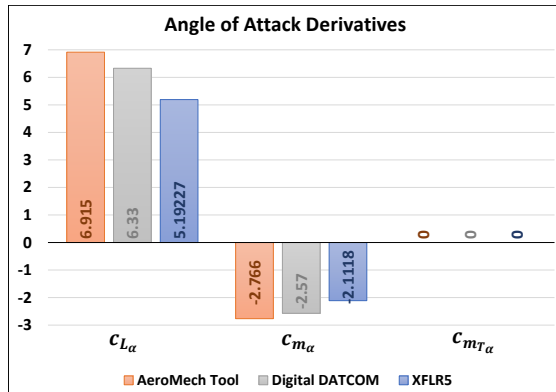


Fig. (5.5) Angle of Attack Derivatives

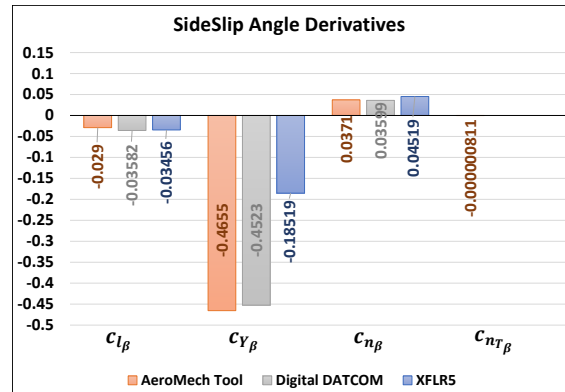


Fig. (5.6) SideSlip Angle Derivatives

## 5.2 Design and Manufacturing of the Wing Loong I Model Using 3D Printing

Traditionally, wind tunnel test models for aircraft design have been produced using conventional machining techniques, such as CNC machining of metals [65]. However, the high

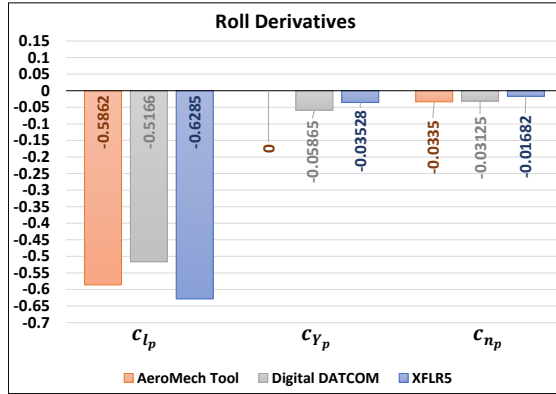


Fig. (5.7) Roll Derivatives

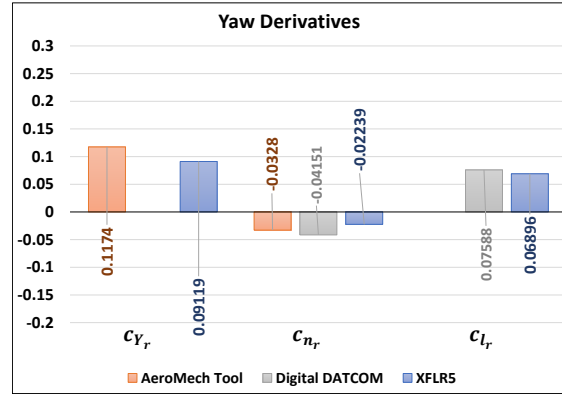


Fig. (5.8) Yaw Derivatives

costs and lengthy transition times from CAD to physical prototypes have hindered the concept of "rapid" prototyping. The emergence of three-dimensional (3D) printing technology offers a promising solution to these challenges [66–68].

Numerous researchers have explored the application of 3D printed aircraft models in wind tunnel testing. Studies have reported the comparative evaluation of 3D printed models and their performance, demonstrating the viability of this approach [66–68]. The literature also discusses the development of accurate and robust approximation methodologies for experimentally derived results, well-suited for industrial problems [69, 70].

The advantages of 3D printing in the aerospace industry are significant. It enables the creation of complex geometries and shapes, reduces cycle times and production costs, and decreases part weights compared to conventional manufacturing techniques [?, 71–73]. The shift from rapid prototyping to rapid manufacturing, facilitated by additive manufacturing (AM) and 3D printing, presents new opportunities and challenges for mechanical engineers and material scientists [72].

One of the most notable advantages of 3D printing is the ability to produce individual elements at a relatively low cost without the need to run the entire production line. This capability enables the verification of product appearance and parameter validation before full-scale manufacturing [72]. Additionally, the flexibility of 3D printing allows for iterative design improvements based on the manufacturer's preferences.

Building on the validated and verified AeroMech tool, we can now use this tool to calculate the aerodynamic derivatives for the Wing Loong I UAV. By leveraging 3D printing

technology, we can rapidly produce accurate physical models of the Wing Loong I UAV. These models can then be utilized in wind tunnel testing to validate the aerodynamic derivatives predicted by the AeroMech tool. This approach not only confirms the tool's predictions but also provides valuable insights for further refinement and optimization of the UAV's design.

### ***5.2.1 Material Selection and Model Fabrication for Aerodynamic Research***

To advance aerodynamic research for the Wing Loong I UAV, Polylactic Acid (PLA) was selected as the material for constructing the aircraft model. A critical component of this research involved creating a precise 3D scan of the aircraft model to facilitate controlled laboratory experiments. The process comprised several key steps aimed at ensuring the accuracy and efficacy of the model for aerodynamic testing.

Firstly, a 3D scanner was employed to capture the intricate details of the base model of the Wing Loong I UAV. This scanning process provided the foundational data required for constructing an accurate digital representation. Subsequently, the scanned data were meticulously processed using Geomagic Design X to create a precise 3D CAD model.

Once the initial CAD model was established, the geometry of the Wing Loong I aircraft was accurately constructed in SolidWorks. This step involved optimizing and simplifying the model geometry to enhance testing efficiency while maintaining the essential aerodynamic characteristics. The refined digital model was then 3D printed, producing a tangible test model made from PLA.

The 3D printed model underwent meticulous finishing processes to prepare it for rigorous testing protocols. This preparation ensured that the model was of high quality and suitable for experimental studies. Finally, the test model was subjected to wind tunnel testing to assess its aerodynamic performance.

By leveraging the validated and verified AeroMech tool, we are able to calculate the aerodynamic derivatives for the Wing Loong I UAV with confidence. The wind tunnel tests conducted on the 3D printed model serve to validate the predictions made by the AeroMech tool, providing valuable insights for further refinement and optimization of the UAV's design.

#### ***5.2.1.1 Creaform Handyscan 700 Portable Scanner***

To facilitate the creation of an accurate digital model of the Wing Loong I UAV, the Creaform Handyscan 700 Portable Scanner was employed. This advanced 3D scanner plays a

pivotal role in capturing the intricate geometries of the aircraft, which are essential for subsequent analysis and validation.

The Handyscan 700 provides comprehensive three-dimensional data, enabling detailed aerodynamic and structural assessments. This scanner's high resolution and accuracy are instrumental in generating precise digital models that serve as the foundation for both theoretical and practical research. The detailed information obtained supports thorough simulations and evaluations, which are critical for advancing our understanding of the aircraft's performance.

One of the key advantages of the Handyscan 700 is its portability, which allows for efficient in situ data capture without the need for extensive disassembly of the aircraft. This capability not only enhances the accuracy of the results but also streamlines the data collection process. The digital models produced form a robust basis for further computational analysis using the validated AeroMech tool and subsequent experimental validation through wind tunnel testing.

By integrating the high-resolution data from the Handyscan 700 with the computational capabilities of the AeroMech tool, we can accurately calculate the aerodynamic derivatives for the Wing Loong I UAV. This comprehensive approach ensures that our research is grounded in precise and reliable data, thereby advancing the field of aviation technology.

### ***5.2.2 Conversion of 3D Scan Data to CAD Models Using Geomagic Design X***

Geomagic Design X, a sophisticated reverse engineering software, plays a crucial role in converting 3D scan data into detailed CAD models. This software enables the creation of editable solid models, which are essential for iterative optimization and refinement. For the Wing Loong I UAV model, Geomagic Design X was employed to ensure precise geometry mapping and to correct any imperfections in the scanned data.

The process began by importing the 3D scan data captured by the Creaform Handyscan 700 into Geomagic Design X. The software facilitated the transformation of this raw scan data into a high-fidelity CAD model, preserving the intricate details of the aircraft's geometry. This step was critical for achieving the accuracy required for subsequent aerodynamic analysis.

Once the geometry mapping was completed and imperfections were corrected, the finalized model was exported as an STL file. This file format is widely used for 3D printing

and further CAD refinements. The STL file of the Wing Loong I model, as shown in Fig. 5.9, was then imported into SolidWorks for additional refinement and preparation for aerodynamic testing.

By integrating the high-resolution CAD model generated by Geomagic Design X with the validated AeroMech tool, we are able to accurately calculate the aerodynamic derivatives for the Wing Loong I UAV. This comprehensive approach ensures that the aerodynamic predictions are based on precise and reliable geometric data, thereby enhancing the overall accuracy of the research.

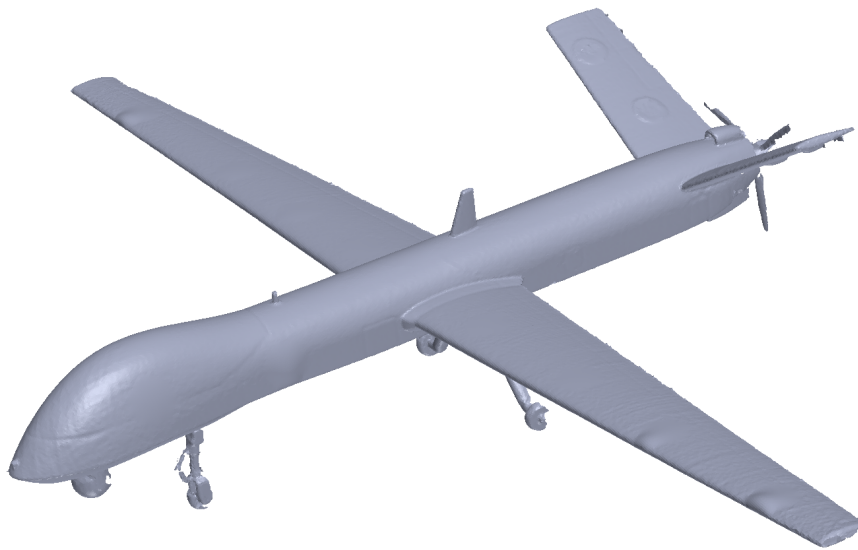


Fig. (5.9) WING LOONG 3D Scanning

### ***5.2.3 Refinement and Optimization of the Wing Loong I Model Using SolidWorks***

SolidWorks, a premier CAD software, is instrumental in the creation and refinement of spatial geometries through solid and surface modeling. This software supports the development of assemblies, simulations, animations, and 2D documentation, making it an essential tool for comprehensive design and analysis.

For the Wing Loong I UAV model, SolidWorks was utilized to refine the shape and dimensions derived from the initial base model. The process began by importing the STL file generated from Geomagic Design X into SolidWorks. This allowed for the precise manipulation of the model's geometry to ensure that it met the stringent requirements for aerodynamic testing.

Using SolidWorks, the structural components of the Wing Loong I model were optimized to maximize the efficiency of wind tunnel testing within the constraints of measurement capabilities. This optimization involved streamlining various elements of the model to enhance its aerodynamic performance while ensuring that the geometric integrity of the original design was maintained.

The refined CAD model, as illustrated in Fig. 5.10, was then prepared for 3D printing and subsequent wind tunnel testing. The comprehensive capabilities of SolidWorks facilitated a detailed and accurate representation of the Wing Loong I UAV, ensuring that the model was well-suited for both theoretical and practical evaluations.

By integrating the refined CAD model with the validated AeroMech tool, we can accurately calculate the aerodynamic derivatives for the Wing Loong I UAV. This approach not only confirms the predictions made by the AeroMech tool but also provides valuable insights for further refinement and optimization of the UAV's design.

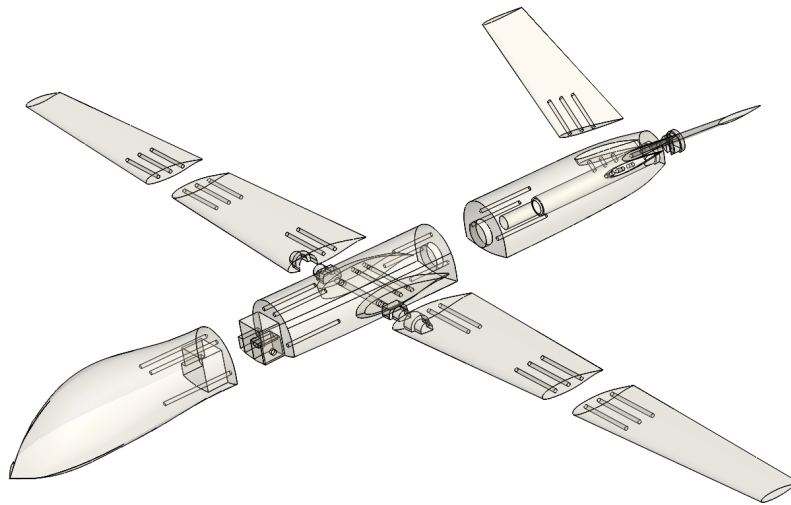


Fig. (5.10) WING LOONG CAD Part

#### ***5.2.4 3D Printing Methodology and Material Selection for Wing Loong I Model***

The 3D printing methodology employed in this study was carefully chosen to ensure the creation of accurate and high-quality models of the Wing Loong I UAV. The 3D printer used features a substantial working surface of  $200 \times 200 \times 300$  mm, which allows for the

concurrent printing of multiple components. The enclosed and heated printing chamber maintains a consistent temperature, thereby minimizing material shrinkage during cooling and ensuring the dimensional accuracy of the final object.

Polylactic Acid (PLA), a biodegradable thermoplastic derived from renewable resources, was selected as the primary material for printing. PLA is known for its translucency and shares similar properties with conventional thermoplastics, such as polystyrene. It does not require additional modifications for processing, making it an ideal choice for this application. Furthermore, PLA can exhibit characteristics of polypropylene and polyethylene when modified, adding to its versatility.

One of the notable properties of PLA is its ability to crystallize upon stretching, which allows for the adjustment of its impact strength by controlling the crystallization process through temperature management. This adaptability makes PLA suitable for various manufacturing applications, as it can be copolymerized and processed using standard equipment.

The use of PLA in the 3D printing process for the Wing Loong I model ensures that the material properties align with the requirements for aerodynamic testing. The ability to control and modify the material characteristics during the printing process allows for the production of robust and accurate models, which are essential for validating the aerodynamic derivatives calculated using the AeroMech tool.

### **5.3 Design and Manufacturing of the Test Rig**

The design and manufacturing of a specialized test rig are pivotal for the aerodynamic evaluation of the Wing Loong I UAV model within a wind tunnel. This rig has been meticulously engineered to facilitate both static and dynamic testing, thereby providing a comprehensive platform for aerodynamic analysis.

In static mode, as illustrated in Fig. 5.11, the rig employs a servo motor to precisely adjust the model's angle of attack. This capability is crucial for examining the aerodynamic forces and moments at various orientations. By enabling fine-tuned adjustments, the rig ensures that the model can be tested under a wide range of conditions, which is essential for a thorough aerodynamic evaluation.

For dynamic testing, as shown in Fig. 5.12, the rig utilizes a DC motor to generate



Fig. (5.11) Static Mode of Test Rig

pitching motions. This functionality is vital for simulating real-world flight dynamics and evaluating the stability and control characteristics of the model. The ability to replicate pitching movements allows for a more comprehensive investigation of the aircraft's aerodynamic performance.



Fig. (5.12) Dynamic Mode of Test Rig

The control of the test rig is achieved through a user-friendly interface operable via a tablet or smartphone connected through Bluetooth. The control unit comprises several key components, as depicted in Fig. 5.13, including an Arduino MEGA chip, a motor driver for the DC motor, and an encoder to measure motor revolutions. This sophisticated integration ensures precise and reliable control of the rig's movements, thereby enhancing the fidelity of the experimental data collected. By leveraging the validated AeroMech tool, we can accurately calculate the aerodynamic derivatives for the Wing Loong I UAV. The test rig, with its advanced capabilities, provides the necessary experimental platform to validate these

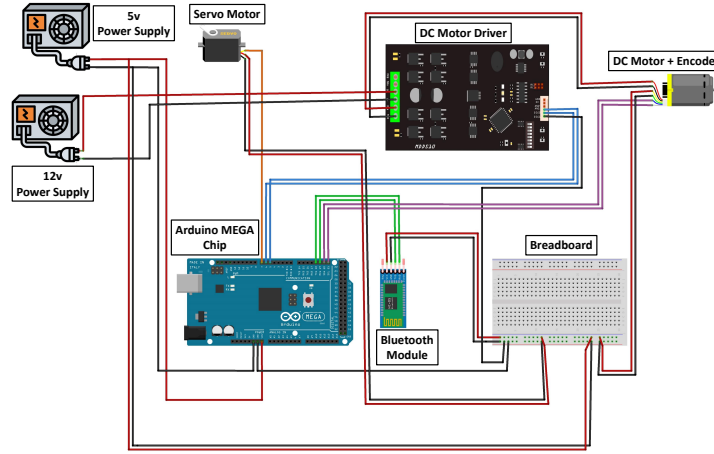


Fig. (5.13) The Control Unit Circuit

calculations, ensuring that the aerodynamic predictions are precise and reliable.

#### 5.4 Experimental Validation and Future Work

In the next phase of our research, we will conduct comprehensive wind tunnel testing of the Wing Loong I model using the custom-designed test rig. This experimental validation aims to confirm the results obtained from the Aeromech tool, as well as those from DATCOM and XFLR5 programs. By rigorously testing the model in both static and dynamic modes within the wind tunnel, we will be able to validate the aerodynamic derivatives and ensure the reliability and accuracy of our findings. This experimental effort will provide critical data to corroborate our computational analyses, thereby enhancing the robustness of our aerodynamic characterization of the Wing Loong I UAV.

## References

- [1] A. W. Babister, *Aircraft Dynamic Stability and Response: Pergamon International Library of Science, Technology, Engineering and Social Studies*. Elsevier, 2013.
- [2] T. Theodorsen, I. E. Garrick, and U. S. N. A. C. for Aeronautics, *General potential theory of arbitrary wing sections*. US Government Printing Office New York, 1933.
- [3] T. Theodorsen, “General theory of aerodynamic instability and the mechanism of flutter,” tech. rep., 1949.
- [4] B. Etkin and L. D. Reid, *Dynamics of flight: stability and control*. John Wiley & Sons, 1995.
- [5] J. E. Williams and S. R. Vukelich, “The usaf stability and control digital datcom. volume i. users manual,” tech. rep., MCDONNELL DOUGLAS ASTRONAUTICS CO ST LOUIS MO, 1979.
- [6] G. Mattsaits, “An update of the digital datcom computer code for estimating dynamic stability derivatives,” tech. rep., AEDC-TR-81-30, 1982.
- [7] W. Blake, “Prediction of fighter aircraft dynamic derivatives using digital datcom,” in *3rd Applied Aerodynamics Conference*, p. 4070, 1985.
- [8] H. Jaslow, “Aerodynamic relationships inherent in newtonian impact theory,” *AIAA Journal*, vol. 6, no. 4, pp. 608–612, 1968.
- [9] M. Tobak and W. R. Wehrend, “Stability derivatives of cones at supersonic speeds,” tech. rep., 1956.
- [10] L. E. Ericsson, “Unsteady aerodynamics of an ablating flared body of revolution including effect of entropy gradient,” *AIAA Journal*, vol. 6, no. 12, pp. 2395–2401, 1968.
- [11] L.-E. Ericsson, “Unsteady embedded newtonian flow(as basis for nose bluntness effect on aerodynamics of hypersonic slender bodies),” *Astronautica Acta*, vol. 18, pp. 309–330, 1973.

- [12] H. Ashley and G. Zartarian, "Piston theory-a new aerodynamic tool for the aeroelastician," *Journal of the Aeronautical Sciences*, vol. 23, no. 12, pp. 1109–1118, 1956.
- [13] J. Chen, "Pitching derivatives of wing in supersonic and hypersonic stream—method for local flow piston theory," *Acta Aerodyn Sin*, vol. 9, no. 4, pp. 469–476, 1991.
- [14] W.-W. Zhang, Z.-Y. Ye, C.-A. Zhang, and F. Liu, "Supersonic flutter analysis based on a local piston theory," *AIAA Journal*, vol. 47, no. 10, pp. 2321–2328, 2009.
- [15] C. Ye and M. Dongli, "An aircraft steady dynamic derivatives calculation method," in *2012 Proceedings of International Conference on Modelling, Identification and Control*, pp. 855–860, IEEE, 2012.
- [16] J. DeSpirito, S. I. Sifton, and P. Weinacht, "Navier-stokes predictions of dynamic stability derivatives: evaluation of steady-state methods," *Journal of Spacecraft and Rockets*, vol. 46, no. 6, pp. 1142–1154, 2009.
- [17] M. Park and L. Green, "Steady-state computation of constant rotational rate dynamic stability derivatives," in *18th applied aerodynamics conference*, p. 4321, 2000.
- [18] G. Guglieri and F. Quagliotti, "Dynamic stability derivatives evaluation in a low-speed wind tunnel," *Journal of aircraft*, vol. 30, no. 3, pp. 421–423, 1993.
- [19] E. Hanff and K. Orlik-Ruckemann, "Wind-tunnel measurement of dynamic cross-coupling derivatives," *Journal of Aircraft*, vol. 15, no. 1, pp. 40–46, 1978.
- [20] X. Liu, W. Liu, and Y. Zhao, "Navier–stokes predictions of dynamic stability derivatives for air-breathing hypersonic vehicle," *Acta Astronautica*, vol. 118, pp. 262–285, 2016.
- [21] W. H. Hui, "Stability of oscillating wedges and caret wings in hypersonic and supersonic flows," *AIAA Journal*, vol. 7, no. 8, pp. 1524–1530, 1969.
- [22] J. F. Le Roy and S. Morgand, "Saccon cfd static and dynamic derivatives using elsa," in *28th AIAA applied aerodynamics conference*, p. 4562, 2010.
- [23] J.-F. Le Roy, S. Morgand, and D. Farcy, "Static and dynamic derivatives on generic ucav without and with leading edge control," in *32nd AIAA applied aerodynamics conference*, p. 2391, 2014.

- [24] N. Alemdaroglu, I. Iyigun, M. Altun, H. Uysal, F. Quagliotti, and G. Guglieri, "Determination of dynamic stability derivatives using forced oscillation technique," in *40th AIAA Aerospace Sciences Meeting & Exhibit*, p. 528, 2002.
- [25] A. D. Ronch, D. Vallespin, M. Ghoreyshi, and K. Badcock, "Evaluation of dynamic derivatives using computational fluid dynamics," *AIAA journal*, vol. 50, no. 2, pp. 470–484, 2012.
- [26] F. G. Moore and R. C. Swanson Jr, "Dynamic derivatives for missile configurations to mach number three," *Journal of Spacecraft and Rockets*, vol. 15, no. 2, pp. 65–66, 1978.
- [27] J. Sahu, "Numerical computations of dynamic derivatives of a finned projectile using a time-accurate cfd method," in *AIAA Atmospheric Flight Mechanics Conference and Exhibit*, p. 6581, 2007.
- [28] V. Bhagwandin, "Numerical prediction of roll damping and magnus dynamic derivatives for finned projectiles at angle of attack," in *30th AIAA applied aerodynamics conference*, p. 2905, 2012.
- [29] E. Oktay and H. Akay, "Cfd predictions of dynamic derivatives for missiles," in *40th AIAA aerospace sciences meeting & exhibit*, p. 276, 2002.
- [30] B. Mialon, A. Khrabov, A. Da Ronch, L. Cavagna, M. Zhang, and S. Ricci, "Benchmarking the prediction of dynamic derivatives: Wind tunnel tests, validation, acceleration methods," in *AIAA atmospheric flight mechanics conference*, p. 8244, 2010.
- [31] B. Mialon, A. Khrabov, S. B. Khelil, A. Huebner, A. Da Ronch, K. Badcock, L. Cavagna, P. Eliasson, M. Zhang, S. Ricci, *et al.*, "Validation of numerical prediction of dynamic derivatives: The dlr-fl2 and the transcruiser test cases," *Progress in Aerospace Sciences*, vol. 47, no. 8, pp. 674–694, 2011.
- [32] M. Baigang, Z. Hao, and W. Ban, "Computational investigation of simulation on the dynamic derivatives of flight vehicle," in *29th Congress of the International Council of the Aeronautical Sciences*, pp. 1–7, ICAS St. Petersburg, Russia, 2014.
- [33] B. Mi, H. Zhan, and B. Chen, "Calculating dynamic derivatives of flight vehicle with new engineering strategies," *International Journal of Aeronautical and Space Sciences*, vol. 18, no. 2, pp. 175–185, 2017.

- [34] J. D. Bird, J. W. Cowan, and B. M. Jaquet, "Effect of fuselage and tail surfaces on low-speed yawing characteristics of a swept-wing model as determined in curved-flow test section of langley stability tunnel," tech. rep., 1948.
- [35] F. Lutze, "Experimental determination of pure rotary stability derivatives using curved and rolling flow wind tunnel," in *18th Aerospace Sciences Meeting*, p. 309, 1980.
- [36] T. Gainer, W. Henderson, and W. Phillips, "Rolling stability derivatives of a variable-sweep tactical fighter model at subsonic and transonic speeds," tech. rep., 1967.
- [37] K. Orlik-Ruckemann, "Review of techniques for determination of dynamic stability parameters in wind tunnels," *AGARD Lecture Series*, no. 114, 1981.
- [38] S. Avcı, "Static and forced oscillatory tests on a generetic combat aircraft model in ankara wind tunnel," Master's thesis, Middle East Technical University, 2000.
- [39] T. Şahin, "Modification of the oscillating test rig in ankara wind tunnel for roll oscillations and measurement of dynamic stability derivatives," Master's thesis, Middle East Technical University, 2001.
- [40] M. Tobak and L. B. Schiff, "Generalized formulation of nonlinear pitch-yaw-roll coupling: Part i-nonaxisymmetric bodies," *AIAA Journal*, vol. 13, no. 3, pp. 323–326, 1975.
- [41] J. R. Chambers, J. S. Bowman Jr, and G. N. Malcolm, "Stall/spin test techniques used by nasa," in *AGARD Flight Mechanics Panel Specialists' Meeting on Stall/Spin Problems of Military Aircraft, Brussels, Belgium*, 1975.
- [42] W. Bihrlé Jr, R. Hultberg, and W. Mulcay, "Rotary balance data for a typical single-engine low-wing general aviation design for an angle-of-attack range of 30 deg to 90 deg," tech. rep., 1978.
- [43] G. Malcolm and S. Davis, "New nasa-ames wind-tunnel techniques for studying airplane spin and two-dimensional unsteady aerodynamics," *AGARD Dyn. Stability Parameters*, 1978.
- [44] C. L. Denham and D. B. Owens, "Rotary balance wind tunnel testing for the faser flight research aircraft," in *AIAA Atmospheric Flight Mechanics Conference*, p. 3105, 2016.

- [45] B. Trieu, T. Tyler, B. Stewart, J. Chamock, D. Fisher, E. Heim, J. Brandon, and S. Grafton, "Development of a forced oscillation system for measuring dynamic derivatives of fluidic vehicles," in *38th Aerospace mechanisms symposium*, 2006.
- [46] M. Cook, "On the use of small scale aircraft models for dynamic wind tunnel investigation of stability and control," *Transactions of the Institute of Measurement and Control*, vol. 9, no. 4, pp. 190–197, 1987.
- [47] S. Carnduff, S. Erbsloeh, A. Cooke, and M. Cook, "Characterizing stability and control of subscale aircraft from wind-tunnel dynamic motion," *Journal of aircraft*, vol. 46, no. 1, pp. 137–147, 2009.
- [48] J. Pattinson, M. Lowenberg, and M. Goman, "A multi-degree-of-freedom rig for the wind tunnel determination of dynamic data," in *AIAA Atmospheric Flight Mechanics Conference*, p. 5727, 2009.
- [49] P. D. B. Navaratna, *Virtual Flight Testing in a Wind Tunnel Using a Manoeuvre Rig*. PhD thesis, University of Bristol, 2020.
- [50] J. Pattinson, *Development and evaluation of a wind tunnel manoeuvre rig*. PhD thesis, University of Bristol, 2010.
- [51] N. Peyada, A. Ghosh, and T. Go, "Mathematical modelling, simulation, and estimation of aircraft parameters using five degree-of-freedom dynamic test rig," *Proceedings of the Institution of Mechanical Engineers, Part G: Journal of Aerospace Engineering*, vol. 226, no. 1, pp. 55–63, 2012.
- [52] J. Pattinson, M. H. Lowenberg, and M. Goman, "Multi-degree-of-freedom wind-tunnel maneuver rig for dynamic simulation and aerodynamic model identification," *Journal of Aircraft*, vol. 50, no. 2, pp. 551–566, 2013.
- [53] S. A. Araujo-Estrada, Z. Gong, M. H. Lowenberg, S. Neild, and M. Goman, "Wind tunnel manoeuvre rig: a multi-dof test platform for model aircraft," in *54th AIAA Aerospace Sciences Meeting*, p. 2119, 2016.
- [54] J. Bratt, "Wind-tunnel techniques for the measurement of oscillatory derivatives," 1960.

- [55] S. Kim, P. Murphy, and V. Klein, "Evaluation and analysis of f-16xl wind tunnel data from dynamic tests," in *AIAA Atmospheric Flight Mechanics Conference and Exhibit*, p. 5396, 2003.
- [56] P. Murphy and V. Klein, "Validation of methodology for estimating aircraft unsteady aerodynamic parameters from dynamic wind tunnel tests," in *AIAA Atmospheric Flight Mechanics Conference and Exhibit*, p. 5397, 2003.
- [57] M. Lowenberg and H. Kyle, "Development of a pendulum support rig dynamic wind tunnel apparatus," in *AIAA atmospheric flight mechanics conference and exhibit*, p. 4879, 2002.
- [58] A. Gatto and M. Lowenberg, "Evaluation of a three degree of freedom test rig for stability derivative estimation," *Journal of Aircraft*, vol. 43, no. 6, pp. 1747–1761, 2006.
- [59] W. ŁUCJANEK and P. ADAMS, "Development of free-flight technique for nae helium hypersonic wind tunnel," *DME/NAE Quarterly Bulletin*, vol. 3, pp. 61–104, 1966.
- [60] M. E. Beyers, "Analysis of high-maneuvrability vehicles in free flight,," 1980.
- [61] M. Beyers, "Investigation of high manoeuvrability flight vehicle dynamics," in *ICAS Proceedings*, vol. 80, pp. 278–292, 1980.
- [62] B. Dayman Jr, "Free-flight testing in high-speed wind tunnels," tech. rep., 1966.
- [63] S. B. Grafton, J. R. Chambers, and P. L. Coe Jr, "Wind-tunnel free-flight investigation of a model of a spin-resistant fighter configuration," tech. rep., 1974.
- [64] C. Fremaux, D. Vairo, and R. Whipple, "Effect of geometry and mass distribution on tumbling characteristics of flying wings," *Journal of aircraft*, vol. 32, no. 2, pp. 404–410, 1995.
- [65] S. Daneshmand, R. Adelnia, and S. Aghanajafi, "Comparison between fdm model and steel model as wind tunnel testing models," in *Proceedings of the 6th WSEAS International Conference on Robotics, Control and Manufacturing Technology*, pp. 36–41, Citeseer, 2006.

- [66] E. Kroll and D. Artzi, “Enhancing aerospace engineering students’ learning with 3d printing wind-tunnel models,” *Rapid Prototyping Journal*, vol. 17, no. 5, pp. 393–402, 2011.
- [67] J. Anderson, *EBOOK: Fundamentals of Aerodynamics (SI units)*. McGraw hill, 2011.
- [68] A. Raza, S. Farhan, S. Nasir, and S. Salamat, “Applicability of 3d printed fighter aircraft model for subsonic wind tunnel,” in *2021 International Bhurban Conference on Applied Sciences and Technologies (IBCAST)*, pp. 730–735, IEEE, 2021.
- [69] M. Rahman, A. Miettinen, and T. Siikonen, “Modified simple formulation on a collocated grid with an assessment of the simplified quick scheme,” *Numerical Heat Transfer*, vol. 30, no. 3, pp. 291–314, 1996.
- [70] A. Rezgui, P. Cinnella, and A. Lerat, “Third-order accurate finite volume schemes for euler computations on curvilinear meshes,” *Computers & fluids*, vol. 30, no. 7-8, pp. 875–901, 2001.
- [71] Y.-C. Wang, T. Chen, and Y.-L. Yeh, “Advanced 3d printing technologies for the aircraft industry: a fuzzy systematic approach for assessing the critical factors,” *The International Journal of Advanced Manufacturing Technology*, vol. 105, pp. 4059–4069, 2019.
- [72] A. Ambrosi and M. Pumera, “3d-printing technologies for electrochemical applications,” *Chemical society reviews*, vol. 45, no. 10, pp. 2740–2755, 2016.
- [73] T. Sarkar, P. Sayer, and S. Fraser, “Flow simulation past axisymmetric bodies using four different turbulence models,” *Applied Mathematical Modelling*, vol. 21, no. 12, pp. 783–792, 1997.

# **Appendix A**

## **Proposed Model Equations**